Integration of Novel Quantum Emitters into On-Chip Photonic Devices

A thesis submitted in partial fulfilment of the requirements

for the degree of Doctor of Philosophy

University of Technology Sydney

Faculty of Science

School of Mathematical and Physical Sciences

by

Johannes E. FRÖCH

Supervisors

Prof. Milos TOTH

Prof. Igor AHARONOVICH

Dr. Sejeong KIM

June 2021

Certificate of Original Authorship

I, Johannes E. Fröch declare that this thesis, is submitted in fulfilment of the requirements for the award of Doctor of Philosophy, in the School of Mathematical and Physical Sciences at the University of Technology Sydney.

This thesis is wholly my own work unless otherwise referenced or acknowledged. In addition, I certify that all information sources and literature used are indicated in the thesis.

This document has not been submitted for qualifications at any other academic institution.

This research is supported by an Australian Government Research Training Program.

Signature:

Production Note:
Signature removed
prior to publication.

Date: 01/06/2021

Acknowledgements

I would not be here writing these lines of my thesis without the help and support of several people, whom I would like to say - ***thank you***.

First and foremost I would like to express my warmest gratitude to Professor Milos Toth. Thank him for accepting me to his group, and supporting my every step, even before my journey across to Australia started. More than once he was a steadfast support in science and personal matters. I would also like to give my profound appreciation to Professor Igor Aharonovich, who also has taught me a lot in scientific and personal matters, such as becoming a more efficient researcher. Then I would like to thank Sejeong Kim, who taught me so much on the matter of quantum and nanophotonics, which built the essential foundation for my PhD. To all three, I am grateful for stimulating my intellectual curiosity and for believing in my ideas. They have given me valuable support beyond their role as supervisor and by doing so they helped me more than I could ever repay them.

Next I would like to thank the many other academics of our group, Carlo Bradac, Alexander Solntsev, Mehran Kianinia, Toan Trong Tran, Zaiquan Xu, James Bishop, John Scott, Mika Westerhausen, and Helen Xu. All of them have helped me and taught me since I set my first foot in the lab and were always there for helpful discussions and to point out inconsistencies, which helped to improve my work. I am glad to have met such wonderful and open minded people and hope to stay connected to them in the future.

My appreciation also goes to all Technical Staff of the MAU, Katie McBean, Geoff McCredie, Herbert Yuan, Mark Berkahn, and Mark Lockrey. They all have been an invaluable support and without their know-how and maintenance of machines, I would not have made it past the introduction of this thesis. Therefore, I am deeply thankful to them.

Due to the extended network of my supervisors I had the pleasure to collaborate with some of the most brilliant minds in the field of quantum and nanophotonics. I am happy to have been working with Alan Bahm, Joe Christian, and Marcus Straw from FEI on several projects. Professor Weibo Gao from NTU, and his group members Disheng Chen and Mu Zhao. In the same way I would like to thank Professor Paul Barclay from Calgary and his group, especially Prasoon Kumar Shandilya, Matthew Mitchell, and David Lake. Also I would like to

acknowledge the support from Julie M. Cairney and Vijay Bhatia from the University of Sydney.

I certainly would have missed out on a lot of fun without my fellow MAUans and PhD colleagues. Here I would like to thank all of them, Noah Mendelson, Ngoc My Hanh Duong, Minh Nguyen, Chi Li, Blake Regan, Daniel Totonjian, Milad Nonahal, Angus Gale, Mikhail Borisov, Thinh Tran, Yongliang Chen, Aleksandra Trycz, Connor Stewart, Simon White and of course all the lab spiders, which were always a highlight and good reminder that our lab is located in Australia.

Here, I would like to thank the people who have been by my side for the longest –my family. Thanks to my parents Luise and Wolfgang and my siblings, Christopher, and Lisa, as well as Anna and Manuel and their children Raphael and Theresia. Thanks to all of them for

And finally, most of all, I would like to thank my partner for putting up with me and giving me the endless support that helped me overcome my downs and who made my ups during my PhD journey even better.

List of Publications

Refereed journal publications

1) Kim, Sejeong*, **Johannes E. Fröch***, Joe Christian, Marcus Straw, James Bishop, Daniel Totonjian, Kenji Watanabe, Takashi Taniguchi, Milos Toth, and Igor Aharonovich. "Photonic crystal cavities from hexagonal boron nitride." *Nature communications* 9, no. 1 (2018): 1-8.[1]

2) Shandilya, Prasoon K.*, **Johannes E. Fröch***, Matthew Mitchell, David P. Lake, Sejeong Kim, Milos Toth, Bishnupada Behera, Chris Healey, Igor Aharonovich, and Paul E. Barclay. "Hexagonal boron nitride cavity optomechanics." *Nano letters* 19, no. 2 (2019): 1343-1350.[2]

3) **Fröch, Johannes E.***, Yongsop Hwang*, Sejeong Kim, Igor Aharonovich, and Milos Toth. "Photonic nanostructures from hexagonal boron nitride." *Advanced Optical Materials* 7, no. 4 (2019): 1801344.[3]

4) **Fröch, Johannes E.**, Sejeong Kim, Connor Stewart, Xiaoxue Xu, Ziqing Du, Mark Lockrey, Milos Toth, and Igor Aharonovich. "Photonic nanobeam cavities with nanopockets for efficient integration of fluorescent nanoparticles." *Nano Letters* 20, no. 4 (2020): 2784-2790.[4]

5) **Fröch, Johannes E.**, Sejeong Kim, Noah Mendelson, Mehran Kianinia, Milos Toth, and Igor Aharonovich. "Coupling Hexagonal Boron Nitride Quantum Emitters to Photonic Crystal Cavities." *ACS nano* (2020).[5]

6) **Fröch, Johannes E.**, Alan Bahm, Mehran Kianinia, Zhao Mu, Vijay Bhatia, Sejeong Kim, Julie M. Cairney, Weibo Gao, Carlo Bradac, Igor Aharonovich, and Milos Toth. "Versatile Direct-Writing of Dopants in a Solid State Host through Recoil Implantation." *Nature communications in press* (2020).[6]

7) Bishop, James, Marco Fronzi, Christopher Elbadawi, Vikram Nikam, Joshua Pritchard, **Johannes E. Fröch**, Ngoc My Hanh Duong et al. "Deterministic nanopatterning of diamond using electron beams." *ACS nano* 12, no. 3 (2018): 2873-2882 [7]

8) Elbadawi, Christopher, **Johannes E. Fröch**, Igor Aharonovich, Milos Toth, and Charlene J. Lobo. "One-Step Nanoscale Patterning of Silver Nanowire–Nitride Heterostructures Using

Substrate-Assisted Chemical Etching." *The Journal of Physical Chemistry C* 123, no. 1 (2018): 945-949.[8]

9) Chen, Disheng, Zhao Mu, Yu Zhou, **Johannes E. Fröch**, Abdullah Rasmit, Carole Diederichs, Nikolay Zheludev, Igor Aharonovich, and Weibo Gao. "Optical gating of resonance fluorescence from a single germanium vacancy color center in diamond." *Physical review letters* 123, no. 3 (2019): 033602.[9]

10) Kim, Sejeong, **Johannes E. Fröch**, Augustine Gardner, Chi Li, Igor Aharonovich, and Alexander S. Solntsev. "Second-harmonic generation in multilayer hexagonal boron nitride flakes." *Optics letters* 44, no. 23 (2019): 5792-5795.[10]

11) Regan, Blake, Alireza Aghajamali, **Johannes E. Fröch**, Toan Trong Tran, John Scott, James Bishop, Irene Suarez-Martinez et al. "Plastic Deformation of Single-Crystal Diamond Nanopillars." *Advanced Materials* 32, no. 9 (2020): 1906458.[11]

12) Bernhardt, Nils, Kirill Koshelev, Simon JU White, Kelvin Wong Choon Meng, **Johannes E. Fröch**, Sejeong Kim, Toan Trong Tran, Duk-Yong Choi, Yuri Kivshar, and Alexander S. Solntsev. "Quasi-BIC Resonant Enhancement of Second-Harmonic Generation in WS2 Monolayers." *Nano Letters* 20, no. 7 (2020): 5309-5314.[12]

13) Kianinia, Mehran, Simon White, **Johannes E. Fröch**, Carlo Bradac, and Igor Aharonovich. "Generation of spin defects in hexagonal boron nitride." *ACS Photonics* 7, no. 8 (2020): 2147-2152.[13]

14) Mu, Zhao, Soroush Abbasi Zargaleh, Hans Jürgen von Bardeleben, **Johannes E. Fröch**, Milad Nonahal, Hongbing Cai, Xinge Yang et al. "Coherent manipulation with resonant excitation and single emitter creation of nitrogen vacancy centers in 4H silicon carbide." *Nano Letters* 20, no. 8 (2020): 6142-6147.[14]

15) Mu, Zhao, Yu Zhou, Disheng Chen, **Johannes E. Fröch**, Jianqun Yang, Xingji Li, Igor Aharonovich, and Wei-Bo Gao. "Observation of Binary Spectral Jumps in Color Centers in Diamond." *Advanced Optical Materials* (2020): 2000495.[15]

16) Rohdenburg, Markus, **Johannes E. Fröch**, Petra Martinović, Charlene J. Lobo, and Petra Swiderek. "Combined Ammonia and Electron Processing of a Carbon-Rich Ruthenium Nanomaterial Fabricated by Electron-Induced Deposition." *Micromachines* 11, no. 8 (2020): 769.[16]

Oral conference presentations

1) **Fröch, Johannes E.** et al. “Photonic Crystal Cavities in hexagonal Boron Nitride by EBIE”, 7th Workshop on Focused Electron Beam-Induced Processing, Modena, 2018

2) **Fröch, Johannes E.** et al. “Fabrication and Tuning of Photonic Crystal Cavities in hexagonal Boron Nitride by Electron Beam Induced Etching”, 19th International Microscopy Congress, Sydney, 2018

3) **Fröch, Johannes E.** et al. “Fabrication of Photonic and Optomechanics Devices in hBN by Electron Beam Induced Etching”, DPG Fruehjahrstagung, Regensburg, 2019

4) **Fröch, Johannes E.** et al. “Photonic nanobeam cavities with nano-pockets for efficient integration of fluorescent nanoparticles”, SPIE Optics + Photonics, virtual conference, 2020

Contents

Certificate of Original Authorship i
Acknowledgements ii
List of Publications iv
Abbreviations xxi
Abstract xxiii
Chapter 1 Introduction 1
Chapter 2 Background 4
2.1 Single Photon Emitters 4
2.1.1 Diamond 11
2.1.2 Hexagonal Boron Nitride 14
2.2 Photonic Crystal Cavities 17
2.3 Device Integration 22
Chapter 3 Experimental Methods 25
3.1 Nanofabrication 25
3.2 Confocal Microscopy 26
Chapter 4 Photonic Crystal Cavities from Hexagonal Boron Nitride 28
4.1 Introduction 28
4.2 Methods 29
4.2.1 Preparation of suspended hBN 29
4.2.2 Electron Beam Induced Etching 30
4.2.3 Focused Ion Beam Milling 30
4.2.4 Finite Difference Time Domain Simulations 30
4.3 Results 32
4.3.1 Fabrication of hBN Photonic Crystals 32
4.3.2 1D Photonic Crystal Nanobeam Cavity 35

4.3.1 Tunable photonic cavity....40
4.3.2 Creation of quantum emitters....42
4.4 Conclusion....45
Chapter 5 Photonic Nanostructures from Hexagonal Boron Nitride....46
5.1 Introduction....46
5.2 Fabrication Scheme....47
5.3 Fabrication of Prototype Structures....50
5.4 Fabrication Artefacts....52
5.5 Device Functionality....55
5.6 Conclusion....55
Chapter 6 Coupling Hexagonal Boron Nitride Emitters to Photonic Crystal Cavities....57
6.1 Introduction....57
6.2 Methods....58
6.2.1 Device Fabrication....58
6.2.2 Simulations....59
6.3 Results and Discussion....60
6.3.1 Hybrid Integration....60
6.3.2 Device Characterisation....62
6.3.3 Observation of Integrated Single Photon Emitter....64
6.3.4 Observation of Spectral Shifts and Momentary Coupling....66
6.4 Conclusion....68
Chapter 7 Nanobeam Cavities with Pockets for Efficient Integration of Nanoparticles....69
7.1 Introduction....69
7.2 Methods....70
7.2.1 Device Fabrication....70
7.2.2 CL Characterisation....70
7.3 Results and Discussion....71

7.3.1 The Pocket Cavity Concept 71
7.3.2 Fabrication 73
7.3.3 Device Characterisation 74
7.3.4 Coupled Cavity Particle System 76
7.4 Conclusion 80
Chapter 8 Versatile Direct-Writing of Dopants in a Solid State Host 82
8.1 Introduction 82
8.2 Methods 84
8.2.1 Sample Preparation 84
8.2.2 FIB Irradiation 84
8.2.3 Post Irradiation Treatment 84
8.2.4 PL Measurements 85
8.2.5 Electron Beam Induced Etching (EBIE) 86
8.2.6 AFM Measurements 86
8.3 Results 86
8.3.1 Concept 86
8.3.2 Fluence and Spatial Control 88
8.3.3 Emitter Activation 95
8.3.4 Further Characterisation 97
8.3.5 Ion Beam Profile 100
8.3.6 Spatial and Depth Profile 102
8.3.7 Implantation into other Systems and Restrictive Geometries 106
8.4 Conclusion 108
Chapter 9 Conclusion and Outlook 109
9.1 Summary 109
9.2 Future Work 110
Bibliography 113

List of Figures

Figure 2.1 Toy model of a single photon emitter. (a) A naive picture of a single photon emitter, shown as a 2 level system, with a delta like spectrum shown in (b). (c) A refined system considering atomic orbitals and intermediate transitions. (d) The emission can be polarised, and may be decreased due to non radiative decay channels. (e) The system closest to reality, assuming an emitter in a solid state crystal with pecuilar shaped ground and excited state orbitals. The system may have spin multiplicity and different charge states. (f) A spectrum of such a system may thus have different main transitions, due to different charge states. Accompanying to the zero phonon line (ZPL) is the phonon side band (PSB).

Figure 2.2. Identifying a single photon emitter. a) Schematic of a Hanbury-Brown and Twiss setup. b) The ideal autocorrelation curve collected from the background free emission of a single photon emitter.

Figure 2.3 Single Photon Emitter in the solid state. (a)Semiconductor Quantum Dots are localised 0D systems with a confined bandgap, causing the exciton to act as an SPE. (b) Defects and ions in 3D crystal can act as single photon emitter, such as diamond, SiC, or YAG. (c) Defects and bound exciton like single emitter in low dimensional materials, such as in carbon nanotubes, hBN, or strained WSe_2. Reproduced from (a) - [17,18], (b) - [19], (c) - [13,20,21]

Figure 2.4 The NV centre in Diamond. (a) The crystallographic structure of the NV centre. (b) The associated level structure of the NV centre. (c)The PL spectrum of the NV centre at room temperature and cryogenic temperature. Reproduced from [22]

Figure 2.5 The group IV colour centres in diamond. (a) The archetypical defect configuration of the group IV split vacancies. M indicates one of the atoms, Si, Ge, Sn, Pb, V indicates a vacancy. (b) Spectra of the PbV, GeV, SnV, and SiV. (c)The related level structure of the group-IV defects. Reproduced from [23]

Figure 2.6 Single Photon emitter in hBN. (a) The atomic structure of hBN with Nitrogen and Boron indicated as blue and pastel spheres, respectively. (b) The spectra of the initially identified SPEs in multi- and monolayer hBN, red and blue, respectively. (c) The g^2 measurement of the related emitters, shown in (b). (d) Emission of an hBN single emitter in the UV, identified by TEM cathodoluminescence. (e) SPEs in the visible range. (f) A hBN SPE in

the NIR regime. (g) Multimodal distribution of the ZPL in the visible range. (h) Creation of Emitter through annealing or electron beam irradiation. (i) Site specific creation of emitter through strain engineering. Reproduced from (a-c) - [24], (d) - [25], (e),(h) - [26], (f) - [27], (g) - [28], (i) - [29]

Figure 2.7 The VB- emitter in hBN. (a) Creation of the defect through ion beam irradiation. (b) A hBN flake after irradiation, with an inset showing a PL map, with the irradiated regions appearing bright. (c) The spectrum of the VB- defect. (d) PL contrast of the emission in ODMR. Reproduced from [13]

Figure 2.8 Other colour centers in hBN. (a) CVD grown hBN predominantly exhibit a ZPL with emission around 585 nm. (b) Emission of hBN colour centre in MOVPE growth with different doping flow of a carbon precursor (TEB). Reproduced from [30,31]

Figure 2.9 The band diagram of Photonic crystals. (a) Dispersion relation of a 3D photonic crystal, with a full band gap for a structure as shown in the bottom left inset. Symmetry points of the crystal are defined in the bottom right inset. (b) Dispersion relation of a 2D photonic crystal, as shown in the inset top left, with symmetry points defined by the top right inset. Solutions for the wave equation that are not confined in the slab, which lie inside the light cone, are not depicted. Reproduced from [32,33]

Figure 2.10. Example of a Photonic Crystal Cavity. (a) A PCC is achieved by introducing a defect into a photonic crystal. In this case by increasing (blue) or decreasing (red) a hole at the centre. Grey circles represent air holes in a dielectric slab. (b) In the corresponding band diagram defect states emerge, known as acceptor or donor states, corresponding to an increase or decrease in the centre hole size, respectively. (c) Representative field distributions for the corresponding mode associated with the defect. Reproduced from (b) - [33], (c) - [34]

Figure 2.11 Methods for site specific emitter creation based on ion implantation. (a) Implantation of Nitrogen into diamond through apertures, as defined by a mask by Electron Beam Lithography. A map of the implanted sites shows the capability of the technique. (b) Implantation of Nitrogen into diamond through a pierced AFM tip. (c) Direct and mask free ion implantation of rare earth ions by a specialised Focused Ion Beam Setup, utilising a Paul trap as the ion source. (d) Ion implantation of Si into diamond from a Liquid Metal Ion Source FIB system. Reproduced from (a) - [35], (b) - [36], (c) - [37], (d) - [38]

Figure 3.1. The main confocal laser microscope setup used for most optical characterisation during this thesis

Figure 4.1. 3D FDTD modelling for 1D photonic crystal cavity. (a), Schematic showing 1D ladder-like photonic crystal cavity. (b), Photonic mirror region has lattice constant of 'a', while photonic well region has modulated lattice constant as plotted in the graph. (c), Spectrum showing the S0, F0, F1, and F2 modes. (d), Q-factor with respect to thickness of nanobeam. (e), Q-factor with respect to nanobeam width (w).

Figure 4.2. Free-standing hexagonal boron nitride 2D photonic crystal cavities. (a) Optical microscope image of exfoliated hBN crystals on a silicon substrate. The scale bar corresponds to 50 µm. (b) Schematic of a free-standing hBN cavity on a trenched silicon substrate. (c) SEM image of the hBN showing the layered structure. The scale bar corresponds to 500 nm. (d) False Color SEM image (45°) of a free-standing hBN photonic crystal cavity fabricated using a combination of RIE and EBIE. The scale bar corresponds to 2 µm. (e) Top view of a 2D photonic crystal cavity. The scale bar corresponds to 2 µm. (f) Photoluminescence spectra with a laser exciting the cavity mode (red) compared with an off-cavity excitation (grey). The inset depicts the electric field intensity profile of the fundamental mode for the cavity calculated using 3D FDTD

Figure 4.3. Optical analysis of one dimensional (1D) hBN photonic crystal cavities. ***a*** *SEM image of a 1D ladder PCC with 25 rectangular air holes. The scale bar is 1 µm.* ***b*** *magnified view showing the geometrical parameters; width (w), lattice constant (a), air hole width (h_x) and air hole height (h_y). The cavity was fabricated using a combination of RIE and EBIE. The scale bar corresponds to 200 nm.* ***c*** *Photoluminescence spectra of different 1D ladder PCCs in the same hBN crystal with varying lattice constants of 220 nm (black), 250 nm (red), and 280 nm (blue), respectively. F0, F1, and F2 mark the position of the zeroth, first, and second order mode from the first dielectric band. S0 marks the position of the zeroth order from the second dielectric band mode.* ***d*** *3D FDTD simulation result showing field profiles of the measured optical modes.* ***e*** *Experimentally obtained Q-factors of various 1D PCCs fabricated from hBN.* ***f*** *PL spectrum of a 1D cavity fabricated by focused ion beam milling, showing a high Q (~ 2100) mode in the visible spectral range. The inset is an SEM image of the cavity and the scale bar corresponds to 1 µm*

Figure 4.4 Sidewall slopes. (a), Top-view SEM image after RIE. (b), Tilted (45°) view after RIE. (c), Tilted view (52°) of a cross section after FIB etching. (d), Tilted view (60°) of a cross section after EBIE. Scale bars in all images correspond to 200 nm.

Figure 4.5. Comparison of Raman spectra of pristine hBN (black) with (a), RIE/ EBIE-processed area (blue) and (b), FIB-processed area (orange).

Figure 4.6. Tuning of a 1D nanobeam cavity using direct-write, maskless EBIE. (a) Schematic of the etch process in which a focused electron beam (blue) is scanned along the outer sidewalls of the nanobeam cavity to induce the etch reaction in the presence of water molecules. (b) Photoluminescence (PL) spectra of a 1D photonic cavity before tuning (black), and after the first (red) and second (blue) tuning steps were performed by EBIE. (c) Q-factor of the F0 (circles) and F1 (triangles) modes measured immediately after fabrication (black), and after the first (red), and second (blue) tuning steps

Figure 4.7. Generation of single photon emitters within the hBN cavities. (a) Optical microscope image of the analysed area comparing an unprocessed site (left), with a processed site (right) that contains several 1D nanobeam cavities. The scale bar corresponds to 1 μm. (b) corresponding Photoluminescence map of this region. Positions of quantum emitters are indicated by yellow circles (c) PL spectra from two regions of the same cavity showing an optical mode only (blue) and the combination of an optical mode and an emitter (red). (d) Measured $g^2(\tau)$ curve obtained from this emitter

Figure 5.1. Fabrication of photonic structures from hBN. a) Mechanical exfoliation of a hBN flake from sticky tape onto a prepatterned substrate. b) An as-exfoliated hBN flake after a cleaning process. c) Optical image showing such a flake before further fabrication steps. d) Deposition of a tungsten layer and spin coating of a PMMA layer, which serve as masks in the EBIE and RIE steps, respectively. e) EBL followed by SF_6 RIE. f) Optical image of the hBN flake containing 1D photonic crystals after RIE and PMMA removal, showing that patterns are transferred into tungsten and hBN. g) Masked EBIE used to complete the hBN etch. h) Final hBN photonic structures after tungsten removal. i) Optical microscope image of the hBN flake obtained after all processing steps. Scale bars in optical images correspond to 10 μm.

Figure 5.2. Primary Electron penetration depth in a Tungsten Film (15 nm) on hBN (Substrate). (a) Interaction volume of PEs. (b) PE hits vs. depth.

Figure 5.3. Various photonic structures fabricated from hBN. a) Top view of a photonic crystal cavity with air hole sizes of 100 nm × 450 nm over a length of 10 μm. The scale bar corresponds to 500 nm. b) Tilted and c) top view images of free-standing 1D photonic crystal cavity arrays. Scale bars correspond to 2 and 4 μm, respectively. d) A set of hBN microrings with various

sizes and e) a magnified view of the highlighted area. Scale bars correspond to 10 and 1 μm, respectively. f) A circular grating structure in a tilted view, the scale bar corresponds to 2 μm. g) A waveguide with two grating couplers and h) its magnified image. Scale bars correspond to 5 and 1 μm, respectively. Structures in (d)–(h) are on a SiO_2 substrate.

Figure 5.4. Fabrication artefacts of hBN. a) Photonic crystal cavities imaged after RIE, showing small spots from micromasking. Some spots are highlighted with red circles. b) The same spots persist after EBIE, and give rise to the formation of grass in nominally unmasked regions of hBN, seen clearly in the tilted view in c). Scale bars correspond to 500 nm in (a) and (b), and 250 nm in (c), respectively. Two images of the same nanobeam obtained after subsequent EBIE steps, d) and e), show that some areas of unmasked hBN are not etched, producing features that agglomerate and wrap around the cavities. Scale bars correspond to 500 nm. An overetched structure shown in f) top and g) tilted views, in which hBN residuals are not removed even after prolonged EBIE. The integrity of the photonic crystal cavity is compromised by agglomeration of residuals. Scale bars correspond to 500 nm. A comparison of the side view after RIE only h) and after the subsequent EBIE processing step i). Scale bars correspond to 500 nm. j) and k) are enlarged views of the outlined sections in (g) and (h). Scale bars correspond to 250 nm.

Figure 5.5. Quality factors of the fabricated hBN devices. a) A 1D photonic crystal cavity (PCC) with a resonant mode at ≈701 nm. The left inset shows the measured device, with a scale bar of 1 μm. The right inset shows the cavity Q of ≈1500, as determined from a Lorentzian fit at the resonant wavelength. b) WGMs of a hBN microring. The left inset shows the measured device. The scale bars correspond to 1 μm. The right inset shows the Q of the microring resonator was determined to be 500 by a Lorentzian fit of a resonance at 644 nm.

Figure 6.1. Integration of CVD-grown hBN with 1D photonic crystal cavities. (a) Schematic of the fabrication steps: (I) CVD growth of hBN on copper. (II) Precheck of the hBN film on copper using a confocal microscope setup. (III) Transfer the hBN from copper to a 180 nm thick Si_3N_4 substrate. (IV) Spin coating of the EBL resist (CSAR 62). (V) EBL patterning of the cavity structures. (VI) RIE and undercutting to create free-standing hBN/Si_3N_4 devices. (b) Optical microscope image with the final sample. hBN-covered area (white-dashed guideline) is directly visible due to optical contrast. (c) SEM image showing the final free-standing, hybrid photonic cavity arrays.

Figure 6.2. Comparison of hBN films annealed and not annealed after transfer. (a) and (b) show the same position of a sample with a hBN film transferred and annealed, before and after all processing steps, respectively. (c) and (d) show the same position of a sample with a hBN film transferred and not annealed, before and after all processing step.

Figure 6.3. Photonic cavity design and properties. (a) Magnified view of a fabricated 1D nanobeam photonic crystal cavity with circular holes. Toward the middle of the cavity, the hole periodicity and diameter are linearly tapered. (b) Top view FDTD simulation of the hBN layer showing the main resonance at 590 nm in the centre of the device with a theoretical Q-factor of 1.6×10^4 and a mode volume of $1.5\ (n/\lambda)^3$. (c) Side view showing the distribution of the mode and the overlap with the top hBN layer, for which the field overlap is approximately 40% for a 5 nm thick hBN film. (d) Optical image of an area of fabricated devices at the boundary of a transferred hBN film. A direct comparison of the device functionality was taken from cavities fabricated under the same conditions without hBN and cavities with hBN on top showing representative resonances at a target wavelength spanning from 580 to 605 nm shown to their right, respectively. (e) Comparison of the Q-factor from the cavities in the shown area reveals on average values of 2730 ± 430 and 2700 ± 530 for cavities without (crosses) and with (circles) hBN, respectively.

Figure 6.4. Coupled hBN–Si_3N_4 system. Cavity 1 (a) shows partial coupling, while Cavity 2 (b) shows a high degree of coupling. (I) PL maps show the emitter positions within the respective cavities, being at or close to the centre of the device. (II) Spectra from the respective white-marked spots show the emissions of quantum emitters at 588 and 593 nm for Cavity 1 and Cavity 2, respectively. For Cavity 1, a distinctive resonance mode can be seen at 595 nm, while for Cavity 2 the ZPL cannot be clearly distinguished from a cavity mode. Insets show the cavity resonance determined from a measurement with a higher resolution grating. (III) Correlation measurements with $g^2(0)$ values of 0.3 and 0.1, demonstrating the single photon nature of the emitters. (IV) The ZPL from the coupled system was, in each case, fitted with a sum of Lorentzians (purple) to estimate the respective contributions from the emitter (red and yellow) and cavity (blue).

Figure 6.5. Dynamic enhancement of a quantum emitter which spectrally diffused to a cavity mode. (a) PL spectra, which are normalized to the maximum intensity of the cavity mode, measured with spectrally jumping emitter. As found, the emitter was partially overlapping with a cavity mode at 593 nm. A 1st spectral shift caused the ZPL to be coupled with the cavity mode. After a second shift, the

ZPL was again detuned by 5 nm from the resonance. Then we observed bleaching of the quantum emitter. (b) The same PL spectra without normalization showing PL enhancement of the emitter. (c) Lorentzian fits of spectra in (a). The ZPL (red and yellow) and the cavity mode (blue) were used to estimate the relative contributions, shown in the same order as in (a).

Figure 7.1. One-dimensional fishbone photonic cavity design. (a) 3D schematic of the proposed fishbone photonic crystal cavity (PCC) design with a nanopocket placed in the middle of the cavity to host a fluorescent nanoparticle. The unit cell of the fishbone photonic crystal outlined by white dashed lines with periodicity a, backbone width b, bar length l_b, bar width w_b, and thickness t. (b) Refractive index modulation induced by altering regions of high (H) and low (L) refractive index either via air holes or by placing nanobars periodically on a backbone. FDTD simulation results showing the electric field intensity of the cavity (c) with a nanopocket and (d) without a nanopocket with (I) top-view, (II) cross-sectional view, and (III) magnified view at the nanoparticle cross-section.

Figure 7.2. Fabrication of pocket cavities. (a) Schematic outline of the cavity fabrication scheme: (I) resist application on a SiN/Si substrate, (II) patterning of the cavity outline and the nanopocket in the centre by EBL, (III) RIE placement in a nanoparticle solution, and (IV) final undercut of the cavity structure. (b) Set of PCCs after fabrication showing no nanoparticle contamination on the top of the cavity. Magnified SEM images showing cavities (c) without a nanoparticle and (d) with a nanoparticle in the nanopocket, respectively. (e) Cross-section of a pocket cavity showing halfway through the etched area of the nanopocket due to the RIE lag effect.

Figure 7.3. Spatial and spectral characterization of pocket cavities. (a) SEM image of the cavity investigated for the CL measurement. (b) Spectral response in CL of the structure averaged over the entire mapped area (red) and over the cavity centre (blue), showing a resonant mode at 595 nm. (c) 2D intensity map showing the spatial distribution of the optical mode at the cavity centre. (d) Representative PL spectra showing cavity modes from PCCs with and without a nanopocket. (e) Q-factors of all investigated PCCs in the range 600–680 nm, determined from PL spectra (grating: 1200 lines/mm).

Figure 7.4. Spectral properties of the utilised UCNP. (a) Emission Spectrum under 980 nm excitation with notable emission bands at 520 nm, 540 nm, and 660 nm. (b) Level diagram for the upconversion excitation process of the Er^{3+}.

Figure 7.5. Fluorescent nanoparticles coupled to a pocket cavity. SEM images of UCNPs (black spots) on top of a cavity with particles placed (a) aside the pocket and (b) in the pocket, indicated by the yellow arrow. The red outline represents the approximate size and position of the pumping spot to identify particles that contribute primarily to the PL signal. (c, d) Spectra recorded from the respective cavities with a 980 nm cw excitation laser. (c) For the cavity with particles aside the pocket, we observe a 3.5-fold PL enhancement at the resonance (668 nm) with a Q-factor of 1500 (inset). (d) For the cavity with a particle in the pocket, we observe a 20-fold PL enhancement at the resonance (668 nm) with cavity Q-factor of 1200 (inset). Lifetime measurements for cavities, without and with a particle in the pocket, are shown in parts e and f, respectively. In both cases, a representative lifetime measurement of the UCNP is shown in blue, with a single exponential fit yielding a lifetime of 350 μs. Measurements on cavities are shown in red, with a double exponential fit. For the cavity with particles outside the pocket, a lifetime of 200 μs was obtained. For the cavity with a particle in the pocket, a lifetime of 140 μs was obtained.

Figure 8.1. Creation of colour centres in a diamond target by recoil-implantation. (a) Schematic illustration of the process inside a standard electron-ion dual beam microscope. The inset shows an atomic picture of the process: momentum is transferred from inert primary ions to the atoms of a thin film comprised of the dopants, resulting in implantation of the latter into the underlying target. (b) Photoluminescence map of a pattern fabricated in a single region of diamond using four dopant species that were implanted by momentum transfer from an electrostatically scanned Xe^+ beam. The emblem is patterned in Pb, and the letters U, T, and S in Sn, Ge, and Si, respectively. The scale Bar corresponds to 5 μm. (c) Photoluminescence spectra recorded from the implants in (b), showing characteristic emissions from defect complexes that contain the Pb (green), Ge (orange), Sn (red), and Si (maroon) dopants.

Figure 8.2. Spot arrays of dopants implanted into diamond as a function of Xe^+ fluence. (a) Photoluminescence map of a representative array, here shown for Si dopants. The framed area shows the lowest fluence of Xe^+ that yielded an unambiguous observable array in this case. The number above each array specifies the Xe^+ fluence in units of cm^{-2}. (b) Photoluminescence spectra of emitters from the lowest observable fluence of SiV (maroon), GeV (orange), SnV (red) and PbV-related emissions (green). An additional peak at 630 nm corresponds to the Raman signal of the utilised immersion oil. Insets show second order correlation measurements (background corrected), illustrating the quantum nature of the colour centres.

(c) Histograms showing variability in ZPL wavelength in spot arrays of the colour centre ensembles.
Figure 8.3. Lifetime measurements of implanted regions for SiV (a), GeV (b), SnV (c), and PbV (d) with the respective lifetimes determined from a single exponential fit, given in the top right corner.

Figure 8.4. Characterisation at 4 K. PL (a) and PLE (b) spectra for spot implanted sites of SiV, (c) and (d) for GeV, (e) and (f) for PbV, respectively.

Figure 8.5. Averaged spectra over different dosages, normalised to the maximum of the highest fluence for Si (a), Ge (b), Sn (c), and Pb (d). The black lines correspond to the spectral average for the lowest observed fluence of the spot implantation series. The second lowest line (one shade brighter) corresponds to the next spot series and so forth.

Figure 8.6. Determination of the creation yield for different colour centres versus Xe^+ fluence. a) The average pixel intensity was extracted from PL maps. Error bars indicate standard deviation of the average. b) Colour centres created per primary Xe ion, estimated by comparison of the average intensity to the intensity of identified single photon emitters. Error bars indicate standard deviation of the average pixel intensity.

Figure 8.7. Square fluence series used to estimate the damage related to the technique. a) SEM image of a square series directly after irradiation (52° tilt). b) Representative PL map (Sn) of the fluence dependent series. Scale bars are 5 µm.

Figure 8.8. Spectra taken from the centres of the squares shown in Figure 8.7(b). The number indicates the fluence mentioned in the text. (a) Si, (b) Ge, (c) Sn and (d) Pb.

Figure 8.9. AFM scans and depth profiles of the implanted squares for Si (a) and (b), Ge (c) and (d), Sn (e) and (f), Pb (g) and (h). The numbers denote the aforementioned fluences. The depth profiles are offset in the y-direction for better visibility. For each graph, the first profile corresponds to fluence 4, the second to fluence 5 and so on. The diagonal streaks visible in the AFM maps are polishing marks of the as-purchased diamond.

Figure 8.10 Determination of the beam diameter. a) A plain Si substrate was irradiated by spots with dwell times increasing column-wise from left to right. The scale bar corresponds to 1 µm. b) The normalised inverse pixel intensity of the average for the spots highlighted in (a). c) A Gaussian fit was used to approximate the ion beam shape. d) Direct comparison of measured and fitted beam shape.

Figure 8.11. Angular distribution of Ge atoms trajectories as they cross the thin-film diamond interface. The orientation of the angle relative to the thin-film diamond interface is shown in the inset.

Figure 8.12. A large area scan (10 x 10 array), was analysed by fitting 8 sub grids (4 x 4). In (a), (b), and (c) three examples of subgrids are shown. We note that the subgrids in the most right section (right 4 columns) excluded the top and bottom 4 points, due to a systematic deviation.

Figure 8.13. Spatial distribution of the dopants. (a) Distribution of the ensemble position (GeV) relative to the nominal implantation site, fitted by a Rayleigh function with a mode of (44 ± 4) nm. The inset shows directly the relative ensemble position. (b) Monte Carlo simulations of the depth distribution of Ge in diamond from a Xe+ recoil-implantation process and of the co-implanted Xe. (c) Schematic of the wedge edge to access the implantation profile of an area with the implanted species. (d) AFM map of the wedge prepared by EBIE. (e) PL map of the same Ge-implanted area. The positions of both maps were correlated by the three marked spots. Scale bars in (d),(e) correspond to 2.5 μm. (f) Average profile of depth (blue) and PL (red) along the wedge feature. The shaded areas represent the standard deviation.

Figure 8.14. Implantation of Eu into SiO_2. a) Fluence series with values as mentioned in the main text. b) Normalised Spectra from the square regions.

Figure 8.15. Implantation of rare earth ions into a commercial optical fibre. (a) Picture of the fibre used in this experiment. The end face is highlighted. (b) SEM image of the fibre end face during the implantation process. The yellow outline marks the boundary of the cladding to the ferrule, which was used to identify the core. The inset shows the core (back illuminated) relative to a correlation marker. The scale bar corresponds to 20 μm. (c) Emission of the implanted Eu3+, excited through the other fibre end (PL map shown as inset).

Abbreviations

hBN	-	hexagonal Boron Nitride
SPE	-	Single Photon Emitter
ZPL	-	Zero Phonon Line
PSB	-	Phonon Side Band
HBT	-	Hanbury-Brown and Twiss
APD	-	Avalanche Photo Diode
SPDC	-	Spontaneous Parametric Down Conversion
QKD	-	Quantum Key Distribution
QIP	-	Quantum Information Processing
CMOS	-	Complementary Metal Oxide Semiconductor
QD	-	Quantum Dot
CNT	-	Carbon Nanotube
TMD	-	Transition Metal Dichalcogenide
BNNT	-	Boron Nitride Nanotube
(N)IR	-	(near) Infrared
1D	-	1 Dimensional
2D	-	2 Dimensional
3D	-	3 Dimensional
NV	-	Nitrogen Vacancy
SEM	-	Scanning Electron Microscope
FIB	-	Focused Ion Beam
vdW	-	van der Waals

UV	-	Ultra Violet
UCNP	-	Upconversion Nanoparticle
CVD	-	Chemical Vapour Deposition
PMMA	-	Polymethyl methacrylate
AFM	-	Atomic Force Microscope
FWHM	-	Full Width Half Maximum
FDTD	-	Finite Difference Time Domain
NA	-	Numerical Aperture
BIC	-	Bound States in the continuum
PCC	-	Photonic Crystal Cavity
PE	-	Primary Electron
PLE	-	Photoluminescent Excitation
LPCVD	-	Low Pressure Chemical Vapour Deposition

Abstract

Quantum photonic technologies have an inherently disruptive potential for applications in sensing, computing and communication. A fundamental aspect is the manipulation of light on the nanoscale, where atomic scale defects can allow for the creation of quantum networks, enable quantum sensing, or provide chip scale devices for non-hackable communication. Towards such applications the fabrication and integration of quantum emitter is required, which is showed for two material systems in this thesis, hexagonal Boron Nitride (hBN) and diamond.

First, a route for monolithic device fabrication from hBN is developed with the realisation of photonic crystal cavities achieving Quality-factors up to 2000. As a potential tool to achieve spectral matching of emitter-cavity systems a direct write tuning technique via Electron Beam Induced Etching is demonstrated. Subsequently a deeper analysis of the developed fabrication method is given, with an emphasis on the fabrication artefacts that may occur under non-ideal processing conditions. Albeit the initial success of the monolithic device fabrication, a major hurdle for the integration of single photon emitter into photonic crystal cavities remained – the spectral matching of cavity modes and emitter emission wavelength. This obstacle was overcome by utilisation of single emitter in hBN grown by a chemical vapour deposition method. For this method hBN emitter preferentially exhibit an emission wavelength around 585 nm. This type of hBN was integrated in a hybrid fabrication scheme with Photonic Crystal Cavities from Silicon Nitride with Quality-factors up to ~ 3500. We observed up to 9 fold luminescence enhancement of single photon emitter at room temperature for cavity integrated emitters.

Beyond the integration of hBN single emitter a concept for photonic crystal cavities suitable for efficient integration of fluorescent nanoparticles is developed. In experiments the device integration of Upconversion Nanoparticles was achieved and displayed 20-fold photoluminescence enhancement and an estimate for the Purcell Factor of at least 60 was derived.

In the final part of this thesis a method for site specific creation of quantum emitters in solid state hosts is demonstrated. The technique, which is based on recoil implantation, was showcased for luminescent group IV colour centres in diamond, and facilitates the creation of single photon emitters at specific sites. This is relevant for future application in quantum photonics, which require integrated quantum emitter positioned at specific sites.

Chapter 1

Introduction

The 20th century was shaped by scientific developments that have not only brought a deeper understanding of our world but have granted us a lifestyle that was only imaginable by science-fiction writers at the start of that same century. Arguably, the fundament on which that development is built is quantum mechanics. Particularly, the understanding of how electrons behave in matter, how particles interact with each other, how we can manipulate them, or control the magnetic behaviour of materials - all these effects require an understanding of quantum mechanics to a certain degree. The formulation of quantum mechanics, was initiated by the interpretation of black body radiation by Max Planck, stating that energy is quantised. In his particular case it was in form of photons. This revolutionary idea, albeit introduced as a mere bridging tool to explain inconsistencies in the theory of black body radiation, was later followed by experiments, such as the photoelectric effect, the double slit experiment on electrons, and numerous others then revealed the intricate nature of quantum mechanics. Built upon experimental analysis and theoretical predictions, the framework of quantum mechanics evolved and allowed us to describe the very fundamentals of phenomena taking place at atomic scales. Followed by the establishment of the quantum mechanical framework, applications emerged in the second half of the 20th century. Among these applications were for example the invention of the transistor and the laser. In a historical context, the set of inventions and applications that harness some quantum mechanics effect have been commonly referred to as the first quantum revolution.[39] The hallmark of which is that such devices exploit some quantum effects for their operation. Whilst these gadgets and gizmos have brought us a long way in recent decades, we are now at the brink of the second quantum revolution. A central aspect of the second quantum revolution is the direct manipulation of quantum states, where the intention is not only to exploit some effect but to directly manipulate quantum states. The promise of the second quantum revolution are higher computing power, safe communication, and more accurate sensors. While some of these applications may require insurmountable engineering efforts, we in fact see the first steps towards some of these applications already been taken. A few recent highlights include the realization of fibre-linked quantum networks,[40] the establishment of satellite based quantum communication[41] and the first steps towards quantum computing.[42] However, this is a journey for humanity that is only

setting off now and therefore a collective effort is being directed to identifying suitable systems for such applications. Essentially, while our former century was determined by formulating the science, our current century is set to be age to engineer quantum systems.

The focus of this work lies on novel engineering and integration of quantum emitters and fabrication of photonic devices for on-chip applications. In the first chapters the theoretical framework and experimental fundamentals are established, upon which this work demonstrates several key achievements as outlined below.

Chapter 2 contains an introduction to the topic and a brief overview of some key components required for photonic quantum technologies, with a specific focus on solid state quantum photonics. This chapter covers the basics of quantum emitters, Photonic Crystal Cavities, and device integration.

Chapter 3 contains a brief overview of the utilised fabrication methods and principles of the experimental setups that were used during this thesis.

Chapter 4 contains our work on the fabrication of the first monolithic Photonic Crystal Cavities from hexagonal boron nitride. Significant portions of this chapter are copied verbatim from the peer reviewed article *"Photonic crystal cavities from hexagonal boron nitride."* Kim, Sejeong*, **Johannes E. Fröch***, Joe Christian, Marcus Straw, James Bishop, Daniel Totonjian, Kenji Watanabe, Takashi Taniguchi, Milos Toth, and Igor Aharonovich. *Nature communications* 9, no. 1 (2018): 1-8.

Chapter 5 contains an in depth view of the fabrication process and details for the fabrication of photonic nanostructures from hBN. Significant portions of this chapter are copied verbatim from the peer reviewed article *"Photonic nanostructures from hexagonal boron nitride."* **Fröch, Johannes E.***, Yongsop Hwang*, Sejeong Kim, Igor Aharonovich, and Milos Toth. *Advanced Optical Materials* 7, no. 4 (2019): 1801344.

Chapter 6 contains the hybrid integration of quantum emitters from CVD grown hBN into photonic crystal cavities from silicon nitride. Significant portions of this chapter are copied verbatim from the peer reviewed article *"Coupling Hexagonal Boron Nitride Quantum Emitters to Photonic Crystal Cavities."* **Fröch, Johannes E.**, Sejeong Kim, Noah Mendelson, Mehran Kianinia, Milos Toth, and Igor Aharonovich. *ACS nano* (2020).

Chapter 7 contains an alternative integration method into photonic crystal cavities using fluorescent nanoparticles. Significant portions of this chapter are copied verbatim from the peer reviewed article *"Photonic nanobeam cavities with nanopockets for efficient integration of fluorescent nanoparticles"* **Fröch, Johannes E.**, Sejeong Kim, Connor Stewart, Xiaoxue Xu, Ziqing Du, Mark Lockrey, Milos Toth, and Igor Aharonovich. *Nano Letters* 20, no. 4 (2020): 2784-2790.

Chapter 8 contains the development of a widely applicable direct ion implantation method using a standard Focused Ion Beam system, which is commonly available in Dual Beam Microscopes. Significant portions of this chapter are copied verbatim from the peer reviewed article *"Versatile Direct-Writing of Dopants in a Solid State Host through Recoil Implantation."* **Fröch, Johannes E.**, Alan Bahm, Mehran Kianinia, Zhao Mu, Vijay Bhatia, Sejeong Kim, Julie M. Cairney, Weibo Gao, CarloBradac, Igor Aharonovich, and Milos Toth. *Nature communications* (2020).

Chapter 9 gives an overall outlook of future development and applications of the developed techniques.

Chapter 2
Background

Over the last century, scientific development in quantum science has sparked the imagination and the compulsion of researchers to create concepts that could materialise into revolutionary applications. They are revolutionary in a sense, that these concepts, which are based on the sometimes unfathomable principles of quantum mechanics, can substantially outperform classical systems, be close to fundamental measurement limits, or offer ways of non-hackable communication.[43] In the following I will focus on quantum photonics, and introduce a generic picture of a single photon emitter and describe the specific material systems investigated in this thesis in more detail. Then, I will introduced the concept of Photonic Crystal Cavities and give a short overview of the state of integration.

2.1 Single Photon Emitters

In an abstract picture, a single photon emitter can be imagined as a two level system, as shown in Figure 2.1(a), where the ground state is occupied by a single electron. The electron can be promoted into an excited state by absorption of a photon from a laser with an energy equal or larger than the splitting of the ground and excited state. After some time the excited electron will relax into the ground state and emit a photon with the same energy, which would exhibit a delta like spectrum, corresponding to the energy difference between ground and excited state, shown in Figure 2.1(b). Although, such a picture is convenient to imagine the emission of a single photon stream, it lacks the manifold nuances of an actual system. Building our model of a single photon emitter, the electrons should be associated with a particular wave function corresponding to the ground and excited state, analogues to atomic orbitals, shown in Figure 2.1 (c). Wave functions and the transition between them underlie symmetry rules and quantum mechanical principals, which give rise to selection rules. One implication of selection rules is that the excitation and relaxation of the electron from ground to excited state and vice versa may involve a certain orientation of the electric field, denoted as the excitation and emission dipole. Thus the emitted photons can possess a distinct polarisation. On the other hand the excitation efficiency of a quantum emitter with a laser can be increased by matching the

excitation dipole. Furthermore, other orbitals may be present, for which radiative excitations/ relaxations between certain orbitals are forbidden. This can lead to non-radiative transitions, or so called non-radiative decay channels, which may decrease the effective emission of the emitter, as indicated in Figure 2.1(d). To increase the degree of reality for our model of a single photon emitter, one has to consider that orbitals may not only be occupied by a single electron, as well as their interaction with the environment, for example in a solid state crystal. The former can have two consequences, first that the orbital may be akin to a singlet, doublet, or triplet state, with spin degenerate states, second that the charge state of orbital can be changed by adding/ removing electrons, as shown in Figure 2.1(e). Finally, to complete this toy model, we take into account the interaction of the emitter with its environment and other aspects that will increase the linewidth of the emission. First of all, even for a pure 2 level transition, the emission spectrum would not be a pure delta function, but the linewidth would at the very least be limited by the lifetime of the electron in the excited state, due to the uncertainty principle. Second, the linewidth will further increase due the interaction with the phonon bath in the environment, called dephasing. Third, for a system in the solid state, phonons may be involved in the relaxation process. The main transition is then called Zero Phonon Line (ZPL), while for transitions where phonons are involved are denoted as the phonon side band (PSB). One should note that fluctuations in the environment may affect orbital properties, which can result in a shift of the emission wavelength. A more thorough basic introduction can be found in *Quantum Optics: An Introduction* by Fox.[44]

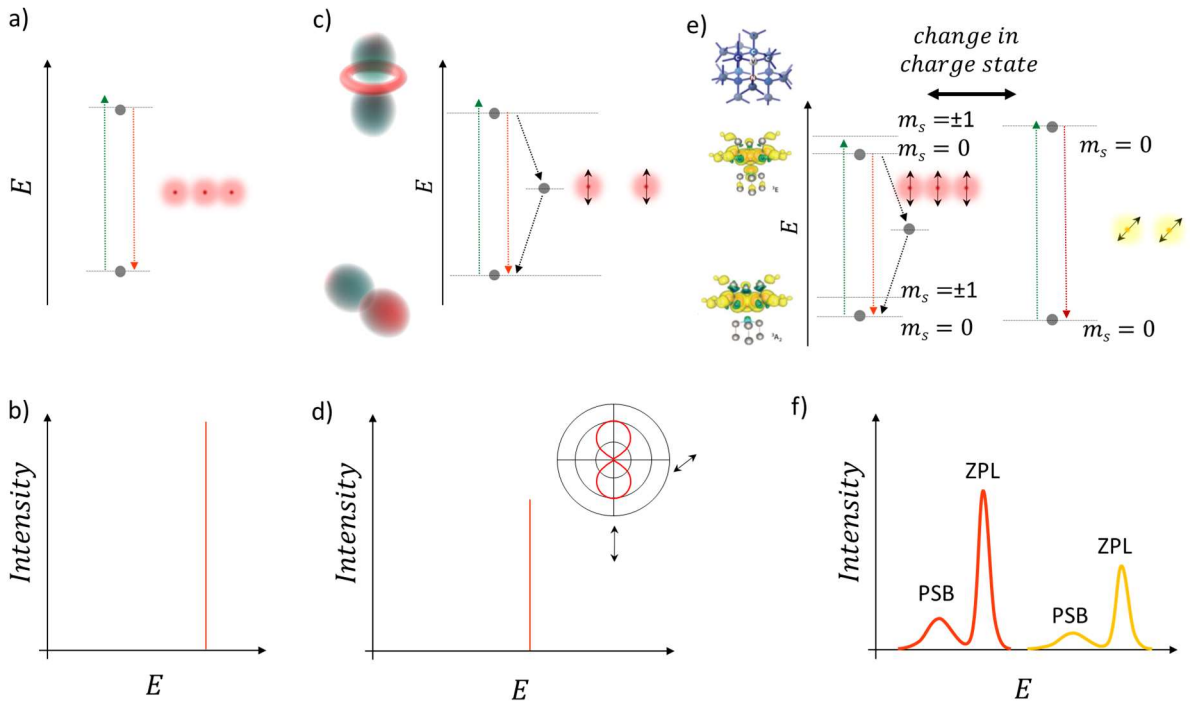

Figure 2.1 Toy model of a single photon emitter. (a) A naive picture of a single photon emitter, shown as a 2 level system, with a delta like spectrum shown in (b). (c) A refined system considering atomic orbitals and intermediate transitions. (d) The emission can be polarised, and may be decreased due to non radiative decay channels. (e) The system closest to reality, assuming an emitter in a solid state crystal with pecuilar shaped ground and excited state orbitals. The system may have spin multiplicity and different charge states. (f) A spectrum of such a system may thus have different main transitions, due to different charge states. Accompanying to the zero phonon line (ZPL) is the phonon side band (PSB).

A single photon emitter can be experimentally identified using a Hanbury-Brown and Twiss (HBT) setup, schematically shown in Figure 2.2(a). In this setup the single photon stream is split equally in two arms by a non-polarising 50/50 beam splitter. On both ends an avalanche photo diode (APD) is used to detect the incoming photons. Due to the particle properties of light, single photons are directed to either arm, but not both at the same time. Thus for a constant stream of photons, each detector will detect only a single photon at a time. To visualise the non-simultaneity of their arrival in both detectors, the signals of both detectors are time correlated. When APD A detects a photon ('click') then the time until a detection event at B is counted and the time difference is then visualised (Figure 2.2(b)).

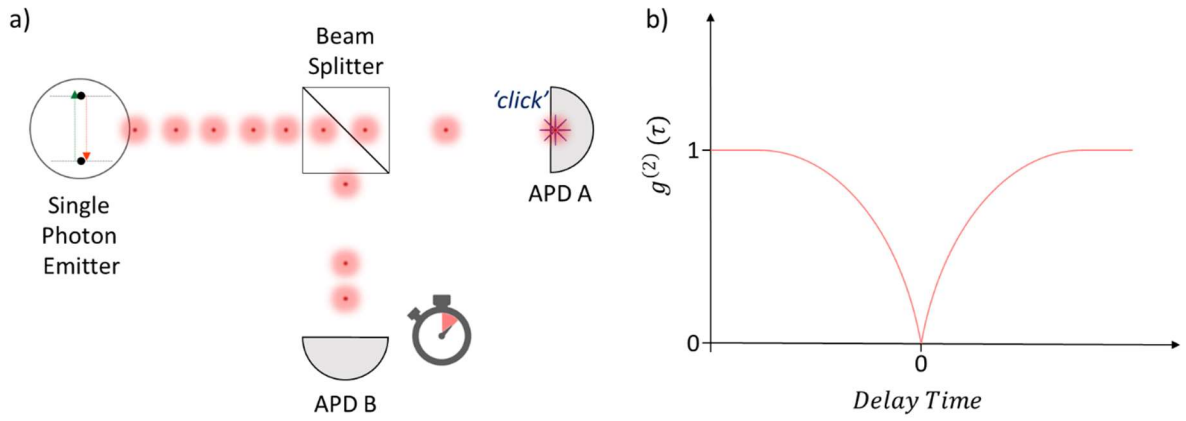

Figure 2.2. Identifying a single photon emitter. a) Schematic of a Hanbury-Brown and Twiss setup. b) The ideal autocorrelation curve collected from the background free emission of a single photon emitter.

Thus in the ideal case of single photons arriving equally spaced, one would expect zero correlation between the detectors at time t=0. This is in fact the 2nd order correlation function, given in Equation 2.1.

$$g^2(\tau) = \frac{\langle \hat{a}^\dagger(t)\hat{a}^\dagger(t+\tau)\hat{a}(t+\tau)\hat{a}(t)\rangle}{\langle \hat{a}^\dagger(t)\hat{a}(t)\rangle^2} \qquad (2.1)$$

Here, t is the arrival time of the first photon, τ the time until the second photon arrives, $\hat{a}^\dagger$ and $\hat{a}$ are the creation and annihilation operators, respectively. It can then be shown, that for photon number states, Equation 2.2 can be derived. While for coherent light $g^2(0) = 1$ and for classic (chaotic) light one obtains $g^2(0) = 2$.

$$g^2(0) = 1 - \frac{1}{n} \qquad (2.2)$$

Where n is the number of photons arriving at the beam splitter. Hence, for the case of photon number states, the dip of the 2nd order correlation function can be used for their identification, e.g. if n=2, then $g^2(0) = 0.5$. One should note that if background luminescence is collected at the same time as the emission of the single photon emitter, then the dip of the autocorrelation curve will not reach 0 but will be higher and may take any continuous value between 0 and 1, depending on the signal to background ratio. In particular, although it is commonly accepted that a $g^2(0)$ dip below 0.5 indicates the presence of a single photon emitter, several emitters with differing brightness may be present, which can as well lead to a dip below 0.5 as for

example studied in the case of single photon emitter in hBN.[45] Moreover, care has to be taken regarding the normalisation of the autocorrelation curve. As for the occurrence of bunching the value of the autocorrelation curve for delay times larger 0 can be greater than 1. Therefore, one has to ensure that the curve is normalised for longer delay times.

Moving from our toy model to actual systems, plenty of different single photon sources has emerged over the years. Based on their physical state these are, spontaneous parametric down conversion and attenuated laser sources, single photons from ions or cold atoms, and single photon emitters in the solid state. For completeness, the former two types will be described shortly, while the latter one be discussed thoroughly.

Spontaneous parametric down conversion (SPDC) is a non-linear process in which a photon, from an incoming laser, is converted into 2 photons with lower energy (half of the incoming photon), having complementary momentum and polarisation, which are entangled under careful consideration of the collection angle. Advanced laser technology allows for a high temporal stability of emitted photons (i.e. absence of spectral diffusion) and a narrow emission linewidth. [46] Therefore due to their properties, such photons are particularly attractive for Quantum Key Distribution (QKD) and for some applications in quantum information processing (QIP). For the former SPDC sources have been exploited in the last decades to demonstrate QKD through fibre links as well as satellite based operation for distances over 1200 km.[41] For QIP, recent efforts have demonstrated for example realisation of quantum neural networks[47] and quantum photonic processors[48]. Although the SPDC process is in essence spontaneous, through engineering efforts, constant and high generation rates are achievable and on chip integration also have been achieved. [46] However, the major drawback is their lack in a spin-photon interface, which is required for applications as quantum memories.

Cold atoms and trapped ions are probably the most elemental single photon sources.[49] These sources have been the essential building block for quantum optics experiments during the late 20th century, with some of the fundamental experimental demonstrations evidenced in these systems, honoured with the Nobel Prize for Serge Haroche and David J. Wineland in 2012. During this time period experiments were conducted on streams of atoms which passed through a mirror arrangement (an optical cavity), which allowed to study their interaction with light. However, in recent efforts the different properties of neutral atoms and ions have been more fundamentally exploited with work towards on chip integration of ions by electronic chips[50]

as well as miniaturization of optical traps for neutral atoms and their integration with photonic nanostructures.[51,52] While overall these source are advantageous due to identical properties of atoms and their identical emission, the integration into on-chip devices is arduous or in the case of neutral atoms not possible at this point and requires larger experimental setups.

Single photon sources in the solid state have attracted attention since the early 2000s, due to their promise for simple on-chip integrability, and potential spin properties, which enables application as quantum memories.[53,54] These sources can be subcategorised with respect to the solid state host and the characteristics of the emitter. At this point some of the most studied sources, are shown in Figure 2.3, (a) semiconductor quantum dots, (b) defects and ions in 3D crystals, and (c) defects and bound excitons in 1D and 2D materials. For thorough reviews on solid state single photon emitters, I refer the reader to Aharonovich et al,[19] Bassett et al.,[55] and Toth et al.,[56] for a specialised review on single photon emitter in 2D materials.

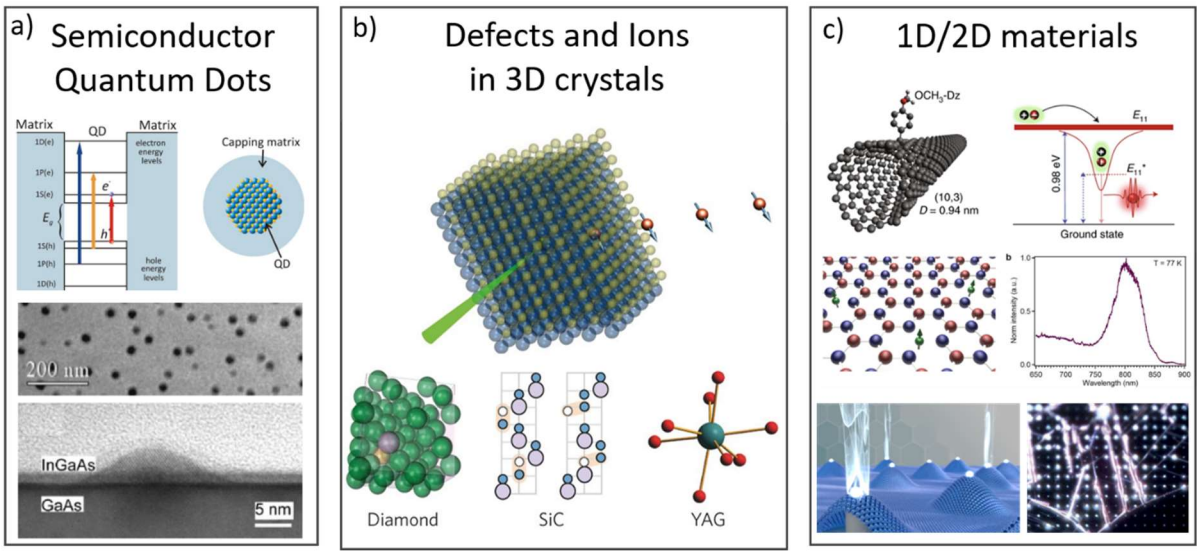

Figure 2.3 Single Photon Emitter in the solid state.(a)Semiconductor Quantum Dots are localised 0D systems with a confined bandgap, causing the exciton to act as an SPE. (b) Defects and ions in 3D crystal can act as single photon emitter, such as diamond, SiC, or YAG. (c) Defects and bound exciton like single emitter in low dimensional materials, such as in carbon nanotubes, hBN, or strained WSe_2. Reproduced from (a) - [17,18], (b) - [19], (c) - [13,20,21]

Semiconductor quantum dots are spatially confined systems with a bandgap smaller than the surrounding material.[57] If the size is smaller than the exciton Bohr radius, the electron wave function is spatially localised and acts as a single photon emitter. In bulk materials, a reduced band gap can be achieved by a variation in the stoichiometry, e.g. InGaAs in GaAs quantum

dots. Although semiconductor quantum dots are appealing due to their sharp emission lines, and their compatibility with CMOS electronics, enabling their manipulation in a p-i-n architecture, their major disadvantage is inhomogeneous line broadening. This causes the emission lines of several quantum dots to be detuned from each other, which is detrimental to applications that require several QDs to be interfaced.

In contrast, point defects in wide band gap materials are appealing because of their potential to achieve single photon emitters with intrinsically identical properties in the future, which follows from the assumption that the same defect is fully reproducible at different sites. Such emitters can be understood as a spatially localised electron wave functions, which introduce discrete energy states within the bandgap of the material. Among the most promising systems thus far are colour centres in diamond[58], further discussed below, and Silicon Carbide[59]. A further class of single emitter in 3D crystals are rare earth ions in crystal hosts[60]. This case is different to defect based emitters, as the emitter properties are almost fully determined by the rare earth ion. In this case the transition of interest for generation of single photons and spin-interfacing is an atomic transition within the 4*f* shell. The main requirement on the crystal host in this cases is to provide an adequate configuration of the bonding orbitals to guarantee proficient shielding of the relevant 4*f* shell transitions.

Material systems with single photon emitters in 1D and 2D materials include carbon nanotubes (CNT)[20], Transition Metal Dichalcogenides (TMD)[61-65], boron nitride nanotubes (BNNT)[66] and hexagonal Boron Nitride (hBN)[24]. In CNTs, single photon emitters are defect bound excitons which are stable at room temperature and have emission in the IR range. For 2D TMDs it is currently assumed that single photon emitters are bound excitons, arising from strain. This has been utilised by placing the 2D material atop of pillars for site specific emitter creation.[21] While recent studies in MoS_2 also suggest that single emitters in these materials can emerge by creation of vacancies.[67] Single photon emitter in hBN and BNNT are currently understood as point-like defects, similar to defects in diamond, and will be discussed more thoroughly below.

Before detailing colour centres in diamond and hBN, it is to say that at this point in time, there is no ideal single photon source, which checks all marks, and the search for it is still an ongoing effort. Specifically, as mentioned in recent viewpoints,[68,69] the ideal single photon source

ought to fulfil the points listed below. While the first 3 points are stringent requirements, the latter can be seen as favourable characteristics:

- On-demand emission of single photons, with only one emitted photon per excitation event
- High collection efficiency of emitted photons
- Indistinguishability of emitted photons, such that polarization, energy, spatial mode are identical
- Gigahertz repetition rate allowing for fast operations
- Tuneable emission wavelength
- Electrical triggering
- Emission into a Gaussian mode for near-unity coupling

As such the identification and characterisation in new materials is also ongoing. Other materials that are studied for single emitters include for example defects in ZnO,[70] ZnS,[71] GaN[72] and AlN,[73] perovskite quantum dots,[74] or single molecules[75].

2.1.1 Diamond

Diamond is a fascinating material system in many aspects, where simplicity in stoichiometry and crystal structure give rise to a range of peculiar physical characteristics. Amongst others, it is being regarded as the hardest natural material, chemically inert and robust, as well as being a wide band gap insulator. For a long time different colours of diamond have been known and are used as gem stones, such as the argyle diamond, which appears in a faint pink. The different colours arise from luminescent point defects in the diamond, therefore have been dubbed colour centres. Among the range of known colour centres some have been particularly intriguing due to spin properties. As the prototypical case that has been studied widely is the Nitrogen Vacancy (NV), as shown in Figure 2.4(a).[22,76] What makes this defect so particularly interesting, is the level structure associated to the defect in its negative charge state with the ground and excited state being triplet states, shown in Figure 2.4(b). The splitting in the ground triplet state is 2.87 GHz, and a transition between these states can be driven by applying a microwave field. In addition to the triplet ground and excited state, further energy levels in the energy diagram can allow for a recombination at 1024 nm. The relaxation to this excited state occurs only when the system is in the $m_s = \pm 1$ excited state. Thus under the application of a microwave field with a frequency of 2.87 GHz the typical PL emission around 637 nm drops,

due cycling through the transition at 1024 nm. The degeneracy of the $m_s = \pm 1$ state can be lifted by applying a magnetic field, i.e. Zeeman splitting, which then changes the PL contrast with respect to the applied microwave field. In addition to its negative charge state the NV centre can also occur as a neutral charge state, with a ZPL at 575 nm. Charge state switching between these states can occur upon photoionization or electronic modification of the environment by introduction of donor states or a shift in the band alignment.[77-80] However, the neutral charge state does not display the same spin properties as its negatively charged counterpart, and has been far less extensively studied.

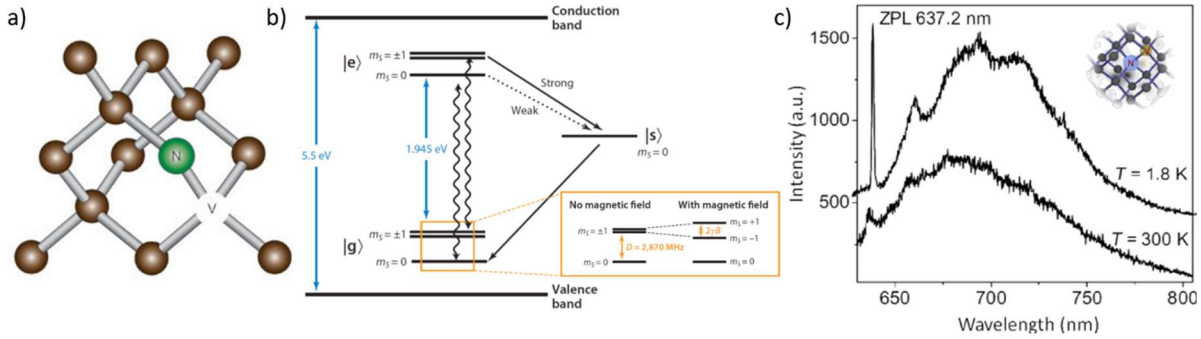

Figure 2.4 The NV centre in Diamond.(a) The crystallographic structure of the NV centre. (b) The associated level structure of the NV centre. (c)The PL spectrum of the NV centre at room temperature and cryogenic temperature. Reproduced from (a),(b) - [22], (c) - [81]

Due to its properties, this defect in its negative charge state has been extensively studied since its initial characterisation. Some applications lie on hand, such as the sensing of magnetic fields by exploiting the level splitting and measuring a shift in the microwave frequency. In addition this defect is interesting for applications in quantum networking, where it can be utilised as a spin quantum bit (Qubit). Although the level structure is promising for quantum application, some other properties are detrimental. Particularly the emission into the ZPL is only about 1 - 10 % at room and cryogenic temperatures, as shown in Figure 2.4(c). Although the absolute intensity of the ZPL increases at cryogenic temperature, due to the linewidth narrowing the total fraction of emission into the ZPL only increases marginally with reports stating overall emissions into the ZPL of 3 - 10 % at cryogenic temperatures.[82-85] Albeit efforts to increase the emission into the ZPL through photonic crystal cavities, over the years another class of defect has become increasingly relevant - the group IV colour centres.[23] These consist of a group IV element (Si, Ge, Sn, or Pb) located in between two vacancies, as shown in Figure 2.5(a). Compared to the NV, these colour centers are particularly attractive, due to their higher

Debye Waller factor, the narrow ZPL even at room temperature (Figure 2.5(b)), as well as their ground and excited state splitting (Figure 2.5(c)), making the defect accessible for spin manipulation. In addition, the symmetric defect configuration makes these emitters less susceptive to environmental disturbances, such as electric field fluctuations due to nearby charge traps, which can cause spectral diffusion.

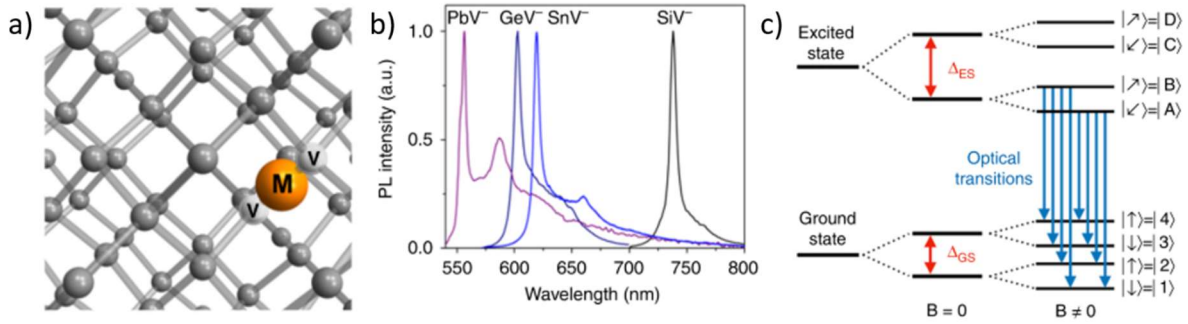

Figure 2.5 The group IV colour centres in diamond. (a) The archetypical defect configuration of the group IV split vacancies. M indicates one of the atoms, Si, Ge, Sn, Pb, V indicates a vacancy. (b) Spectra of the PbV, GeV, SnV, and SiV.(c)The related level structure of the group-IV defects. Reproduced from [23]

The interest into these colour centres was initiated by Elke Neu, who showed that single SiV colour centres are achievable, with a narrow emission line at room temperature.[86] Followed by this initial report, effort was put forward to engineer this particular quantum system through optimization in the material growth and processing. Among others Alp Sipahigil et al. achieved several ground breaking works with the SiV, such as the demonstration of indistinguishable photons from 2 separate SiV centres,[87] as well as the spin manipulation of individual SiVs inside a photonic crystal cavity[88] and superradiant emission of entangled SiV centres[89]. In essence these works demonstrated the potential of the SiV in a quantum photonic network.

Yet, aspects of the defect centre remain disadvantageous, such as its low quantum efficiency, a high non-radiative recombination rate, as well as the requirement for millikelvin operation for spin manipulation, due to the small splitting in the ground and excited states. This motivated further studies of other group IV colour centres, which have larger level splitting. Therefore their spin properties are accessible at slightly higher temperatures, alleviating the stringent requirement of a ^{3}He/^{4}He dilution refrigerator. At this point the GeV was identified with emission at ~ 602 nm,[90] the SnV with emission at ~ 620 nm,[91,92] and a Pb related centre with a ZPL around 550 nm[93,94]. The GeV is attractive for its high quantum efficiency of at

least 20 %,[95] and has been successfully studied in terms of its spin properties,[96] although the ground and excited state splitting are still narrow and require millikelvin operation. Therefore, recently the SnV and PbV have attracted more attention. With recent efforts towards materials engineering to improve colour centre properties, such as high pressure high temperature annealing[92] or material overgrowth[97]. In this ongoing effort, transform-limited photons from a SnV have recently been achieved.[98]

2.1.2 Hexagonal Boron Nitride

Hexagonal boron nitride (hBN) is a wide band gap (~6 eV) van der Waals material, which consists of 2D sheets with Boron and Nitrogen arranged in a hexagonal alternating manner, as depicted in Figure 2.6 (a). In 2015 the first quantum emitters of this material were identified in multi- and monolayers with a ZPL around 625 nm, shown in Figure 2.6 (a).[24] The displayed 2nd order autocorrelation (c) showed a value of < 0.5, a signature for a single photon source. Over the short time period since their discovery, already massive information about single photon emitters could be collected, thanks to the less restrictive and convenient property of room temperature operability. Moreover, samples of hBN are available at a cheap price, either as nanoparticles in solution, or grown as crystals by chemical vapour deposition in a tube furnace or other methods. Similar to diamond, single photon emitter in hBN appear with different emission wavelengths, which span the range from UV,[25] up to the NIR[27], as shown in Figure 2.6 (d),(e), and (f), respectively . However, the ZPL distributions of emitters in hBN appear to be multimodal and relatively broad, as shown in Figure 2.6 (g).[28] The broadness of these distributions may be related either to strain within the crystal, nearby charge traps causing spectral shifts due to the Stark effect, or surface charge transfer from physisorped species. The different positions in emission distributions likely corresponds to different origins in defect structure. Particularly, at this point the origin of most single photon emitting defects in hBN are still under debate. Among the complications for their clear identifications is the fact that emitters can be created/ activated by virtually any process that alters the material. In the original work by Tran et al, it was shown that hBN emitters from CVD grown monolayers and from particle solution can be created/activated by annealing at 850 C°.[24] In subsequent works it was demonstrated that irradiation with low[26,99] and high energetic electrons,[100] as well as ions,[101,102] strain engineering,[29] laser irradiation,[103] plasma exposure,[104,105] and chemical treatment[106] could also activate or create Single Photon emitters in hBN.

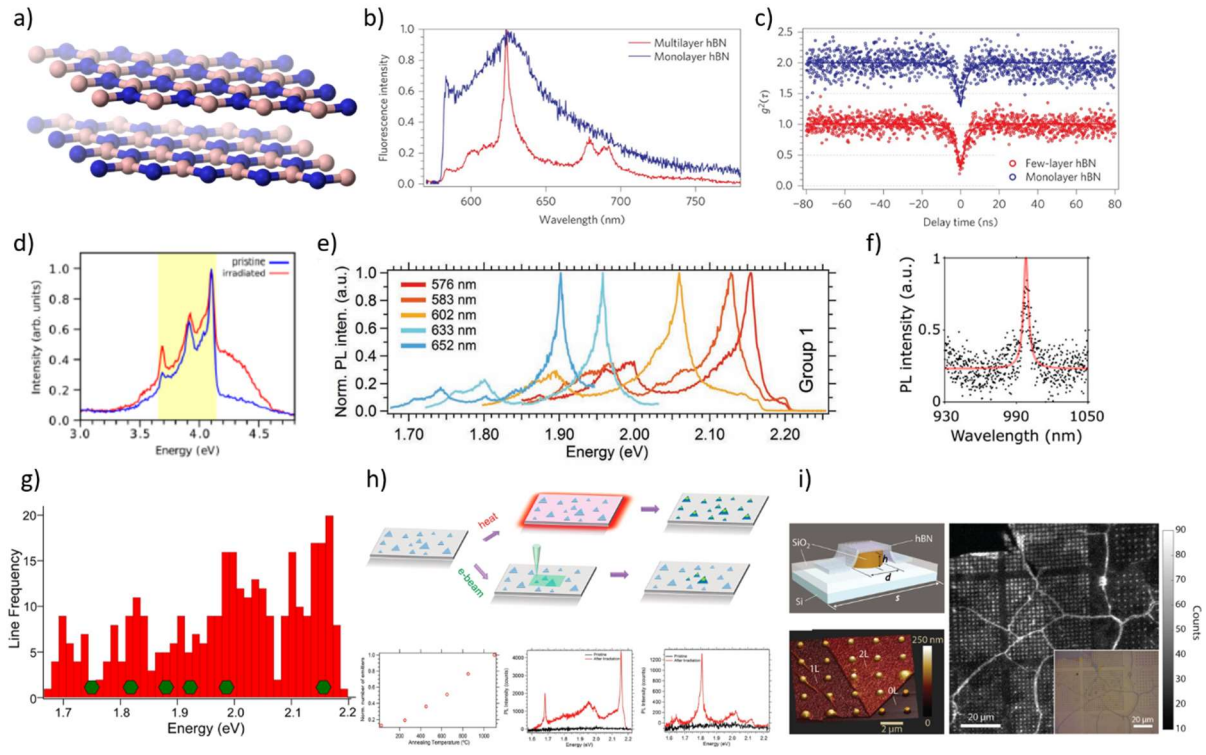

Figure 2.6 Single Photon emitter in hBN. (a) The atomic structure of hBN with Nitrogen and Boron indicated as blue and pastel spheres, respectively.(b) The spectra of the initially identified SPEs in multi- and monolayer hBN, red and blue, respectively. (c) The g^2 measurement of the related emitters, shown in (b). The graphs are offset by 1 for clarity. (d) Emission of a hBN single emitter in the UV, identified by TEM cathodoluminescence. (e) SPEs in the visible range. (f) A hBN SPE in the NIR regime. (g) Multimodal distribution of the ZPL in the visible range. The green hexagons denoted specific emitters that were further characterized in that work in HBT measurements. (h) Creation of Emitter through annealing or electron beam irradiation. (i) Site specific creation of emitter through strain engineering. Reproduced from (a-c) - [24], (d) - [25], (e),(h) - [26], (f) - [27], (g) - [28], (i) - [29]

The only hBN defect that has been unambiguously identified, is the VB^-,[107] a vacancy located at a boron site, which can be simple generated by irradiation with ions,[13] as schematically shown in Figure 2.7(a). In this case a hBN flake was irradiated with a Xenon Focused Ion Beam, as shown in Figure 2.7 (b). From irradiated areas the broad emission of this defect is observed, centred at 825. However, it remains unclear, whether it corresponds to the defect ZPL or a PSB. This centre also possesses ODMR, as shown in Figure 2.7(d), with a Zero Field Splitting of 3.47 GHz. Single photon emission from this defect could thus far no be detected.

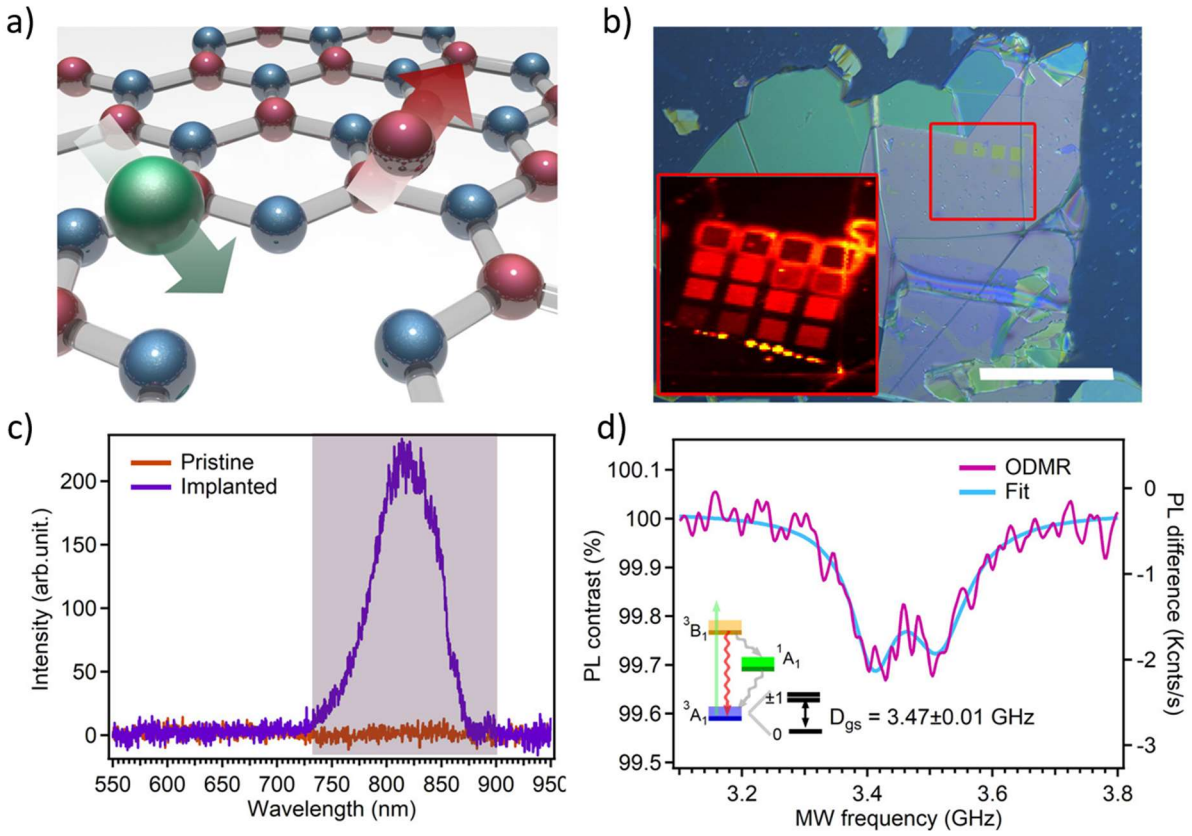

Figure 2.7 The VB- emitter in hBN. (a) Creation of the defect through ion beam irradiation. (b) A hBN flake after irradiation, with an inset showing a PL map, with the irradiated regions appearing bright. The scale bar corresponds to 20 µm. (c) The spectrum of the VB- defect. (d) PL contrast of the emission in ODMR. Reproduced from [13]

In the search of the defect origin for other SPEs in hBN, recently Mendelson et al. showed that emitters in CVD-grown hBN exhibit a ZPL primarily around 585 nm,[30] as shown in Figure 2.8(a). Furthermore, by comparison of different growth conditions and techniques (Figure 2.8(b)), it was shown that Carbon is either directly involved in the defect, or at least required for its activation.[31] This is supported by several theoretical works, which deduce a carbon related defect as the most likely candidate for a SPE with emission around 600 nm.[108]

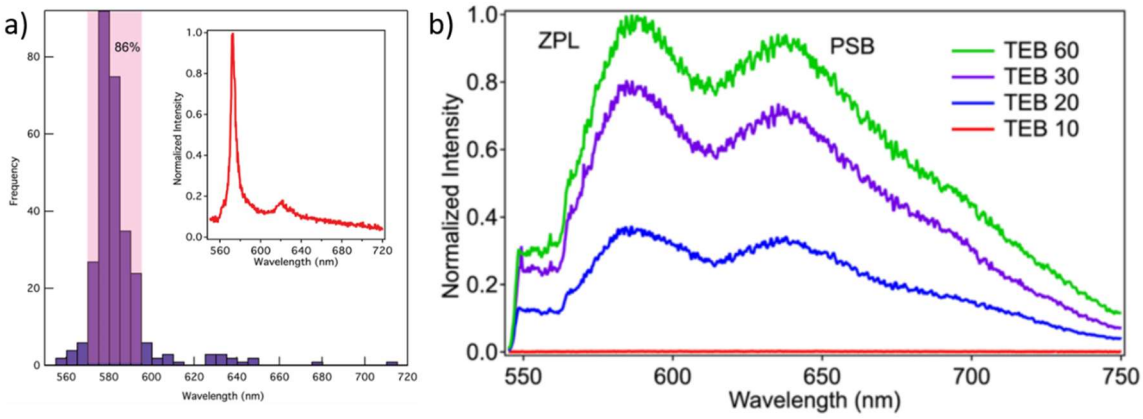

Figure 2.8 Other colour centers in hBN.(a) CVD grown hBN predominantly exhibit a ZPL with emission around 585 nm. (b) Emission of hBN colour centre in MOVPE growth with different doping flow of a carbon precursor (TEB). Reproduced from [30,31]

2.2 Photonic Crystal Cavities

Photonic crystal cavities (PCCs) are a key part in some on-chip applications of quantum emitters, required either for the enhancement of the emission or as a non-linear light-matter interface. Essentially two concepts of photonics are combined within, the photonic crystal and the optical cavity. The concept of photonic crystals emerged in 1987, by works of Eli Yablonovitch[109] and Sajeev John[110] and can be understood as the photon analogue of electronic semiconductors and insulators. In detail, the general solution for the propagation of an electromagnetic wave is given through Maxwell's Equation, which can be combined into Equation 2.3 - the Wave Equation.

$$\nabla \times \nabla \times \boldsymbol{E}(\boldsymbol{r}) = \left(\frac{\omega}{c}\right)^2 \varepsilon(\boldsymbol{r})\boldsymbol{E}(\boldsymbol{r}) \qquad (2.3)$$

Where, $\boldsymbol{E}$ is the electric field vector, $\boldsymbol{r}$ is the position vector, ω is the frequency, and ε the dielectric constant. For a medium with a periodic ($\boldsymbol{a}$) variation of the dielectric constant (Equation 2.4), the solutions for the Wave Equation have to obey Bloch's Theorem (Equation 2.5).

$$\varepsilon(\boldsymbol{r}) = \varepsilon(\boldsymbol{r} + \boldsymbol{a}) \qquad (2.4)$$

$$\boldsymbol{E}(\boldsymbol{r}) = e^{-i\boldsymbol{k}\boldsymbol{r}}\boldsymbol{u}_{\boldsymbol{k}}(\boldsymbol{r}) \qquad (2.5)$$

With $\boldsymbol{k}$, as the wave vector and $\boldsymbol{u_k(r)}$ as the periodic component of Equation 2.5. The wave equation is solved (typically numerically) for a range of frequencies ω to find the respective components of $\boldsymbol{k}$. This relation is known as the dispersion relation $\omega(\boldsymbol{k})$, which describes how the solutions of the wave equation, i.e. certain modes, propagate through a medium, as shown in Figure 2.9(a) for a photonic crystal in 3D dimensions. Whereas modes in general describe a pattern of an oscillatory motion, for light it describes the pattern of electric and magnetic field distributions relative to their propagation. A collective of modes is called a band and under certain conditions, a range of frequencies exist without a solution - a band gap. The band below the gap (smaller ω) is called the dielectric band, while the band above is called the air band (larger ω). This nomenclature arises from the localisation of the energy of modes within the photonic crystal. For modes of the air band, the energy is primarily localised within the region with lower refractive index (being more air like), while for the dielectric band the energy is localised in the high index region (being more dielectric like). Based on the mode pattern one can also distinguish 2 principle types of modes, which are the Transverse Electric (TE) and Transverse Magnetic (TM) modes. For a TE mode no electric field exists in the propagation direction, while for a TM mode no magnetic field component exists in the propagation direction. One should note that a band gap can be achieved for either the TE or TM modes, in case it is present for both types, it is denoted as a full band gap, as there exists no light wave that can propagate through that crystal. The principles of a 3D photonic crystal can be translated to lower dimensions, by light confinement through total internal reflection (TIR) in the confined dimensions, e.g. for a photonic crystal slab, as shown in Figure 2.9(b). In this case we have to consider that light with a wave vector larger than the critical angle (i.e. no TIR) is not confined within the structure and will couple out, i.e. radiative loss. This boundary is called the light line, and the region for which $\boldsymbol{u_k(r)}$ is larger than the critical angle is denoted as the light cone. Light within this region is not confined within the photonic crystal. Yet, under certain conditions, resonances within the light cone can be localised in the photonic crystal, called therefore Bound States in the continuum (BIC). As these resonances are not topic of this thesis, I refer to Chia Wei Hsu et al.[111] for an in depth review of BICs. Furthermore it is to add that for 1D and 2D photonic crystals the modes are identified as TE-like and TM-like, since the TE and TM properties occur only at the centre of the slab but deviate at the slab boundary.

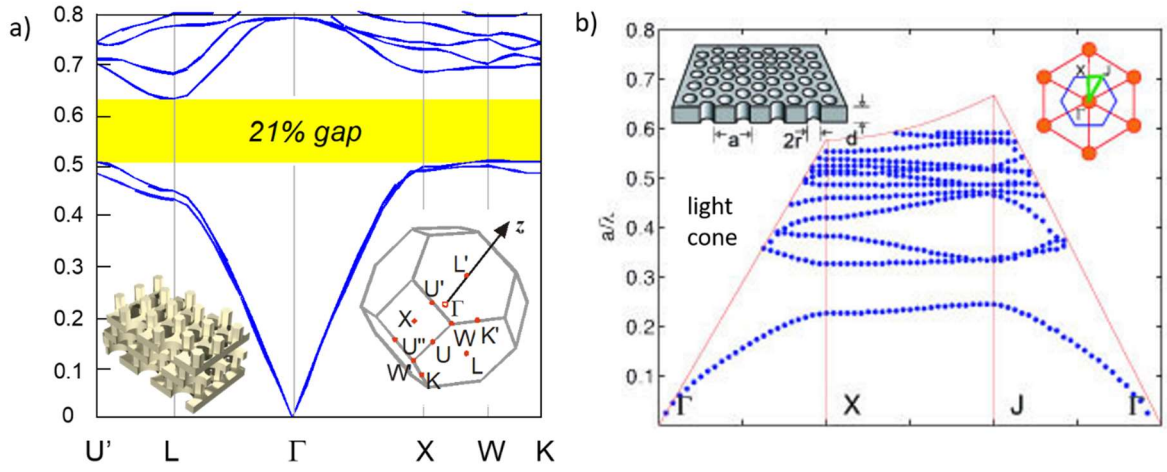

Figure 2.9 The band diagram of Photonic crystals. (a) Dispersion relation of a 3D photonic crystal, with a full band gap for a structure as shown in the bottom left inset. Symmetry points of the crystal are defined in the bottom right inset. (b) Dispersion relation of a 2D photonic crystal, as shown in the inset top left, with symmetry points defined by the top right inset. Solutions for the wave equation that are not confined in the slab, which lie inside the light cone, are not depicted. Reproduced from [32,33]

The second principle that is exploited in a PCC is the optical cavity. An optical cavity is a setup of mirrors, which supports the formation of a standing wave of light under the condition that the optical path length is a multiple of the wavelength, which allows it to act as a resonator. Main attributes of the optical resonator are the quality factor (Q-factor) and the mode volume (V_{mode}). The former is an indicator of the damping, i.e. how well the energy of a resonance is stored in the cavity, while the latter describes the extent of the field that is confined within that resonator.

The Photonic Crystal Cavity is thus the conceptual combination of these principles, demonstrated as a 2D PCC structure with air holes in Figure 2.10. The simplest design consists of a photonic crystal with one repeating element changed at its centre. This change in the crystal periodicity can be seen as a defect being introduced, with an associated mode. Depending on whether that defect arises due to a shift of the dielectric band upwards or a shift of the air band downwards, it is characterised as an acceptor or donor cavity, analogues to semiconductor physics. Due to the isolation of the defect in the band, the photonic crystal around acts as mirror, thus forming a cavity for that particular wavelength. Over time, since the first PCCs were fabricated, the design guidelines refined and instead of the introduction of a single defect it was

found that a less abrupt change in the photonic crystal periodicity would confine the light better, as scattering is reduced due to a gradual change in the periodicity. A tapered design was typically used throughout the thesis.

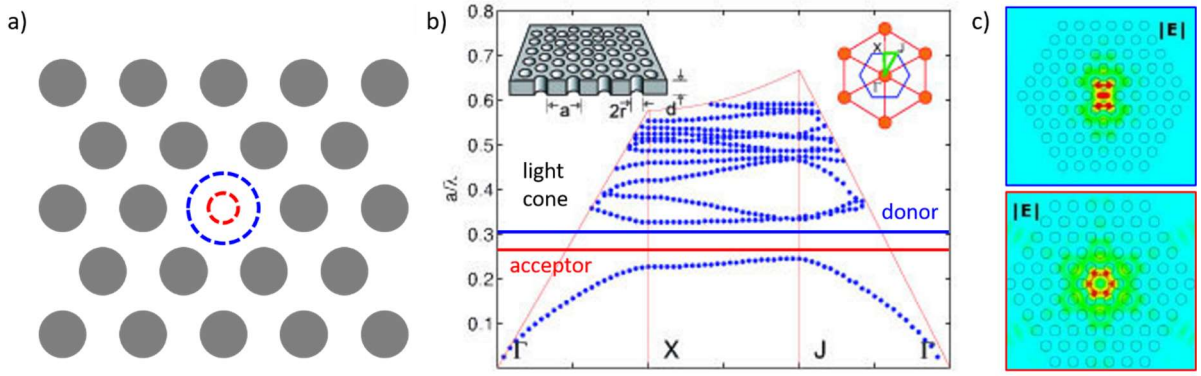

Figure 2.10. Example of a Photonic Crystal Cavity. (a) A PCC is achieved by introducing a defect into a photonic crystal. In this case by increasing (blue) or decreasing (red) a hole at the centre. Grey circles represent air holes in a dielectric slab. (b) In the corresponding band diagram defect states emerge, known as acceptor or donor states, corresponding to an increase or decrease in the centre hole size, respectively. (c) Representative field distributions for the corresponding mode associated with the defect. Reproduced from (b) - [33], (c) - [34]

As compared to an optical cavity, the PCC is integratable on a chip scale with a significantly smaller mode volume (Equation 2.6) typically on the order of the diffraction limit.

$$V_{mode} = \frac{\int\int\int \varepsilon(\vec{r})\left|\vec{E}(\vec{r})\right|^2 d^3\vec{r}}{max\left(\varepsilon\left|\vec{E}(\vec{r})\right|^2\right)} \qquad (2.6)$$

Regarding the Quality factor of real PCCs in measurements, for designs with sufficiently extended mirror regions the Q-factor is typically limited by material absorption, or scattering losses at the top/ bottom surface.

If an emitter is integrated into the cavity then the interaction is typically described in the framework of the Jaynes-Cummings model with a Hamiltonian given as Equation 2.7 assuming emitter and cavity to be in resonance ω. For the derivation of the individual terms, see Vuckovic[34].

$$\hat{H} = \hat{H}_E + \hat{H}_F + \hat{H}_{int} \qquad (2.7)$$

$$\hat{H}_E = \frac{\hbar\omega}{2}\sigma_z \qquad (2.8)$$

$$\hat{H}_F = \hbar\omega\left(a^\dagger a + \frac{1}{2}\right) \qquad (2.9)$$

$$\hat{H}_{int} = i\hbar\left(g^*(\vec{r_e})a^\dagger\sigma_- - g(\vec{r_e})\sigma_+ a\right) \qquad (2.10)$$

$$g(\vec{r_e}) = \frac{\mu_{eg}}{\hbar}\sqrt{\frac{\hbar\omega}{2\varepsilon V_{mode}}}\,\frac{E(\vec{r_E})}{|E(\vec{r_M})|}\,\frac{\vec{\mu}_{eg}\cdot\hat{e}}{\mu_{eg}} \qquad (2.11)$$

In this case $\sigma_z = |ex\rangle\langle ex| - |g\rangle\langle g|$ is the population operator, with $|ex\rangle$ and $|g\rangle$ representing the energy eigenstates of the emitter, $\sigma_+ = |ex\rangle\langle g|$ and $\sigma_- = |g\rangle\langle ex|$ are the transition operators, $g(\vec{r_e})$ is the coupling parameter with μ_{eg} being dipole moment, and $\hat{e}$ being the unitary electric field vector at the emitter location. In the resonant case, we distinguish 2 cases for this system, known as the strong and weak coupling regime. Furthermore, we also have to take into account the cavity loss rate and the emitter decoherence rate, with the former arising due to a imperfections in the cavity and the latter due to decay through non resonant channels. In the strong coupling regime ($g > \kappa, \gamma$) the emitter and cavity form hybrid states, which deviate from the harmonic ladder of the isolated systems. Specifically, when emitter and cavity are in resonance one can observe a splitting of the coupled state, known as Rabi splitting. In this case a coherent energy exchange of emitter and cavity takes place. The strongly coupled system can serve as a gate by exploiting the anharmonicity of the states. In the weak coupling regime, one will observe an enhancement of the emitter emission, which can be understood by considering that the cavity increases the local density of optical states. As stated by Fermis golden rule, the transition between two states is proportional to the density of states, which therefore leads to a reduction of the emitter lifetime. The enhancement of the emitter, as compared to its free space emission is given in Equation 2.12, known as the Purcell factor, which becomes Equation 2.13 if the emitter is positioned at the field maximum and the dipole and mode polarisation are aligned.

$$F = \frac{2|g|^2/\kappa}{n\Gamma_0} \qquad (2.12)$$

$$F = \frac{3}{4\pi^2}\left(\frac{\lambda}{n}\right)^3 \frac{Q}{V_m} \qquad (2.13)$$

2.3 Device Integration

The on-chip utilisation of quantum emitters in practical devices requires integration with a range of photonic components, achievable either by monolithic or a hybrid design. In the former an emitter is integrated directly within the functional device consisting of the same material. Particularly semiconductor quantum dots seemed suitable for this approach, due to mature semiconductor fabrication protocols, allowing to integrate single photon sources with waveguides[112], phase shifter,[113] and structures for tuning.[114] This allowed the study of light matter interaction with Semiconductor QDs in the strong coupling regime[115] and demonstration as gates[116-118]. More recent examples for monolithic emitter integration were demonstrated by integrating SiV colour centres in diamond cavities, as well as rare earth ions in YVO_4 cavities. Among others a quantum photonic switch at the single photon level and coherent interaction between colour centres in a cavity was achieved.[88,89,119-124]

A key for monolithic integration is the creation of the quantum emitter at a particular site. Particularly, for defect centres in the solid state, ion beam implantation is commonly used. To enable the site specific generation of emitters, various techniques have been employed in order to minimise the area that is implanted, such as implantation through a mask,[35] or through a pierced AFM tip,[36] which acts as an aperture. Alternatively Focused Ion Beam systems have been applied, which may either utilise liquid ion metal sources,[38] plasma sources,[125] or as recently demonstrated a Paul Ion trap[37]. The techniques for emitter generation are summarised in Figure 2.11.

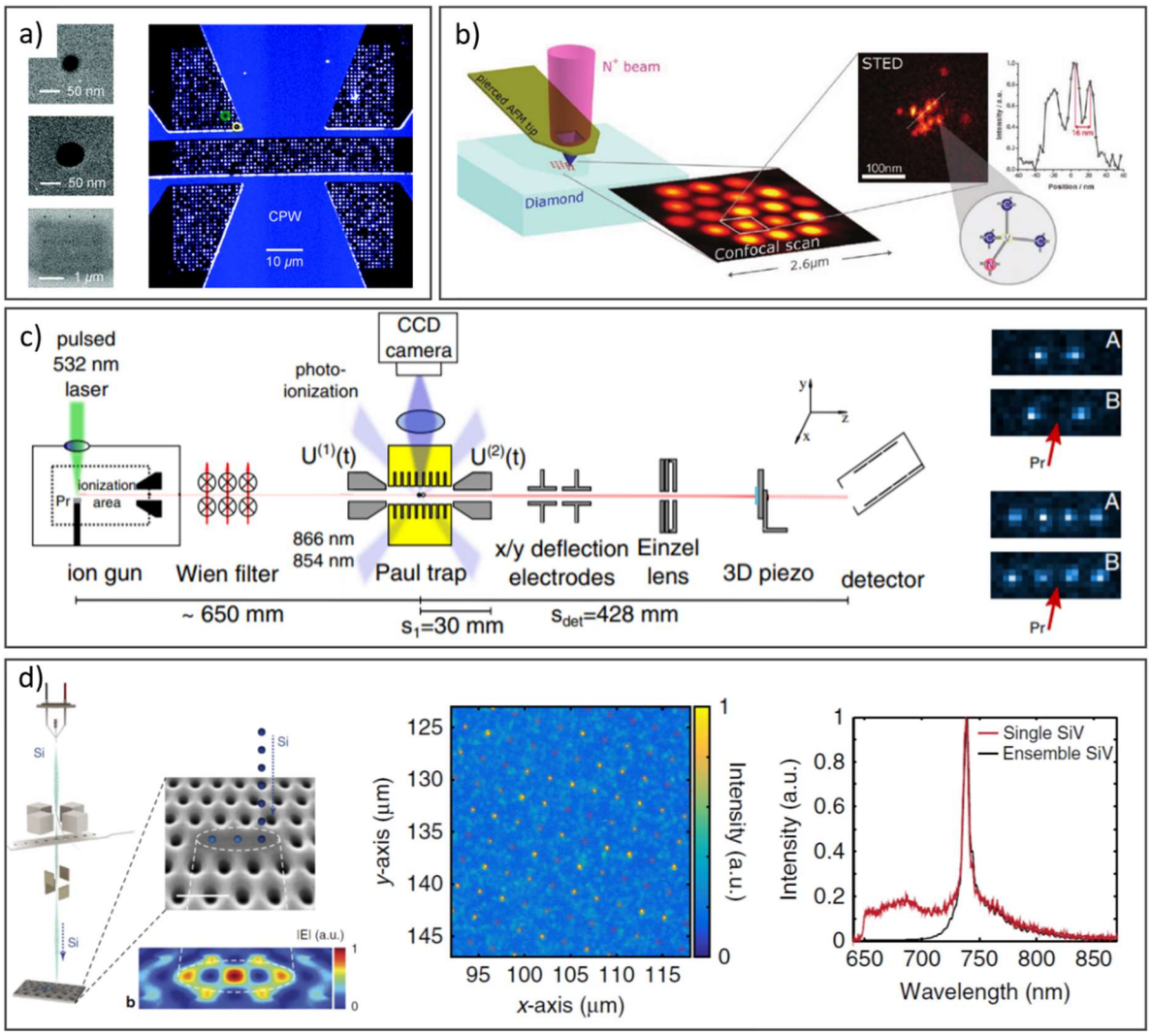

Figure 2.11 Methods for site specific emitter creation based on ion implantation. (a) Implantation of Nitrogen into diamond through apertures, as defined by a mask by Electron Beam Lithography. A map of the implanted sites shows the capability of the technique. (b) Implantation of Nitrogen into diamond through a pierced AFM tip. (c) Direct and mask free ion implantation of rare earth ions by a specialised Focused Ion Beam Setup, utilising a Paul trap as the ion source. (d) Ion implantation of Si into diamond from a Liquid Metal Ion Source FIB system. Reproduced from (a) - [35], (b) - [36], (c) - [37], (d) - [38]

Monolithic concepts have long been seen advantageous, due to a high field overlap that is achievable when the emitter is integrated at the device centre. However, single material platforms may easily be limited in certain properties, such as the potential to fabricate single devices or an entire circuit from that specific material. This was the driving force for hybrid integration for long time, for example utilising nanodiamonds,[126] which offer a suitable degree for spatial placement through nanomanipulation. Furthermore, a single material

platform may not provide all characteristics required for a fully on-chip integrated photonic circuit. Therefore, efforts in this case range from the integration of nanoparticles in cavities and waveguides,[127-132] to integration of 2D materials with photonic structures, [133-135] to an approach where waveguides/ nanoneedles containing single emitters are integrated with another material platform.[136-138] Particularly, the latter approach has become appealing as demonstrated by Noel Wan et al.[139], where a diamond chiplet containing implanted emitters were integrated with an Aluminium Nitride photonic integrated circuit. For a more comprehensive overview on the topic of device integration the reader is referred to recently published reviews by Ali Elsaharri et al.[140], as well as Jae Hyung Kim et al.[141].

Chapter 3
Experimental Methods

3.1 Nanofabrication

For the creation of photonic devices, as described in Chapter 2, nanofabrication techniques are required. The first step in a typical fabrication scheme is the definition of a mask. In most cases this is achieved by means of a lithography method, such as optical lithography or electron beam lithography (EBL). In both cases, a light/ electron sensitive material, such as a polymer resist, is exposed selectively, which causes a chemical modification of the resist changing its solubility. After exposure the resist is developed, which removes regions with higher solubility, i.e. those that were exposed before. Throughout this thesis EBL was done on a Zeiss Supra 55 VP SEM, equipped with a RAITH EBL system. The recipe, including exposure parameters and development, was constantly developed and exact parameters are given in the respective sections of this thesis.

For the subsequent step, after EBL, the underlying material is modified by etching, deposition or through surface functionalisation. In this thesis, material modification was achieved through Reactive Ion Etching (RIE) or Electron Beam Induced Etching (EBIE). For RIE, a reactive ion species is generated in an RF plasma (13.56 MHz) at low vacuum pressure (~ 10 mTorr) and then directed onto a sample through an applied stage bias. The reactive species interacts with the sample by chemical reactions, as well as physically due to the collision of ions with the sample. Through chemical reactions with the reactive ion species a volatile species can form, whereas the removal of the volatile species is accelerated through the physical interaction of ions with the sample.[142] The RIE systems used in this thesis was a Trion ICP plasma system or a lab built RIE system with no ICP capability.

For EBIE, an electron beam instead of ions is used to drive chemical reactions at the nanoscale. In detail, a precursor is supplied to the surface, either through a Gas Injection System (GIS) or by filling the entire SEM chamber with a gas, called Environmental SEM (ESEM) mode. The

incident electron and secondary electrons drive a reaction between the physisorped gas molecules and the substrate, which causes the volatilisation of the material. Thus the material is etched by a reaction driven through the electron beam.[143] Large area EBIE on masked samples, as described in chapters 4, 5, and 8 was done on a Zeiss EVO system with Environmental mode. Focused EBIE was done on a FEI Sirion system.

3.2 Confocal Microscopy

For the characterisation of photonic devices and quantum emitters, a confocal laser microscope was used. In contrast to a standard wide-field microscope, the key feature of the confocal microscope is the addition of a pinhole in the excitation and the collection path. By that, the collection is limited to the excitation spot, which means that both collection and excitation are focused on the same spot, hence the name con-focal microscope. The confocal microscope has a higher spatial resolution and achieves a better signal to background ratio, which is a stringent requirement for the observation of single photon emitter. The principal setup used for all studies is shown in Figure 3.1. It consists of a 532 nm continuous wave laser (Gemstone), with the size of the laser beam first expanded through a telescope arrangement, then guided by mirrors through a neutral density filter (Thorlabs), by which the laser power can be adjusted. Optionally, a lambda half waveplate (Thorlabs) was utilised to adjust the polarization of the laser in order to maximise the excitation efficiency of emitters or cavities. The laser is then reflected by a dichroic mirror (Semrock) and a scanning mirror (Thorlabs), and guided through 2 achromatic doublets to the objective (Nikon 0.9 NA), which focuses the laser beam to a diffraction limited spot on the sample. The optical path between the scanning mirror and the objective corresponds to 4 times the focal length (4f system). As the incoming laser beam is deflected by the scanning mirror, the 4f system ensures that the beam goes collimated into the back aperture of the objective. Specifically, the 4f system translates the spatial displacement of the laser beam into a purely angular change, enabling that the laser beam at all times impinges collimated onto the back aperture of the objective. The photoluminescence (PL) generated by the excitation laser is then collected through the same objective and guided back on the same path, while passing through the dichroic mirror. A longpass filter was then in the optical path used to eliminate laser leakage through the dichroic mirror. The PL was then collected by either of one fibre couplers, selectable by a flip mirror. Both fibres are a Thorlabs multimode fibre with a core size of 50 um. The core of the fibre in this setup acts as the confocal pinhole. One fibre was then guided to a spectrometer (Princeton Instruments with either a 300 l/mm or a

1200 l/ mm grating), the other fibre was split in two arms, each connected to an Avalanche Photo Diode (APD - Excelitas). Through a time correlator (PicoHarp) the counts on both APDs could be time-correlated, thus allowing for time correlation measurements, acting as a Hanbury-Brown and Twiss (HBT) setup. For lifetime measurements a pulsed laser (512 nm, 20 MHz) was used, with the trigger signal delivered to the time correlator. For upconversion and oil immersion experiments as discuss in chapters 7 and 8, respectively, a separate setup was used as detailed in the respective chapters.

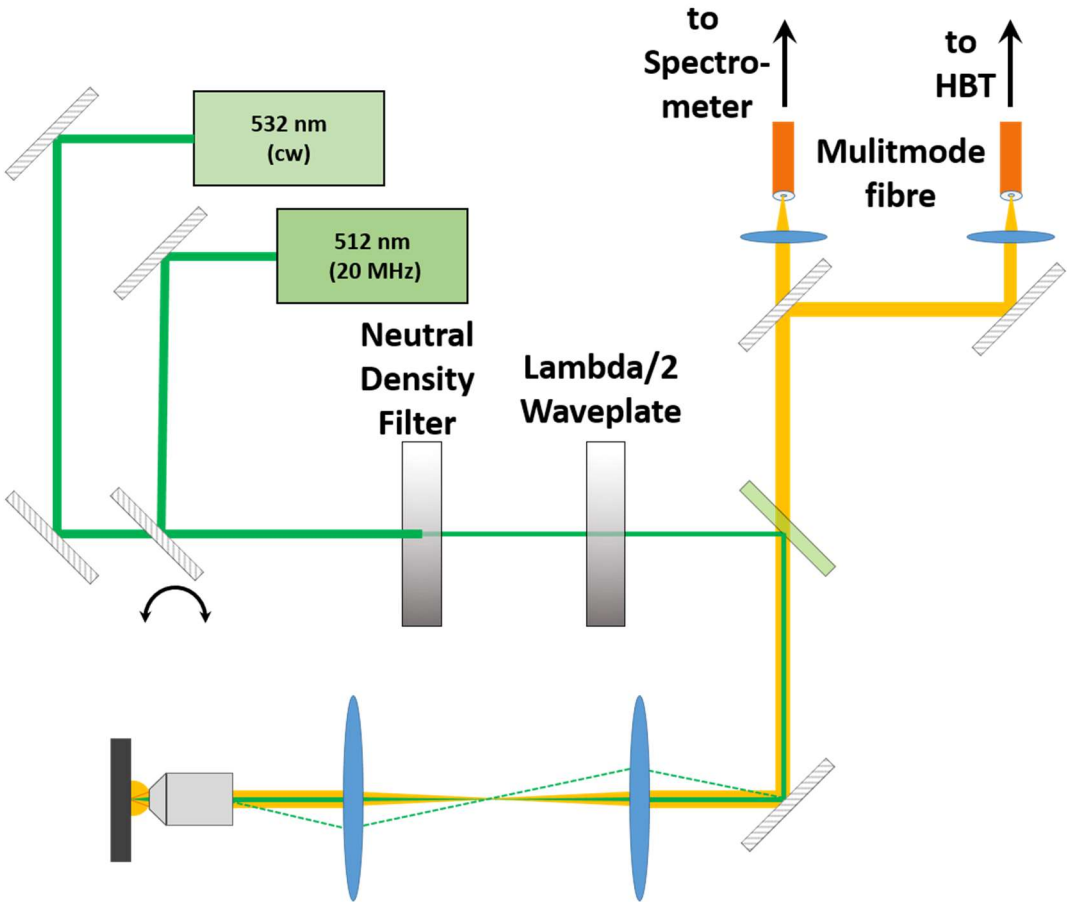

Figure 3.1. The main confocal laser microscope setup used for most optical characterisation during this thesis

Chapter 4

Photonic Crystal Cavities from Hexagonal Boron Nitride

This chapter presents the fabrication of the first photonic crystal cavities from hexagonal Boron Nitride. The main goal for this project was to achieve a way for monolithic integration of quantum emitters. The original idea of the project was conceived by Sejeong Kim, Igor Aharonovich, and Milos Toth. Johannes E. Fröch developed and conducted the fabrication and tuning procedure. Sejeong Kim performed optical measurements and simulations. Joe Christian and Marcus Straw provided cavities fabricated by Focused Ion Beam milling. Kenji Watanabe and Takashi Taniguchi grew the hBN samples. James Bishop assisted with EBIE experiments, Daniel Totonjian prepared trenched silicon substrates. Sejeong Kim, Johannes E. Fröch, Igor Aharonovich and Milos Toth co-write the manuscript.

4.1 Introduction

Controlling and manipulating light at the nanoscale is important for a vast variety of applications that include sensing, quantum information processing, secure communications and cavity QED experiments.[43,83,88,116,124,144-149] Key components for most of these applications include optical resonators such as photonic crystal cavities, and non-classical light sources that can emit single photons on demand such as colour centres in solids,[19] defects in carbon nanotubes (CNTs),[150] single molecules[151] and quantum dots[152]. Remarkable progress has been achieved over recent years to realize on-chip integrated quantum photonic circuits that employ various combinations of these systems. For example, in a monolithic approach where nanophotonic elements and a quantum light source are embedded in the same material, coupled systems have been implemented using diamond,[83,88,89] rare earth crystals,[121-124] and gallium arsenide[153,154]. Alternatively, hybrid systems, where an external source is positioned in close proximity to the photonic element made from a foreign

material, have been assembled from a broad range of materials such as CNTs[155] and InAsP quantum dots (QDs)[137,156] integrated with silicon nitride components.

In recent years, layered van der Waals materials have emerged as promising hosts of ultra-bright quantum emitters.[24] Integration of these light sources with dielectric and metallic waveguides has been achieved by placing flakes of the van der Waals hosts on top of the waveguides.[157-159] However, in such a hybrid approach, the emitter couples only to the evanescent field of the cavity mode. Hence, spatial matching between the emitter and the electric field maximum is limited, and scattering losses are increased. A monolithic system, in which the photonic resonator hosts the quantum emitter is required for ideal on-chip devices. Here, we design and fabricate optical cavities from hBN – a wide bandgap, hyperbolic van der Waals material[160] that has recently attracted considerable attention as a promising host of ultra-bright, room-temperature quantum emitters.[24,25,28,106,161,162] In addition, hBN is naturally hyperbolic and exhibits volume-confined phonon polariton modes[163] that open up opportunities to study light–matter interaction in the deep subwavelength regime and advance infrared and terahertz nanophotonics[163,164]. It is therefore important to engineer nanostructures that enable control over a broad spectral range that accommodates both visible on-chip nanophotonics and integrated polaritonics. The specific designs for the optical cavity used in this work is based on a 2D photonic crystal slab and a 1D ladder type nanobeam structure. Finally, the layered nature of hBN allows flakes to be easily relocated and combined with other platforms. This, together with a high degree of inherent chemical inertness, makes hBN resilient to a broad range of environments such as liquids, and hence applications in sensing where the relatively low refractive index of hBN is beneficial as it leads to large evanescent fields that enhance sensing efficiency.

4.2 Methods

4.2.1 Preparation of suspended hBN

We used trenched silicon substrates in order to maximize the refractive index contrast in *z*-direction (normal to the plane of 2D hBN layers). First, high crystalline hBN flakes were mechanically exfoliated from sticky tape onto trenched silicon substrates. Tape residuals were removed by calcination in air for 2 h at 450 °C on a hot plate. Further desorption of contaminants and an increase of adhesion of flakes to the substrate was achieved by annealing in a tube furnace (Lindberg/Blue M) with Argon at 850 °C for 30 min.

4.2.2 Electron Beam Induced Etching

A 15 nm tungsten film was deposited in a homebuilt plasma sputter deposition chamber using a growth rate of ~0.8 Å/s. On top of the tungsten layer, 950 PMMA A3 was spun on to a thickness of ~100 nm. Cavity designs were patterned via conventional EBL at 20 kV, 40 pA, on a commercial Zeiss Supra 55VP SEM with a RAITH E-beam Lithography System. The cavity patterns were transferred into the tungsten film via RIE (homebuilt) using SF_6 flown at a rate of 60 sccm and a pressure of 10 mTorr (RF power = 100 watt, self-bias = 200 V). Under these conditions the tungsten film was fully etched in the exposed areas within 20 s. The PMMA was removed in an Acetone bath followed by ashing of residual cross-linked PMMA in Oxygen plasma. Further cleaning was done in Acetone and IPA. EBIE of hBN was done at 1 kV, 15 nA in a water atmosphere of 150 mTorr in a Zeiss Evo LS15. Finally, the tungsten mask was removed using H_2O_2 (30%). Although we observe optical modes without further processing steps, the chance of activating/ creating emitters is highly increased after annealing. Therefore, after fabrication the samples were annealed in a tube furnace in Argon, at pressure of 1 Torr, and Argon flow rate of 50 SCCM at 850 °C for 30 min.

4.2.3 Focused Ion Beam Milling

Cavities fabricated by focused ion beam (FIB) were milled using a Ga^+ ion beam at 30 kV, using beam current of 32 nA. Water vapour was delivered to the processing site through a gas injection nozzle in order to suppress charging artefacts during FIB milling. In order to remove damaged areas of hBN and remove implanted Ga ions, the samples were annealed for 2 h in vacuum (1 mTorr) in a tube furnace (Lindberg/ Blue Minimite) at 900 °C.

4.2.4 Finite Difference Time Domain Simulations

FDTD simulations were performed using the Lumerical software package. Our 1D photonic crystal cavities each have 25 uniform-sized air holes, as is shown in Figure 4.1(a). The nanobeam photonic crystal cavity is defined by the beam width w, the lattice constant a, the rectangular size, defined by h_x, h_y, and the beam thickness t. A cavity is formed by modulating lattice constants in the middle of the structure. The region with modulated lattice constant is called a photonic well, while the region with a periodic lattice constant is called a photonic mirror. The lattice constant in the photonic well decreases gradually in order to avoid an abrupt change, as is shown in Figure 4.1(b). A 1D photonic crystal with lattice constant (a) having h_x=130 nm, h_y=550 nm, t=230 nm, w=750 nm has 4 prominent modes in the visible wavelength

range. F0, F1, and F2 are modes from the first dielectric band, while S0 is the mode from the second dielectric band. The frequencies of the fundamental mode and higher order modes are determined by the photonic band used for the cavity design. In our case, the lowest energy photonic band forms a photonic well, the fundamental mode has the highest energy, and is therefore located at the shortest wavelength[165]. We note that the S0 mode is not the air mode because cavities designed to form a photonic well from the air mode are different from those employed here, i.e. lattice constants in the photonic well region should be larger than in the photonic mirror region. We additionally conducted simulations to see how nanobeam thickness and width affect the *Q*-factor. First, we fixed all the parameter to a=250 nm, h_x=130 nm, h_y=550 nm, w=750 nm, and spanned the thickness from 150 nm to 350 nm. Within this range, larger thickness provides higher Q-factor. Next, we fix thickness to 300 nm and vary nanobeam width (w). Q-factor is maximum when the width of the 1D PCC is 760 nm.

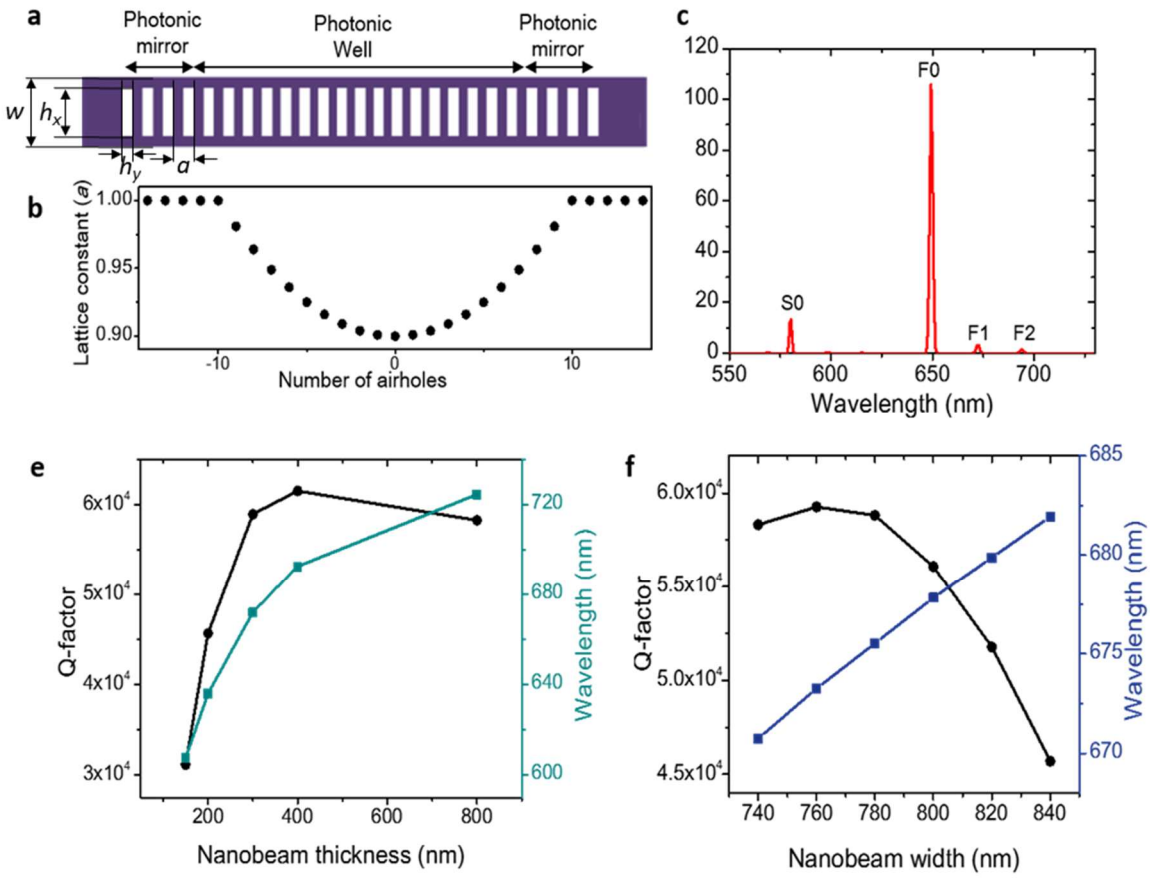

Figure 4.1. 3D FDTD modelling for 1D photonic crystal cavity. (a), Schematic showing 1D ladder-like photonic crystal cavity. (b), Photonic mirror region has lattice constant of 'a', while photonic well region has modulated lattice constant as plotted in the graph. (c), Spectrum

showing the S0, F0, F1, and F2 modes. (d), Q-factor with respect to thickness of nanobeam. (e), Q-factor with respect to nanobeam width (w).

4.3 Results

4.3.1 Fabrication of hBN Photonic Crystals

As a first step toward applications, we demonstrate nanofabrication of two-dimensional (2D) and one-dimensional (1D) photonic crystal cavities (PCCs) with optical *Q*-factors of up to 2100. Such fabrication protocols are needed because, in contrast to mature semiconductors, techniques for making high Q-factor optical devices from van der Waals layered materials that operate in the visible wavelength range are not yet fully developed. For example, it was unknown whether 2D stacked layers are sufficiently robust to endure nanofabrication processes without being destroyed. Also, undercutting techniques that are used to achieve suspended structures and bulk angle etch processes have not been applied successfully to these materials. This is particularly significant because of the small refractive index of hBN of ~ 1.8 (at $\lambda = 600$ nm) makes it hard to achieve a high refractive index contrast that is needed for efficient light confinement in the visible spectral range. In this work, we resolve these challenges by demonstrating the fabrication and iterative editing/tuning of suspended photonic cavities from the van der Waals material hBN using a combination of hBN exfoliation onto a trenched substrate, reactive ion etching (RIE) and single-step, direct-write electron beam induced chemical etching.[143]

As a first step toward the nanofabrication of photonic cavities, we prepared hBN flakes by scotch tape exfoliation from bulk crystals, which were synthesized in a high pressure–high temperature process that yields carbon and oxygen impurity concentrations below 10^{18} cm^{-3}.[166] Examples of exfoliated hBN films on a bulk substrate, as shown in Figure 4.2(a), reveal a sufficient lateral size for fabrication of devices on the micrometre scale, as films appear smooth over several microns with low amounts of grain boundaries, while the different thicknesses of hBN stacks are apparent by their different colours. Due to the low refractive index of hBN, substrates cause severe optical losses. We therefore employed a substrate with pre-patterned trenches so that optical cavities can be fabricated in the suspended regions, as schematically depicted for the case of a 2D photonic crystal in Figure 4.2(b). Figure 4.2(c) is a scanning electron microscope (SEM) image of the suspended hBN showing the layered nature

of hBN. Layers are held together by van der Waals forces and each 2D monolayer consists of alternating boron and nitrogen atoms arranged in a hexagonal pattern.

The thicknesses of hBN flakes vary from a monolayer to a few hundred nanometres and these flakes appear smooth and flat. From exfoliated hBN flakes, only those with a thickness in the range of 200–500 nm were considered for fabrication. The lower limit was chosen to provide a sufficient *Q*-factor, as thinner films will not confine light sufficiently, whereas the upper limit is selected to allow for only a single guided mode in the out-of-plane direction, as generally preferred for photonic cavities.

The first resonators that we show are 2D PCCs fabricated using a nanofabrication procedure that combines RIE with EBIE. Briefly, a tungsten layer that serves as a hard mask is deposited on top of hBN, followed by a thin layer of e-beam resist (polymethyl methacrylate (PMMA)). Using electron beam lithography, the 2D PCC pattern is written in the PMMA film followed by an RIE step in SF_6 gas, which transfers the 2D PCC pattern into the tungsten mask. The underlying hBN is then etched by material-selective EBIE using water vapour as a precursor gas[167], which results in nearly-straight sidewalls. Moreover, EBIE is a chemical process which does not rely on physical removal of atoms through knock-on processes that commonly occur in RIE and FIB techniques and cause substantial damage in the host crystal.[143] As a result, no post processing (via annealing or wet-chemical treatment) is necessary after EBIE in order to observe and subsequently tune cavity modes, as is shown below. The EBIE process does not involve heavy ions (e.g., Ga) hence re-sputtering of ions and re-deposition of the etched material are absent.

Figure 4.2(d) shows a side view, false-Color SEM image of the 2D PCC fabricated in a suspended flake of hBN with nine holes missing in the centre (L9 cavity). A top-view SEM image of the same cavity is shown in Figure 4.2(e). The geometries of the PCCs presented here were designed to have resonances in the visible spectral range,[168] where hBN quantum emitters are typically observed. To achieve the desired resonances, we used a lattice constant (a) in the range of 240–300 nm, with an air hole radius in the photonic mirror region of $0.33a$ and two air holes at the end of the line defects with $0.22a$, shifted outwards by $0.22a$.

The fabricated cavities were analysed optically using a confocal microscope setup at room temperature. A broadband hBN background emission is excited by a 532 nm continuous wave laser, and an objective lens with a numerical aperture of 0.9 is used for excitation and collection. A comparison of room temperature photoluminescence (PL) spectra measured by

excitation of the cavity centre with line defects (red) compared to excitation of an adjacent periodically patterned PCC area (grey) is shown in Figure 4.2(f). Excitation of the cavity yields an optical mode at 586.6 nm, whilst only a broad PL emission is observed when the laser spot is off the cavity. The electric field intensity profile of the measured mode is depicted in the inset, calculated using the 3D finite difference time domain (FDTD) method. By using a Lorentzian fit, a *Q*-factor of 160 is obtained. The observed *Q*-factor is relatively low, yet there are no other studies on 2D PCCs with similar or lower refractive index materials in the visible wavelength range. We note that, in practice, it is very challenging to open a photonic bandgap using a low refractive index material and a 2D cavity geometry.

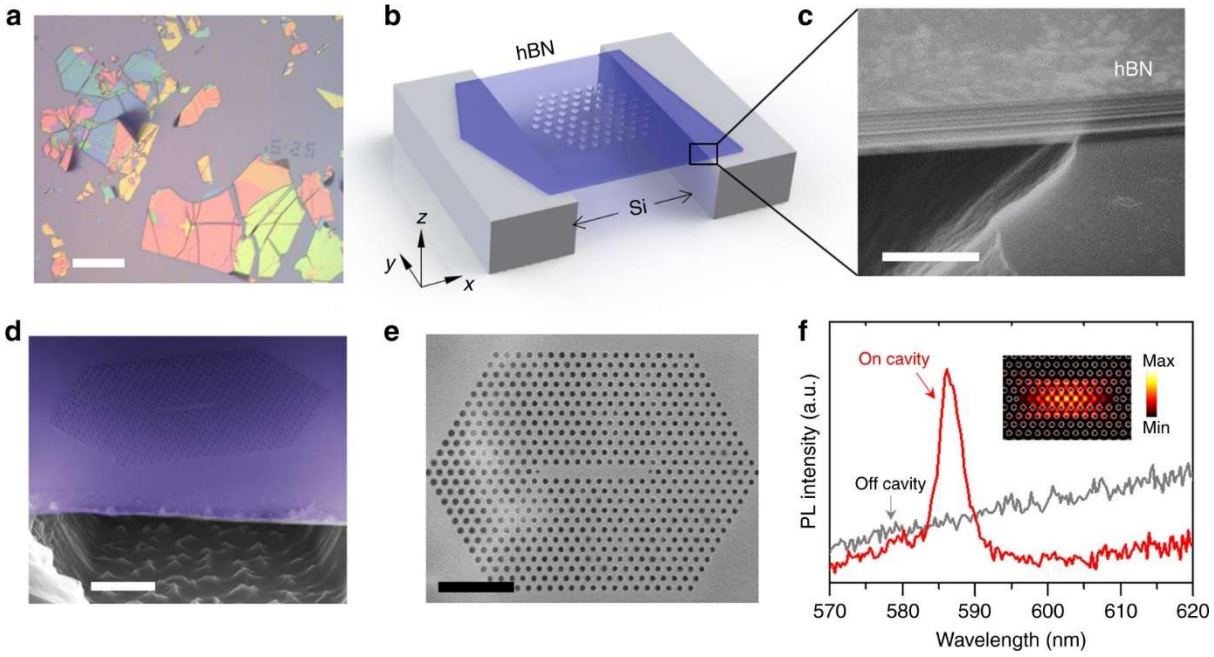

Figure 4.2. Free-standing hexagonal boron nitride 2D photonic crystal cavities.(a) Optical microscope image of exfoliated hBN crystals on a silicon substrate. The scale bar corresponds to 50 µm. (b) Schematic of a free-standing hBN cavity on a trenched silicon substrate. (c) SEM image of the hBN showing the layered structure. The scale bar corresponds to 500 nm. (d) false Color SEM image (45°) of a free-standing hBN photonic crystal cavity fabricated using a combination of RIE and EBIE. The scale bar corresponds to 2 µm. (e) Top view of a 2D photonic crystal cavity. The scale bar corresponds to 2 µm. (f) Photoluminescence spectra with a laser exciting the cavity mode (red) compared with an off-cavity excitation (gray). The inset depicts the electric field intensity profile of the fundamental mode for the cavity calculated using 3D FDTD

4.3.2 1D Photonic Crystal Nanobeam Cavity

To achieve high Q cavities from low refractive index materials, it is more favourable to fabricate 1D ladder-type PCCs. Figure 4.3(a) shows representative SEM images of a 1D ladder PCC (beam width w = 750 nm) fabricated using the same combination of RIE and EBIE that was used to fabricate the cavity in Figure 4.2. The ladder contains 25 uniform-sized, rectangular air holes (h_x = 150 nm, h_y = 550 nm) with a lattice constant a of 250 nm (shown in Figure 4.3(b)). The lattice constants of 19 air holes are modulated to form a photonic well at the centre of the ladder structure with decreased lattice constants in the cavity region compared with the mirror region.

Detailed information on the cavity design and the formation of the depicted modes from the photonic band is given in Section 4.3.4. The designs must accommodate a range of mode wavelengths in order to enable applications such as sensing and integrated photonic devices. This is particularly important in the case of hBN since quantum emitters in this material possess a relatively wide range of emission wavelengths[169], thus necessitating the fabrication of 1D PCCs with modes spanning ~576–762 nm. Figure 4.3(c) shows room temperature PL spectra acquired from three 1D ladder PCCs with lattice constants of 220 nm (black), 250 nm (red), and 280 nm (blue), and resonances that span 600–750 nm, and thus cover most of this range. The three cavities were fabricated in the same hBN flake with a thickness of 280 nm. The 1D ladder cavity design has three confined resonant modes from the lowest energy photonic band as is observed in the PL spectrum obtained from the cavity with a = 220 nm (Figure 4.3(c)). These three modes are in good agreement with a spectrum obtained from FDTD simulation (see Section 4.3.4). The zeroth order mode, also called the fundamental mode, from the first dielectric band (F0) is observed at 612.8 nm, while first order (F1) and second order (F2) modes are observed at 633.9 and 655.5 nm, respectively. Here, “F” designates that the modes originate from the “First” dielectric band, and the numbers 0, 1, and 2 represent the number of nodes along the x-axis. All of these modes are both TE modes and the dielectric modes, for which the electric field maximum is in the higher dielectric region (i.e., within the suspended hBN beams). Cavities with larger lattice constants have optical modes at longer wavelengths. For example, the measured F0 mode is at 678.4 nm for a = 250 and 756.1 nm for a = 280 nm (Figure 4.3(c)). Higher energy modes, in this case the zeroth order mode from the second dielectric band (S0), which are of interest for sensing applications due to their extended evanescent fields,[170] are also observed for cavities with a = 250 and 280 nm. The electric

field profiles of all observed modes, determined by 3D FDTD simulations, are depicted in Figure 4.3(d).

We fabricated and analysed a number of cavities with a range of lattice constants. The *Q*-factor as a function of wavelength for both the first dielectric (F0, red circle) and the second dielectric (S0, black triangle) modes are summarized in Figure 4.3(e), including the cavity modes shown in Figure 4.3(c). Here among F0, F1, and F2, we only included F0 because modes with a lower number of nodes have higher *Q*-factors. The highest *Q*-factor measured from these cavities is 1700. Theoretical *Q* for a 1D photonic crystal cavity obtained using the 3D FDTD method for the measured parameters $a = 250$ nm, $w = 750$ nm, $h_x = 150$ nm and $h_y = 550$ nm corresponds to 9000 with a resonant wavelength of 662.8 nm. The experimental *Q* is lower than the theoretical value mainly due to the roughness of the sidewalls seen in Figure 4.3(a). We also note that higher *Q*-factors are expected from cavities with resonances at longer wavelengths because scattering caused by surface roughness is reduced. It is important to note that this is the first report of such experimental *Q* values in a resonator made entirely from a layered van der Waals material. Here, roughness is considered the main limiting factor of these devices, as with improvement of the etching steps and smoother sidewalls (devices presented in Chapter 5) the Q-factors indeed increased further. In the future, further etch optimization (specifically optimizing the RIE parameters) is required in order to achieve the smoothest sidewalls and therefore obtain the highest possible Q-factors to further develop the functionality of hBN PCCs.

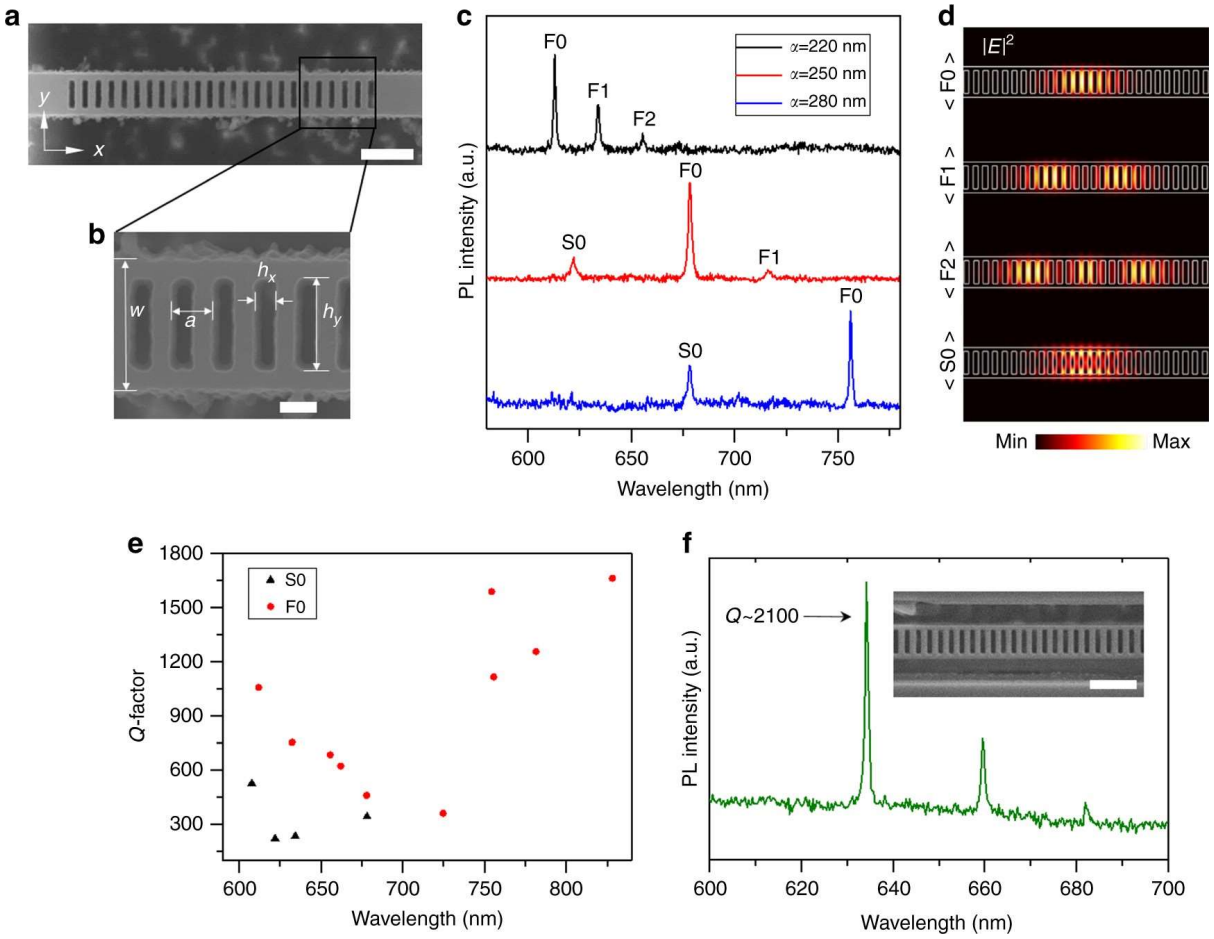

Figure 4.3. Optical analysis of one dimensional (1D) hBN photonic crystal cavities. ***a*** *SEM image of a 1D ladder PCC with 25 rectangular air holes. The scale bar is 1 µm.* ***b*** *magnified view showing the geometrical parameters; width (w), lattice constant (a), air hole width (h_x) and air hole height (h_y). The cavity was fabricated using a combination of RIE and EBIE. The scale bar corresponds to 200 nm.* ***c*** *Photoluminescence spectra of different 1D ladder PCCs in the same hBN crystal with varying lattice constants of 220 nm (black), 250 nm (red), and 280 nm (blue), respectively. F0, F1, and F2 mark the position of the zeroth, first, and second order mode from the first dielectric band. S0 marks the position of the zeroth order from the second dielectric band mode.* ***d*** *3D FDTD simulation result showing field profiles of the measured optical modes.* ***e*** *Experimentally obtained Q-factors of various 1D PCCs fabricated from hBN.* ***f*** *PL spectrum of a 1D cavity fabricated by focused ion beam milling, showing a high Q (~ 2100) mode in the visible spectral range. The inset is an SEM image of the cavity and the scale bar corresponds to 1 µm*

To further investigate potential techniques for the fabrication of cavities from suspended hBN, we employed a focused ion beam. While FIB is an attractive option for direct milling of some

materials, it causes damage within the crystal that must be recovered by annealing. However, the effectiveness of annealing treatments varies substantially for different materials. For example, diamond cavities fabricated using a FIB have very low Q (<800)[171] while yttrium orthosilicate (YSO) crystals show higher Q-factors of several thousand[124]. Figure 4.3(f) shows the PL spectrum of a cavity that was fabricated by FIB milling, and annealed (900°C, Vacuum, 2 h) to recover FIB-induced damage. Additional details on fabrication of cavities by FIB milling is given in the Methods section. Modes are observed at 634.2 nm (F0), 659.6 nm (F1), and 682.0 nm (F2), with a Q-factor as high as 2100 for the F0 mode. We note that no modes were observed immediately after FIB fabrication, and the annealing step is required to remove residual crystal damage. The inset is an SEM image of the cavity. A comparison of cavities fabricated by both methods shows that for EBIE-fabricated cavities sidewalls within the air holes appear more vertical but rougher, while FIB-fabricated cavities show smooth sidewalls that are slanted. In more detail, we compare sidewall slopes and roughness caused by the various etching methods. Figure 4.4(a) and (b) show slanted sidewalls after RIE etching. In the case of other material systems, it has been shown that RIE etching can yield vertical sidewalls once conditions are optimized, including the gas flow rate and gas mixture rate. This has, however, not been achieved to date with hBN. In hBN, cavities fabricated by FIB milling show more vertical sidewalls compared to RIE. But, due to the beam shape and material re-deposition that are typical of FIB, slanted sidewalls and blunt edges were obtained, as shown in Figure 4.4(c). On the other hand, if we use masked EBIE as described above, almost-vertical sidewalls are achieved with a slant of less than 3° for the first 200 nm etching depth and less than 6° beneath, indicated by the two white dashed lines shown in Figure 4.4(d). However, the sidewall roughness is greater than in the case of FIB and thus limits the Q-factors of cavities fabricated to date by EBIE.

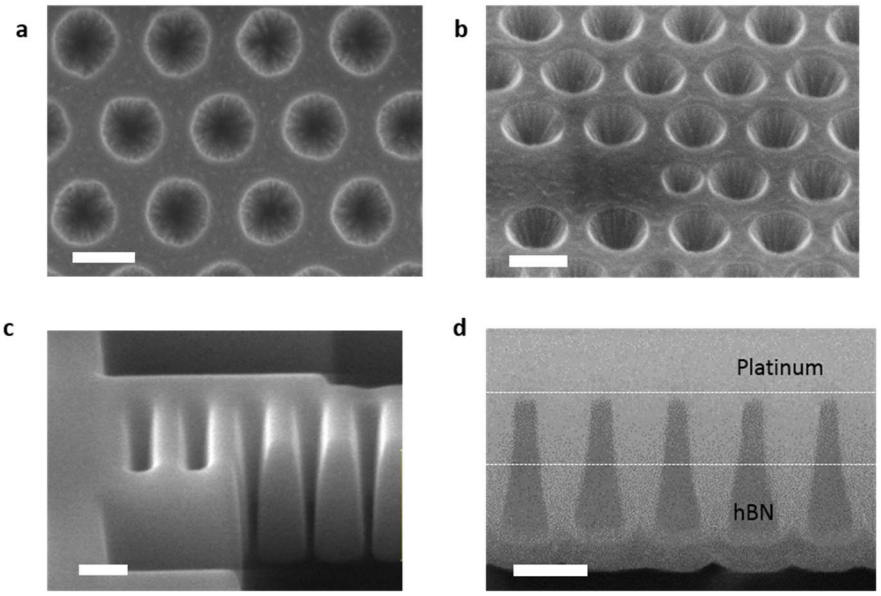

Figure 4.4 Sidewall slopes. (a), Top-view SEM image after RIE. (b), Tilted (45°) view after RIE. (c), Tilted view (52°) of a cross section after FIB etching. (d), Tilted view (60°) of a cross section after EBIE. Scale bars in all images correspond to 200 nm.

Furthermore, Raman analysis to determine the crystalline damage after all processing steps (including annealing of FIB cavities) is shown in Figure 4.5. Spectra of pristine hBN and areas containing photonic crystals pattern by EBIE and FIB are compared. Raman analysis shows that there is no obvious crystalline structure damage after the conducted fabrication steps using EBIE, evidenced by no change in the centre position and FWHM of the characteristic E_{2g} phonon mode at 1366 cm^{-1} (Figure 4.5(a)). Yet, for a cavity fabricated by FIB, even after annealing, crystal damage remains, as can be seen by an increase in the FWHM (Figure 4.5(b))). Hence, at present, the limitations and variations in Q-factor of cavities fabricated by EBIE and FIB are determined by surface roughness and crystal damage, respectively. The fact that EBIE processing does not require annealing is highly favourable for subsequent editing and iterative tuning of the cavities, as is discussed below.

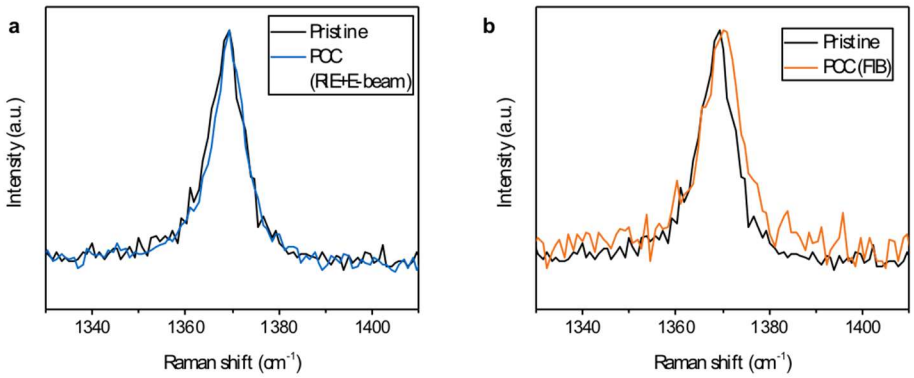

Figure 4.5. Comparison of Raman spectra of pristine hBN (black) with (a), RIE/ EBIE-processed area (blue) and (b), FIB-processed area (orange).

The obtained cavities from hBN are on par, yet lower than other bulk dielectric semiconductors that have much higher refractive indices in the visible wavelength range. Here, we focus on comparison with materials that are known to host quantum emitters in the visible range and have the potential for monolithic integration of emitter – cavity systems. These attributes make them particularly appealing to quantum photonic applications. Cavities fabricated using such materials have been shown to have the following Q-factors: YSO – Q ~3000 at $\lambda = 596$ nm[124], GaN – Q ~5200 at $\lambda = 461$ nm[172], 4H SiC – 6700 at $\lambda = 700$ nm[173] and diamond – Q ~11,000 at $\lambda = 734$ nm[174]. The Q-factors obtained from our hBN cavities are indeed promising for quantum photonic applications. Purcell enhancement of quantum emitters that are located optimally in the cavity field maximum is given by Equation 2.13. For the ladder cavity, with Q ~2100, a Purcell enhancement of ~110 can be achieved.

4.3.3 Tuneable photonic cavity

Next, we demonstrate that the optical modes of the fabricated cavities can be tuned deterministically by EBIE. Tuning is essential to match the resonances to the emission wavelengths of quantum emitters, particularly in the case of hBN where the emission wavelength varies substantially and controlled fabrication of emitters with a given wavelength is yet to be demonstrated. In dielectric cavities, the resonant mode strongly depends on cavity parameters such as the width and thickness. Therefore, numerous methods exist to tune cavity modes, such as thinning via oxidation or RIE, deposition of thin dielectric layers, or gas condensation. In this study, we demonstrate the use of EBIE to controllably tune individual cavities to shorter wavelengths without significant degradation of the Q-factor. As is shown

schematically in Figure 4.6(a), the focused electron beam is guided along the outer sidewalls of a cavity, selectively etching these regions and reducing the width of the beam. In Figure 4.6(b) the PL spectrum of a cavity is shown before tuning (black) with modes F0, F1, and F2 at wavelengths of 745.2, 771.7, and 797.8 nm respectively. A reduced width of the 1D cavity by ~10 nm results in a lower effective refractive index for the optical modes, which resulted in a blue-shift of the cavity resonance by 2.4 nm (red) after the first tuning step. The same process was repeated again to demonstrate further tuning of an additional 4.2 nm (blue). It can be seen (Figure 4.6(c)) that overall the *Q*-factor of the fundamental mode did not degrade significantly (a change of less than 10%) while that of the first-order mode increased in both steps, and the second-order mode showed a mixed behaviour after tuning. We attribute the different trends in Q-factor change to different positions of the field intensity maxima along the beam, and the fact that the EBIE process used for tuning alters the roughness profile of the sidewall (i.e., the roughness of locally smooth regions and those containing asperities can decrease/increase, respectively, during tuning). However, the repeatable tuning by EBIE can be seen as a reliable, robust method for tuning of PCC optical modes over a relatively wide spectral range. It does not cause substantial damage to the cavity and does not require subsequent RIE or deposition steps. The EBIE approach is therefore attractive for two reasons. First, being a localized, direct-write technique, it can be applied to individual cavities without affecting the modes or *Q*-factors of neighbouring structures on the same chip. This is very challenging using deposition or RIE thinning techniques as they require additional masking steps and the low refractive index of hBN necessitates the use of suspended structures to realize high *Q* factors. Second, EBIE does not require any post processing such as annealing that is needed to remove FIB-induced damage, or wet-etching used to etch regions processed by laser oxidation. As a result, the EBIE process can be applied iteratively to individual cavities on a single chip until the desired tuning is achieved.

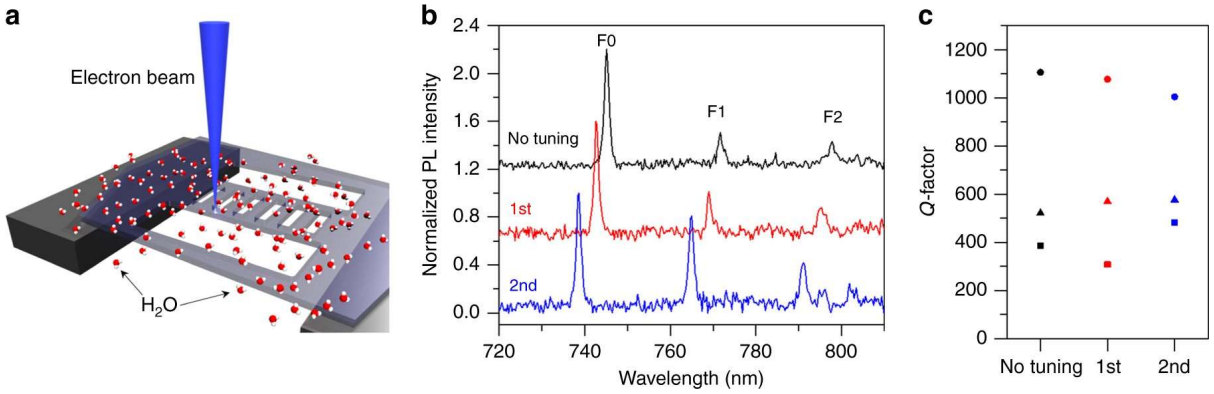

Figure 4.6. Tuning of a 1D nanobeam cavity using direct-write, maskless EBIE. (a) Schematic of the etch process in which a focused electron beam (blue) is scanned along the outer sidewalls of the nanobeam cavity to induce the etch reaction in the presence of water molecules. (b) Photoluminescence (PL) spectra of a 1D photonic cavity before tuning (black), and after the first (red) and second (blue) tuning steps were performed by EBIE. (c) Q-factor of the F0 (circles) and F1 (triangles) modes measured immediately after fabrication (black), and after the first (red), and second (blue) tuning steps

4.3.4 Creation of quantum emitters

Finally, we discuss the potential of integrating quantum emitters hosted by hBN with the fabricated PCCs. Coupling of an emitter to an optical mode requires both spatial and spectral overlap between the emitter and the cavity mode. The spatial overlap probability can be increased by deterministically creating single photon emitters in a non-destructive way with high precision. However, unlike the cases of other materials such as diamond and SiC, ion implantation and electron irradiation have not, to date, been shown to be reliable methods for the generation of quantum emitters in hBN. Furthermore, methods relying on local strain field engineering or laser irradiation are not applicable in this case, as they will cause strong deformation of the suspended cavity and severe damage in the material, resulting in reduction of *Q*-factors. Hence, to create emitters in hBN, we employed an additional annealing step at 850 °C after all the fabrication steps, as this method is known to generate single photon emitters[24] (albeit in random locations). To demonstrate the efficiency of this process, we compare the two regions shown in Figure 4.7(a) – an unprocessed area on the left and a processed area that contains several nanobeams on the right. The corresponding PL map is shown in Figure 4.7(b). In the analysed regions, we found a total of 13 single photon emitters, whose position are marked with yellow circles, all of which are located directly in the fabricated

cavities compared with zero emitters found in the unpatterned area. The creation of extra emitters in the cavity-containing regions can be attributed to an increased surface area, creation of dangling bonds, activation of passivated defects, or chemical modification of sites that undergo partial chemical reactions during etching (we note that stable bright emitters were found consistently on the nanobeams only in samples processed by both RIE and EBIE, but not in samples processed only by RIE or only by FIB, irrespective of whether or not the samples were annealed). Bright spots in the confocal map were analysed spectrally and show clear narrowband zero phonon lines (ZPLs). In several cavities, we clearly observed spatial overlap between cavity modes and emitters, as is shown in Figure 4.7(c). The top plot (red) includes the ZPL at 710 nm from a colour centre and the optical mode of the cavity at 647.7 nm. The emitter is within the laser spot, which has a diameter of ~400 nm. Once the laser is spatially detuned from the emitter (bottom, blue curve), only the cavity mode remains, as expected. To confirm that the peak is indeed a single photon emitter, the emission lines are isolated by spectral filtering and the quantum nature is demonstrated using a Hanbury-Brown and Twiss interferometer. The corresponding $g^2(\tau)$ curve with a zero delay time of $g^2(0)=0.26$ (measured without background subtraction) is shown in Figure 4.7(d), thus classifying it as a single photon source.

We note that to demonstrate coupling between emitter and the optical mode, both spatial and spectral matching are required. However, despite the fact that the probability of spatial matching was increased by the processing steps used to fabricate the cavities (Figure 4.7(b)), spectral matching was not observed because the emitters disappeared after an EBIE tuning step. This most likely happened because of the removal of material from the cavity edges during tuning, where the emitter was physically located, which indicates that the emitter created by the processing steps are located at or closely to the surface. At this stage it has been difficult to find an emitter located in the middle of the dielectric mode of the cavity. To overcome this problem in the future, a method will be required to produce quantum emitters inside the hBN, instead of being located at the surface, which would make it compatible with EBIE tuning. Nevertheless, our method of tuning the cavity resonances, along with recent progress in fabrication of the emitters on demand[29,104,106] is promising for eventual realization of coupled monolithic emitter-cavity systems made from hBN.

For hBN to mature into a reliable platform for integrated nanophotonics, an effort into fabrication of membranes with pre-defined thickness is required, with an emphasis on controlled growth of large-area multilayers. This need is analogous to that which existed in the

field of diamond photonics, which has been reinvigorated dramatically when growth of high quality single crystal material became available. We envision such progress will be achieved with BN as well. In addition to the efforts being made toward deterministic growth of BN, further developments in techniques for both deterministic fabrication of quantum emitters in hBN and resonant wavelength tuning will make weak coupling experiments feasible. To realize coupling between emitters and cavities, tuning into resonance will be required. Gas condensation can be used, in principle, for emitters that are in a close proximity (spectrally) to the cavity mode and overlap spatially with the mode. Alternatively, the hBN cavities can be mounted on stretchable substrates and strain tuning may be employed. This would change cavity dimensions homogeneously in one direction without introducing additional scattering centers. Our present demonstration of hBN PCCs is already highly promising for applications in integrated on-chip quantum nanophotonics, optomechanics, cavity QED and quantum sensing experiments. Moreover, integration of hBN cavities with other 2D materials, may yield hybrid heterostructures for studies of light confinement at the nanoscale, and thus position 2D van der Waals systems as a unique platform in the field of integrated nanophotonics. Finally, the demonstrated ability to deterministically fabricate and tune hBN resonators will further expand its applicability as a hyperbolic material for explorations of light confinement and polaritonics in the mid and near infrared spectral ranges.

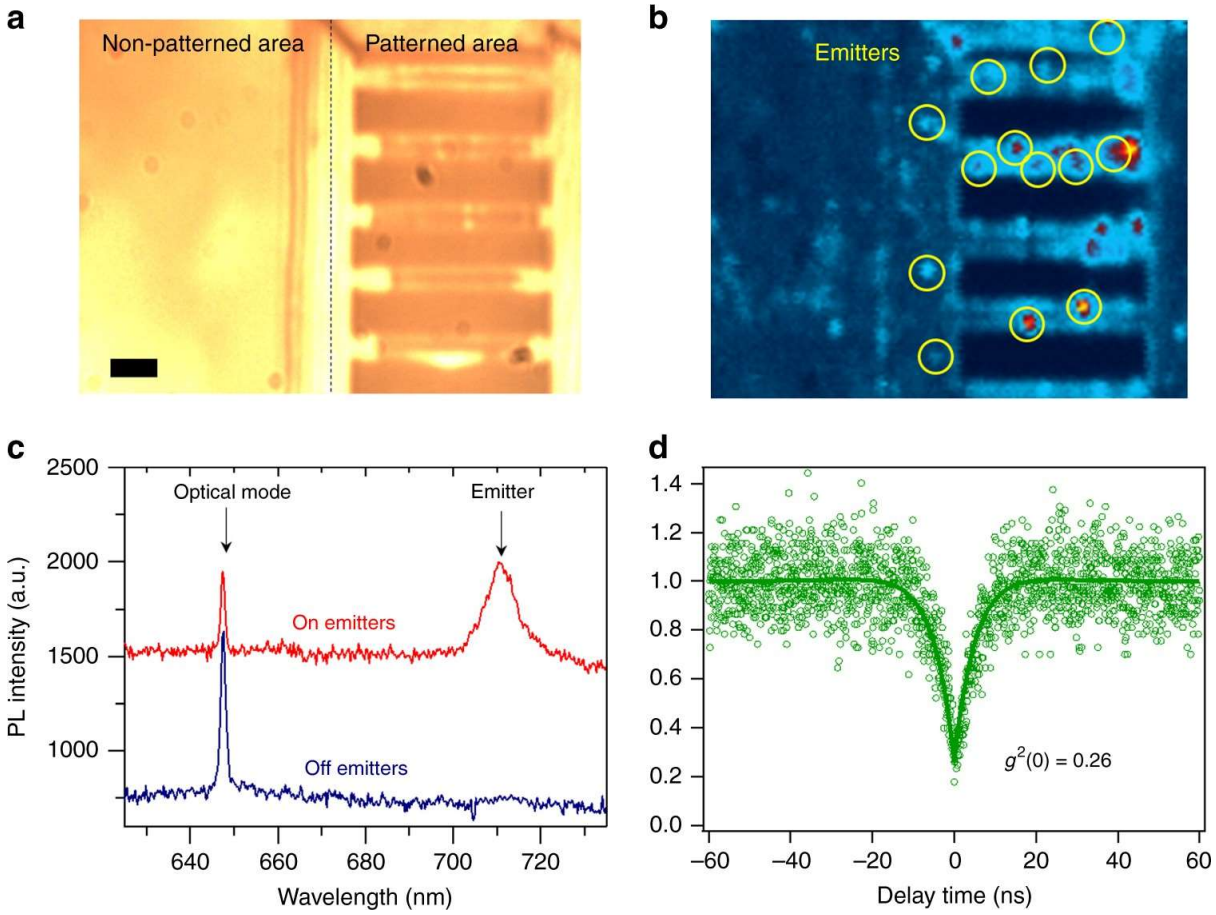

Figure 4.7. Generation of single photon emitters within the hBN cavities. (a) optical microscope image of the analysed area comparing an unprocessed site (left), with a processed site (right) that contains several 1D nanobeam cavities. The scale bar corresponds to 1 µm. (b) corresponding Photoluminescence map of this region. Positions of quantum emitters are indicated by yellow circles (c) PL spectra from two regions of the same cavity showing an optical mode only (blue) and the combination of an optical mode and an emitter (red). (d) Measured $g^2(\tau)$ curve obtained from this emitter

4.4 Conclusion

In summary, we have demonstrated the fabrication of photonic crystal cavities with *Q*-factors in excess of 2000 from hBN, a promising van der Waals crystal. We employed both EBIE etching and FIB milling in protocols used to fabricate 1D and 2D PCCs. We also demonstrated a technique to spectrally tune the optical mode of individual cavities using a maskless EBIE method. Finally, we showed that the cavity-patterned regions host a high density of quantum emitters, marking a first step toward monolithic integration of a hBN emitter–cavity system.

Chapter 5

Photonic Nanostructures from Hexagonal Boron Nitride

This chapter details the fabrication method which was introduced in chapter 4. A particular emphasis is given on the fabrication artefacts can that may occur and how these can be avoided. By further optimisation on the fabrication conditions the device functionality was also increases as compared to devices in chapter 4. The original idea of this project and design of experiments was conceived by Johannes E. Fröch and Sejeong Kim. Yongshop Hwang fabricated hBN microdisks by ICP-RIE. Johannes E. Fröch optimised the fabrication of hBN structures including microrings, photonic crystals, and gratings using the RIE-EBIE approach and conducted the optical characterisation. All authors discussed the results and contributed to writing the paper.

5.1 Introduction

Since the advent of 2D van der Waals (vdW) materials, their peculiar physical properties have been studied intensively, due to their potential applications as atomically thin integrated devices.[175-178] Novel fabrication protocols were developed to reliably process and functionalize these materials, and enable control of their physical, optical, and electronic properties at the nanoscale. In the field of photonics, hexagonal boron nitride (hBN) emerged as a vdW material of interest because it is a naturally hyperbolic material with a highly anisotropic dielectric permittivity which allows directional, subdiffraction-guided modes.[163,164,179] Additionally, hBN has a wide bandgap (≈6 eV)[160] which provides a transparent optical platform in the ultraviolet-to-near-infrared range, and hosts a range of atomic point defects that act as ultrabright, photostable, room temperature single photon emitters (SPEs).[24-26,28,106]

SPEs have numerous potential applications in integrated, on-chip quantum photonic circuits, and quantum information processing.[19,54,152] Integration of SPEs with dielectric cavities

(such as microdisk or microring cavities, photonic crystal cavities) is an important step toward the realization of integrated quantum photonic circuits. Initial results on integration of SPEs from other layered materials such as WSe_2 have been demonstrated by integrating them into 1D silicon nitride cavities or open cavities.[134,180] On the other hand, hBN can be used in an entirely monolithic approach where the devices are fabricated from the parent material that hosts SPEs.[1,181] The monolithic approach is advantageous in that emitters can be located within the high-energy field of the cavities, and can therefore be positioned in the maxima of optical modes, thus enabling the realisation of optimal coupling efficiencies as previously done for diamond, GaAs, and SiC.[82,88,173,182] This in combination with recent reports on the tenability of the SPE emission wavelength will allow to directly tune emitters to the resonant modes of devices,[183] in order to reversibly investigate effects such as Purcell enhancement from hBN SPEs.

In this work, we report detailed nanofabrication protocols used to realize photonic resonators from hBN. In particular, we demonstrate microring cavities and 1D photonic crystals that exhibit high-quality factors (Q) of ≈1500. We also discuss in detail the shortcomings and benefits of a hybrid reactive ion etching–electron beam induced etching (RIE–EBIE) process that is suitable for the fabrication of large-area, suspended, and supported device structures that are made from hBN, and contain nanoscale features and highly vertical sidewalls. The nanofabrication approach presented here is suitable for other layered materials, and therefore broadly relevant to the field of photonics, as well as polaritonic, nanoelectromechanical, optoelectronic, and optomechanic systems,[2] all of which require engineering of structures with nanoscale precision.

5.2 Fabrication Scheme

The fabrication process is outlined schematically in Figure 5.1. First, hBN flakes are transferred onto a silicon or a silicon dioxide substrate via mechanical exfoliation using sticky tape (Figure 5.1(a)). hBN has the advantage that it can be exfoliated from a larger parent crystal, to flakes that are chemically and mechanically stable/robust, with thicknesses as small as a single monolayer. Therefore, it does not require cumbersome preparation steps that are often necessary for classical bulk counterparts such as diamond and SiC. The substrate was prepatterned with trenches that are ≈5 μm deep to allow for a sufficient air gap below the suspended hBN structures. After hBN transfer (Figure 5.1(b)), residues and contaminants from

the sticky tape were removed by calcination in air on a hot plate at 500 °C and subsequent annealing in Argon at 850 °C, which also increases adhesion of hBN flakes to substrates. An optical image of a suspended flake before the subsequent processing steps is shown in Figure 5.1(c). Next, a 15 nm tungsten film was deposited to serve (later on in the process) as a mask for EBIE.[143,167] The substrate was spin coated with a single layer of polymethyl methacrylate (PMMA) A4 (5000 rpm, 50 s) (Figure 5.1(d)), and nanophotonic structures were patterned into the resist using conventional electron beam lithography (EBL) at an electron beam energy of 20 keV and a beam current of 20 pA in a Zeiss Supra 55, equipped with a Raith EBL system. The patterns were then transferred from PMMA into the tungsten layer and hBN by RIE using 10 mTorr of SF_6, a flow rate of 60 sccm, a power of 100 W, a bias of 300 V, and a processing time of ≈30 s (Figure 5.1(e)) in an Oxford Instruments PlasmaPro 80 RIE. After RIE, the PMMA which served as the RIE etch mask, was removed using acetone and the substrate was additionally treated by O_2 RIE ashing (50 W, 150 V Bias, 60 sccm, 10 mTorr) in order to remove PMMA residuals. An optical image of the flake after RIE is shown in Figure 5.1(f), where it can be seen that the patterns were transferred into the W mask and the underlying hBN, although the flake was not penetrated entirely in this etching step. After RIE, we used EBIE (1 keV, 10 nA) in a Zeiss EVO environmental scanning electron microscope (SEM) (Figure 5.1(g)) with water vapour as the reactive agent at a chamber pressure of 100 mTorr to further etch the flakes.[167] The patterned tungsten served as an etch mask in this step. Monte Carlo simulations of electron–solid interactions (performed using the package CASINO[184]) were used to determine that a 15 nm tungsten layer is a sufficient mask for hBN processed with a 1 keV electron beam (Figure 5.2), avoiding penetration of the beam through the mask and undercutting of the mask. Later, we demonstrate that a single RIE processing step is a possible alternative to the hybrid RIE–EBIE method, but the EBIE step is beneficial as it improves sidewall verticality and process resolution. After all processing steps, the remaining tungsten is removed by a H_2O_2 (30%) solution (Figure 5.1(h)). An optical image of final suspended structures (Figure 5.1(i)) shows that they are etched throughout the entire thickness of the hBN flake. We note here that for fabrication of supported devices, as presented later, a thicker PMMA layer (2500 rpm, 50 s) was used, allowing for longer RIE processing times (≈45 s), which would result in etching of the underlying substrate (SiO_2) in less confined areas. This yielded small SiO_2 pedestals that improve the refractive index contrast of the devices. However, we still employed an additional EBIE step, in order to achieve vertical sidewalls and to etch smaller confined featured.

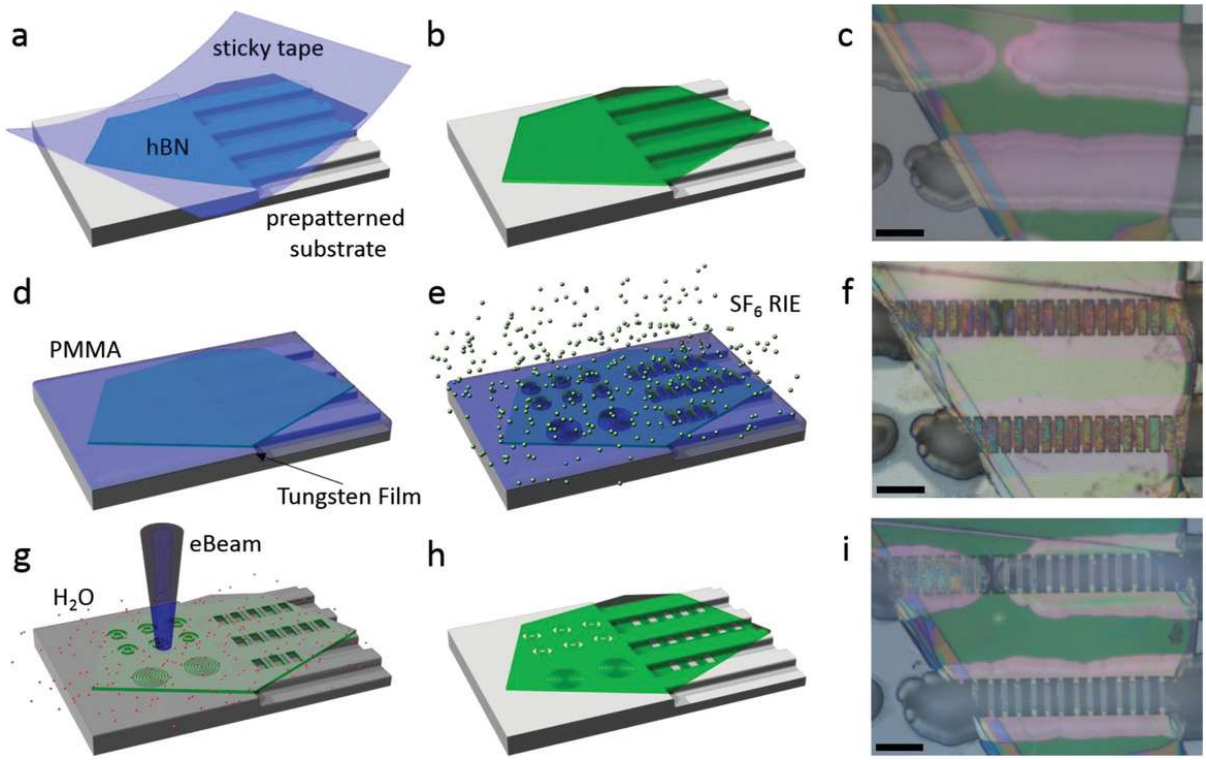

Figure 5.1. Fabrication of photonic structures from hBN. a) Mechanical exfoliation of a hBN flake from sticky tape onto a prepatterned substrate. b) An as-exfoliated hBN flake after a cleaning process. c) Optical image showing such a flake before further fabrication steps. d) Deposition of a tungsten layer and spin coating of a PMMA layer, which serve as masks in the EBIE and RIE steps, respectively. e) EBL followed by SF_6 RIE. f) Optical image of the hBN flake containing 1D photonic crystals after RIE and PMMA removal, showing that patterns are transferred into tungsten and hBN. g) Masked EBIE used to complete the hBN etch. h) Final hBN photonic structures after tungsten removal. i) Optical microscope image of the hBN flake obtained after all processing steps. Scale bars in optical images correspond to 10 μm.

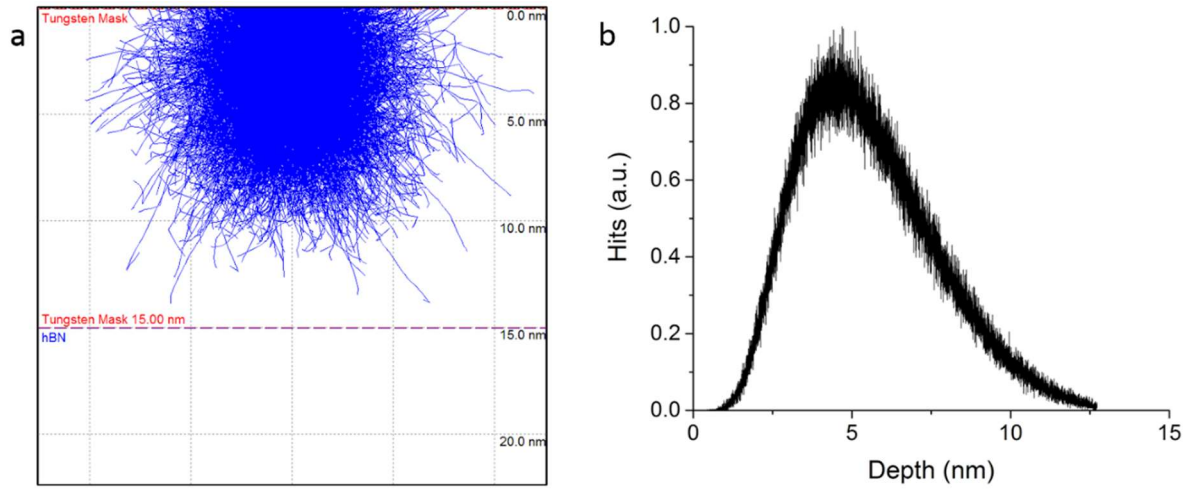

Figure 5.2. Primary Electron penetration depth in a Tungsten Film (15 nm) on hBN (Substrate). (a) Interaction volume of PEs. (b) PE hits vs. depth.

5.3 Fabrication of Prototype Structures

The developed nanofabrication process is directly applicable to arbitrary device geometries, as shown in Figure 5.3. It is possible to fabricate suspended photonic devices, such as photonic crystal cavities (Figure 5.3(a–c)), or devices supported by substrates, such as whispering gallery mode (WGM) microring resonators (Figure 5.3(d),(e)), circular grating structures (Figure 5.3(f)), photonic waveguides (Figure 5.3(g)) with vertical in- and outcoupling gratings (Figure 5.3(h)). Since the developed protocol does not rely on mask lift-off, patterning directly at the EBL resolution is possible without any limitation, enabling feature sizes down to few tens of nanometres. For example, in the case of a photonic crystal cavity (Figure 5.3(a)), air holes with features of 100 nm are fabricated over a length of several micrometre. Sidewalls appear vertical and well resolved, directly demonstrating the high potential of this nanofabrication approach. Another distinct advantage of this technique is that no sonication or rinsing in solution is necessary for mask lift-off, which can relocate smaller free lying features, such as the circular grating and the outcoupling grating of a hBN waveguide shown in Figure 5.3(f–h). Apart from optical considerations, there is no principal limitation on patterning hBN films as thin as a few atomic layers directly on a substrate using our approach. However, to realize suspended hBN structures, thin flakes may be not mechanically strong enough to go through the series of processes used in this approach. In this case where thin, free-standing hBN is required, a previously reported method utilizing maskless direct EBIE can be a viable

alternative as utilized for example in the fabrication of hBN optomechanic devices. The devices in Figure 5.3 constitute the basic components of a quantum photonic chip, and demonstrate that the fabrication technique will make it possible to explore the field of integrated hBN nanophotonics by fabricating structures around existing and precharacterized quantum emitters, since electron beam-induced processing has been shown to be non-invasive to SPEs embedded in hBN.[26] In fact, some emitters in hBN have been observed to be highly resilient to a range of processing treatments, including irradiation by focused He^+ beams.[185] A low-energy electron beam, such as utilized here, will not alter existing defects within hBN through knock-on (i.e., momentum transfer), as the energy threshold for electron knock-on damage is 88 and 130 keV for boron and nitrogen atoms, respectively.[186]

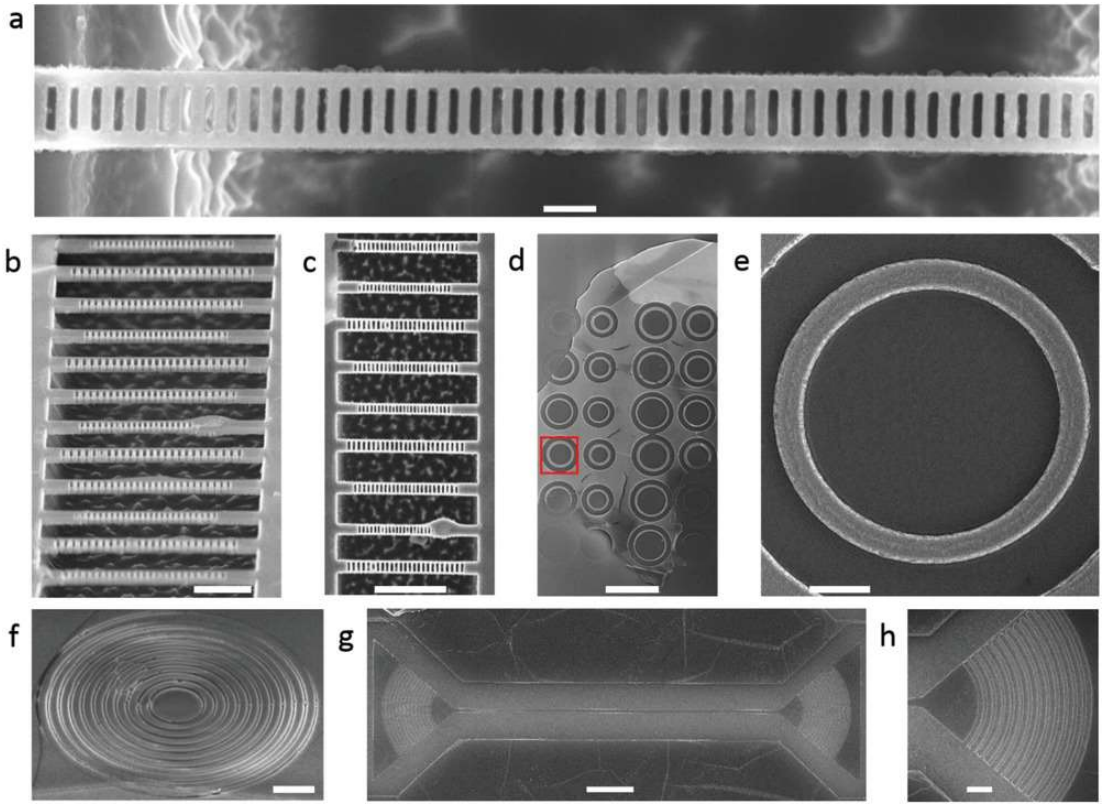

Figure 5.3. Various photonic structures fabricated from hBN. a) Top view of a photonic crystal cavity with air hole sizes of 100 nm × 450 nm over a length of 10 µm. The scale bar corresponds to 500 nm. b) Tilted and c) top view images of free-standing 1D photonic crystal cavity arrays. Scale bars correspond to 2 and 4 µm, respectively. d) A set of hBN microrings with various sizes and e) a magnified view of the highlighted area. Scale bars correspond to 10 and 1 µm, respectively. f) A circular grating structure in a tilted view, the scale bar corresponds to 2 µm. g) A waveguide with two grating couplers and h) its magnified image. Scale bars correspond to 5 and 1 µm, respectively. Structures in (d)–(h) are on a SiO_2 substrate.

5.4 Fabrication Artefacts

The combination of RIE and EBIE, however, suffers from several potential pitfalls that can give rise to fabrication artefacts and compromise device functionality. In Figure 5.4, several of these artefacts are shown. In the case of RIE, it is well known that contaminants in the chamber, an unsuitable mask, or a high physical sputter rate produced by unfavourable RIE conditions can lead to micromasking which gives rise to spots with a size on the order of few tens of nanometres. This in turn will lead to the formation of needle-like features, as the material is being etched. Similarly, we observe micromasking effects during EBIE. To illustrate, the structures in (Figure 5.4(a)) contain spots on the surface of the masked hBN, which are visible after PMMA removal. The spots likely arise from cross-linked PMMA residuals left behind due to incomplete PMMA removal, or regions that were overexposed during EBL, and can act as micromasks and persist in nominally unmasked regions of hBN throughout the EBIE processing step (Figure 5.4(b)) since they are relatively inert to H_2O EBIE. The process of EBIE is known to be highly material selective, and a similar effect has been reported previously.[2,167,187] Specifically, H_2O EBIE of amorphous carbonaceous films was shown to lead to the formation of nanoscale regions that are highly resistant to EBIE, and attributed to electron beam restructuring of the films via processes such as H-C bond cracking, high-order carbon - carbon bond formation, and H desorption.[187] The spots seen in Figure 5.4(b) inhibit EBIE of the underlying hBN, leading to the formation of hBN needles seen in the tilted-view image shown in Figure 5.4(c). To circumvent this issue, the dosage used for EBL must be optimised. Moreover, it is necessary to use low electron beam currents to avoid overexposing of the resist whilst imaging when the flake is positioned for EBL. After SF_6 RIE, it is important to ensure that the substrate is cleaned to remove residual PMMA using both acetone and an additional O_2 RIE ashing step.

Similarly to the previous effect, we observed that the presence of hydrocarbon contaminants in the SEM chamber can lead to the formation of features that are not etched by H_2O EBIE. Most likely, some contaminants react with hBN during electron exposure, forming a compound that is inert to EBIE in a water vapour atmosphere. This is illustrated in Figure 5.4(d) and 5.4(e) for areas processed with total electron doses of 33.6 and 67.2 C cm^{-2}, respectively – such features are typically not removed by EBIE. Smaller features can as well be found at sidewalls of very well fabricated devices, as shown in Figure 5.3(a), indicating that even under well-controlled conditions residual contaminants cause minor artefacts. Attempts to remove these artefacts by

a prolonged EBIE however can cause the unetched features to agglomerate, and to wrap around cavity structures, as is illustrated by Figure 5.4(f),(g), and persist even after extended processing times (≈100 C cm^{-2}). The extended processing times compromise cavities due to irradiation by secondary electrons and backscattered electrons emitted from the underlying substrate. In order to avoid agglomeration and structure wrapping, the SF_6 RIE step has to be maximized until large areas of the hBN film are etched through. In order to suppress etching from secondary and backscattered electrons, the EBIE step has to be stopped immediately, after all features are etched. Despite the above complications, the EBIE processing step has several advantages. Images comparing the same photonic crystal cavity after RIE and after an additional EBIE step are shown in Figure 5.4(h) and (i), respectively. Although larger areas of the hBN film are fully etched by RIE, the sidewalls are not fully vertical and the smallest features are not fully developed in the sense that the film is not completely etched through, as is seen clearly in the enlarged view of the beam end shown in Figure 5.4(j). To date, it was reported that for an SF_6 RIE-based etch process, a maximum sidewall angle of 80° was achieved after optimization, and only for relatively large feature sizes.[188] In contrast, the additional EBIE step utilized here yields straight sidewalls (i.e., sidewall angle of ≈90°) and smaller features are etched thoroughly, as is illustrated by the image shown in Figure 5.4(k). The shortcomings of RIE are attributed to the fact that the plasma needs to penetrate the etched regions of hBN, and material removed by the physical sputtering component of the RIE process can redeposit on surrounding sidewalls. In contrast, the electron beam can easily penetrate nanoscale holes, and the etch process is chemical, thereby mitigating redeposition artefacts under clean conditions. We also note that H_2O EBIE of materials such as single crystal diamond and hBN has previously been shown to be minimally invasive in the sense that Raman spectra of the processed materials do not show evidence of structural damage that is typically produced by ion bombardment/etching.[167,189] Another drawback of EBIE is that backscattered and secondary electrons stemming from the substrate can etch the bottom side of the structure, although at a much slower rate than the sidewalls. This can lead to a certain degree of roughening as seen on the edge of a finished device in Figure 5.4(k). To minimize this issue, it is useful to increase the trench depth, or employ smaller scanning fields focusing on the outlines of the masked devices directly. Under consideration of the mentioned drawbacks, we achieved the best results so far by maximizing the RIE process until larger areas of the material are removed, followed by an EBIE step, which has to be stopped right after the structures are sufficiently etched. This combination and great care to minimize contamination in the

processing chamber led to the smoothest achieved sidewalls and so far the best device functionalities.

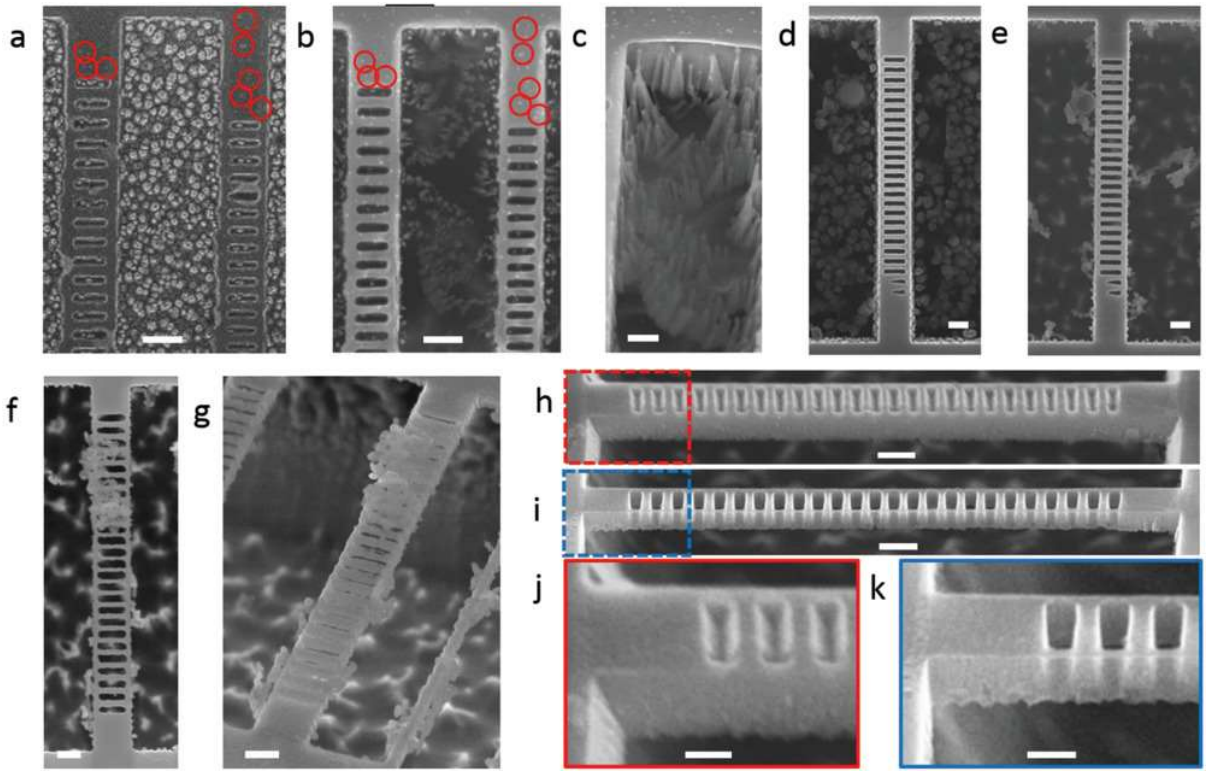

Figure 5.4. Fabrication artefacts of hBN. a) Photonic crystal cavities imaged after RIE, showing small spots from micromasking. Some spots are highlighted with red circles. b) The same spots persist after EBIE, and give rise to the formation of grass in nominally unmasked regions of hBN, seen clearly in the tilted view in c). Scale bars correspond to 500 nm in (a) and (b), and 250 nm in (c), respectively. Two images of the same nanobeam obtained after subsequent EBIE steps, d) and e), show that some areas of unmasked hBN are not etched, producing features that agglomerate and wrap around the cavities. Scale bars correspond to 500 nm. An overetched structure shown in f) top and g) tilted views, in which hBN residuals are not removed even after prolonged EBIE. The integrity of the photonic crystal cavity is compromised by agglomeration of residuals. Scale bars correspond to 500 nm. A comparison of the side view after RIE only h) and after the subsequent EBIE processing step i). Scale bars correspond to 500 nm. j) and k) are enlarged views of the outlined sections in (g) and (h). Scale bars correspond to 250 nm.

5.5 Device Functionality

We now turn to characterization of the devices using photoluminescence (PL) measurements, carried out using a home-built confocal microscope setup at room temperature with a 532 nm excitation source and 300 μW excitation power (measured before the beam passes through the objective). For a suspended nanobeam cavity, a resonance at ≈701 nm, with a $Q = \lambda/d\lambda \approx 1500$ is observed, as shown in Figure 5.5(a) (the right inset is a close-up of the cavity mode). The left inset shows an SEM image of the cavity, with a design discussed elsewhere. For a supported device (i.e., a resonator that rests on a substrate), we demonstrate WGMs of a microring resonator atop an SiO_2 substrate. Figure 5.5(b) shows the WGMs (periodic peaks in the spectrum) from the hBN microring (left inset). The right inset shows a higher resolution spectrum of one of the WGMs, with a measured $Q \approx 500$ at a wavelength of 644 nm. Although the Q of this device is rather moderate, it can be improved in the future by using a substrate with a lower refractive index, such as CaF_2 or MgF_2.

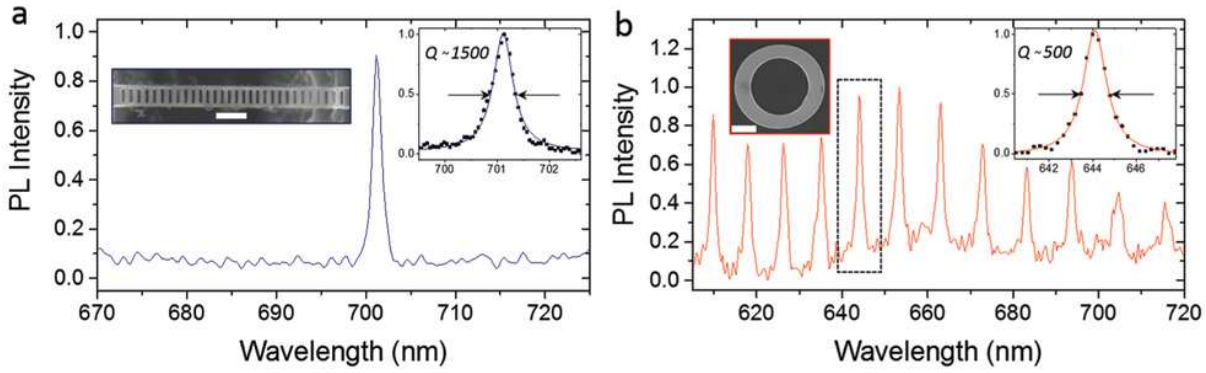

Figure 5.5. Quality factors of the fabricated hBN devices. a) A 1D photonic crystal cavity (PCC) with a resonant mode at ≈701 nm. The left inset shows the measured device, with a scale bar of 1 μm. The right inset shows the cavity Q of ≈1500, as determined from a Lorentzian fit at the resonant wavelength. b) WGMs of a hBN microring. The left inset shows the measured device. The scale bars correspond to 1 μm. The right inset shows the Q of the microring resonator was determined to be 500 by a Lorentzian fit of a resonance at 644 nm.

5.6 Conclusion

We detailed step-by-step fabrication of suspended and supported photonic devices from hBN. For the developed nanofabrication approach, we utilize a combination of RIE and EBIE. We emphasize the versatility of this process by demonstrating several fundamental photonic

devices including microring cavities and photonic crystals, which will enable coupling of hBN SPEs to cavity modes to explore the field of integrated hBN quantum photonics. For a better understanding of the fabrication process, we demonstrate the cause of several fabrication errors, which we observed during the development of this technique and could mainly relate to contamination arising either from the RIE or EBIE step. The best structures achieved so far were realized by maximizing the RIE step, and by using EBIE as a final processing step that improves resolution and sidewall verticality. The presented fabrication approach is not limited to hBN and can be extended to other layered materials. It is therefore of general relevance to the fields of photonics, optoelectronics, optomechanics, and nanoelectromechnical systems.

Chapter 6
Coupling Hexagonal Boron Nitride Emitters to Photonic Crystal Cavities

Due to the semi-random ZPL distribution of hBN single photon emitters in monolithic devices, we did not succeed to find emitters within the tuning range of a photonic resonance. Therefore we change the integration strategy and utilised CVD grown hBN, which was integrated with SiN photonic crystal cavities. The advantage of the CVD grown hBN is that the emitter ZPL distribution is much narrower, which enables a more deterministic approach to the fabrication. The original idea of this project and design of experiments was conceived by Johannes Fröch, Sejeong Kim, Milos Toth, and Igor Aharonovich. Johannes Fröch designed the experiment, fabricated and characterised all devices. Sejeong Kim performed FDTD simulations. Noah Mendelson grew hBN by CVD and transferred onto SiN before fabrication. All authors discussed the results and contributed to writing the paper.

6.1 Introduction

Quantum information processing applications require integration of nonclassical photon sources with optical cavities and resonators to achieve efficient interfaces between flying qubits and quantum memories as well as for quantum repeater applications.[19,41,54,190-192] Several solid-state systems have been explored to achieve this goal, including III–V quantum dots, Color centers in diamond, and single molecules.[124,137,148,193-198] Often, there is a trade-off between the optical properties of the selected source in terms of brightness, stability, or tenability and the selection of the cavity material in terms of ease of fabrication and the ability to achieve strong light confinement. The ultimate goal is to engineer a system in which a bright solid-state emitter can be coupled to a scalable on-chip optical cavity and a waveguide, to realize enhanced emission via modification of the density of states at the proximity of the emitters.[38,112,119,136,138,199] Such a system will then become a key

building block for cavity quantum electrodynamics experiments and integrated quantum photonic circuitry.

Particularly promising sources are quantum emitters in few-layer hexagonal boron nitride (hBN).[24,56,162,169,200-204] Due to both high quantum efficiencies and a high Debye–Waller factor, they are among the brightest solid-state emitters studied so far.[105,205,206] A step forward in the realization of practical devices with quantum emitters in hBN is to couple them to photonic crystal cavities (PCCs), which alter the local photonic density of states leading to a decreased line width and an increase in their emission rates. However, to date, integrating hBN quantum emitters with on-chip photonic cavities has been a challenging task,[1,207] mostly due to a broad and random distribution of their emission wavelengths in the visible range, which has made coupling of the emitters to PCCs inherently impractical.

Here, we report the on-chip integration of hBN quantum emitters with one-dimensional photonic crystal nanobeam cavities fabricated from silicon nitride (Si_3N_4). Specifically, we take advantage of a recently established chemical vapour deposition (CVD) method to grow thin hBN layers with a unimodal distribution of quantum emission at (580 ± 10) nm and spatial densities as high as 2 per μm^2.[30,208] Beyond the narrow wavelength distribution, the advantage of these hBN layers is their uniform nanoscale thickness and large size, which makes it easier to transfer them onto photonic devices. Silicon nitride is consequently chosen as the cavity material because the refractive index contrast between Si_3N_4 ($n = 2.0$) and hBN ($n = 2.1$) is negligible. Moreover, the established fabrication protocols of Si_3N_4 enable us to benefit from high Q-factor (Q) photonic cavities reaching up to 3300. We were able to achieve coupling of several quantum emitters to PCCs with photoluminescence (PL) enhancement up to 6 times. Our results outline a promising route toward scalable on-chip hybrid photonic networks that harness the properties of quantum emitters in hBN as quantum light sources and Si_3N_4 as a technologically mature material platform.

6.2 Methods

6.2.1 Device Fabrication

Si_3N_4 substrates were prepared by purchasing wafers of 300 nm thick LPCVD Si_3N_4 (MTI Corporation), which were then slowly etched using boiling H_3PO_4 (85 wt. % ~ 180 °C) until the desired thickness was achieved, determined by the visual contrast change. For wet transfer,

the hBN/copper samples were spin-coated with ~200 nm PMMA A3 (Microchem.) and baked at 90 °C for 3 min. The supporting copper was then etched in a 0.5 M $(NH_4)_2S_2O_8$ solution until the PMMA/hBN film delaminated. The floating film was picked up with a clean Si substrate, and the film was transferred to Ultrapure Water (UPW) three times to remove residual contaminants. The target Si_3N_4 substrate was then used to pick up the cleansed floating film and placed on a hot plate at 100 °C for 10 min to remove residual liquids. The PMMA was then stripped in a warm acetone bath overnight and briefly (5 min) placed in a UV ozone cleaner to remove residual contaminants. In the following step, the sample was annealed in a tube furnace (Lindberg Blue Mini-mite) at 850 °C for 30 min under continuous argon flow at a pressure of 1 Torr, to increase the adhesion to the substrate and further eliminate contamination. The resist for EBL was AR-P 6200.11 (AllResist GmBH), which was spin-coated at 3500 rpm for 1 min to give an approximate thickness of ~500 nm. EBL was conducted in a FEG-SEM (Zeiss Supra 55 VP) equipped with a RAITH EBL system. The parameters used for patterning were 20 pA at 30 kV and a base dose of ~100 μC cm^{-2}. The patterns were developed in AR 600-546 (AllResist GmBH) for ~45 s at a temperature of ~5 °C. After development, the sample was placed in a UV ozone cleaner for ~30 s to descum the developed regions. Pattern transfer was then conducted in a self-biased reactive ion etching system using an ~300 V self-bias and a forward power of ~90 W in SF_6 plasma at a flow rate of 60 SCCM and pressure of ~10 mTorr. After etching, the resist was stripped in a warm acetone bath overnight, while the remaining resist was further removed by calcination on a hot plate in air at 400 °C (~2 h) and a UV ozone treatment (~10 min). Cavity structures were then released by etching the underlying silicon in a warm KOH (20 wt. %) solution for ~20 min. Following the KOH etch the substrate was put in three consecutive lukewarm UPW baths to remove KOH residues (15 min each). After the UPW baths, the substrate was put into IPA for the structures to be immersed in a liquid with lower surface tension, minimizing the stress during the final drying under a gentle blowing of N_2. After all wet processing steps, the substrate is once more cleaned in a UV ozone step for ~10 min.

6.2.2 Simulations

All numerical modelling including calculation of *Q*-factors, mode volumes, and field intensity maps was performed by using the finite-difference time-domain (FDTD) method. The computational domain was defined as a cuboid volume of 12x3x3 μm^3 with a minimum mesh size of 5 nm. The refractive index used for silicon nitride is 2.0.

6.3 Results and Discussion

6.3.1 Hybrid Integration

Here, it is important to emphasize the nontrivial methodology we employed to create the hybrid quantum photonic devices. Traditionally, in the hybrid photonic approach,[126] the photonic components are fabricated first, and the target material which requires enhanced light interaction is then transferred either using a pick-and-place method (e.g., for nanodiamonds),[209] or using a wet transfer method (e.g., for 2D materials).[134,135,147,210,211] Such a sequence often results in breaking of resonators[134] or degrading of their functionality due to contamination or imperfect spatial alignment. In our approach, we reverse the sequence and transfer the hBN onto the Si_3N_4 before fabricating the final devices, thus eliminating the aforementioned technical difficulties.

A step-by-step scheme of the device fabrication is depicted in Figure 6.1(a), while specific conditions, such as the used equipment, are detailed in the Methods section (6.3.1). First, (I) a few-layer hBN film was grown on copper utilizing a chemical vapour deposition (CVD) method, yielding quantum emitters with a unimodal distribution of the zero phonon line (ZPL) cantered at 580 nm and a spatial density of ~2 μm^{-2}.[30,208] To ensure the quality of the hBN film before further processing, (II) a precheck was performed to confirm the presence of quantum emitters in the as-grown material. Then, (III) the hBN film was transferred from copper to the Si_3N_4 substrate (180 nm on Si) using a wet transfer technique, followed by an annealing step (1 Torr Ar, 850 °C, 30 min). An annealing step at this stage was required in order to avoid delamination of the transferred film in the later steps, as compared in Figure 6.2. Subsequently, (IV) a polymer resist film (CSAR 62) was spin-coated to a thickness of approximately 500 nm, and (V) the photonic cavity design was patterned using electron beam lithography (EBL) and developed. In the current work, we chose to work with 1D PCCs as they provide small mode volumes combined with high-Q resonances. Finally, (VI) the resist was then directly employed as a hard mask to transfer the pattern into the underlying hBN/Si_3N_4 film by reactive ion etching (RIE) in SF_6. After RIE, the resist was stripped in warm acetone, and the device structures were released from the underlying silicon using a KOH wet etch. These fabrication steps are in principle CMOS compatible and, with recent reports of direct growth of hBN on Si_3N_4,[212] may lead to a transfer-free device fabrication process in the future. An optical microscope image of the fabricated sample is shown in Figure 6.1(b).

The hBN film is directly discernible from the substrate by optical contrast with the boundaries outlined by white dashed lines as a guide to the eye, still adhering well to the Si_3N_4 substrate without folding of the film over the device area. A representative SEM image of such an array is shown in Figure 6.1(c).

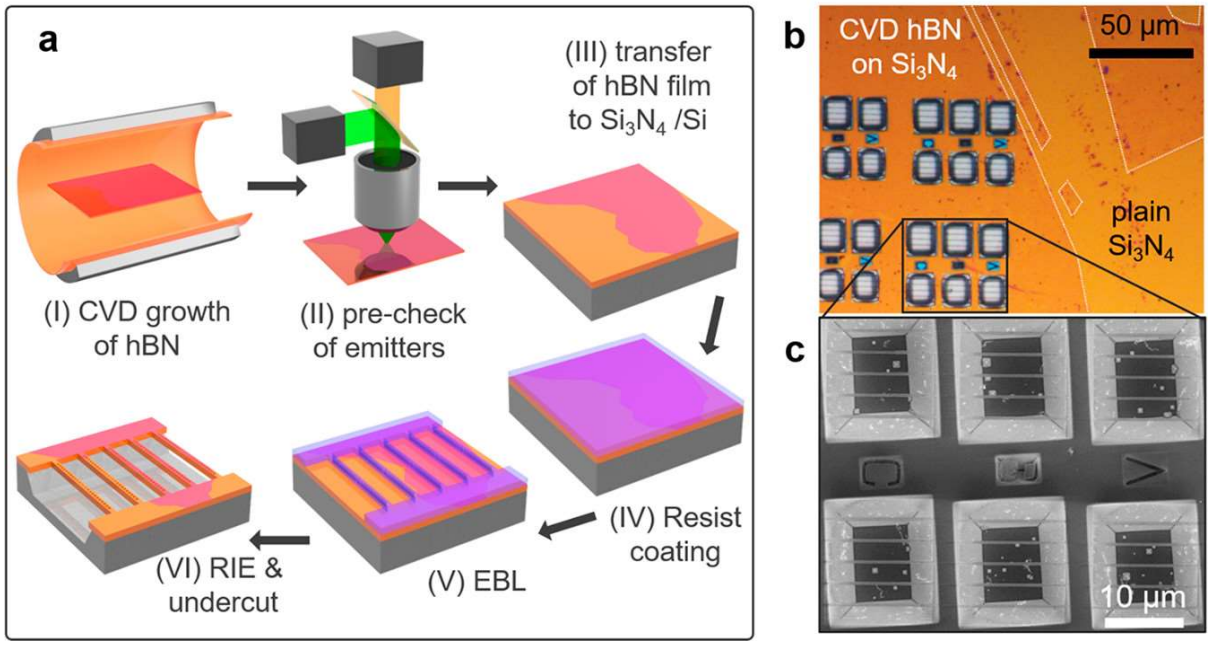

Figure 6.1. Integration of CVD-grown hBN with 1D photonic crystal cavities. (a) Schematic of the fabrication steps: (I) CVD growth of hBN on copper. (II) Precheck of the hBN film on copper using a confocal microscope setup. (III) Transfer the hBN from copper to a 180 nm thick Si_3N_4 substrate. (IV) Spin coating of the EBL resist (CSAR 62). (V) EBL patterning of the cavity structures. (VI) RIE and undercutting to create free-standing hBN/Si_3N_4 devices. (b) Optical microscope image with the final sample. hBN-covered area (white-dashed guideline) is directly visible due to optical contrast. (c) SEM image showing the final free-standing, hybrid photonic cavity arrays.

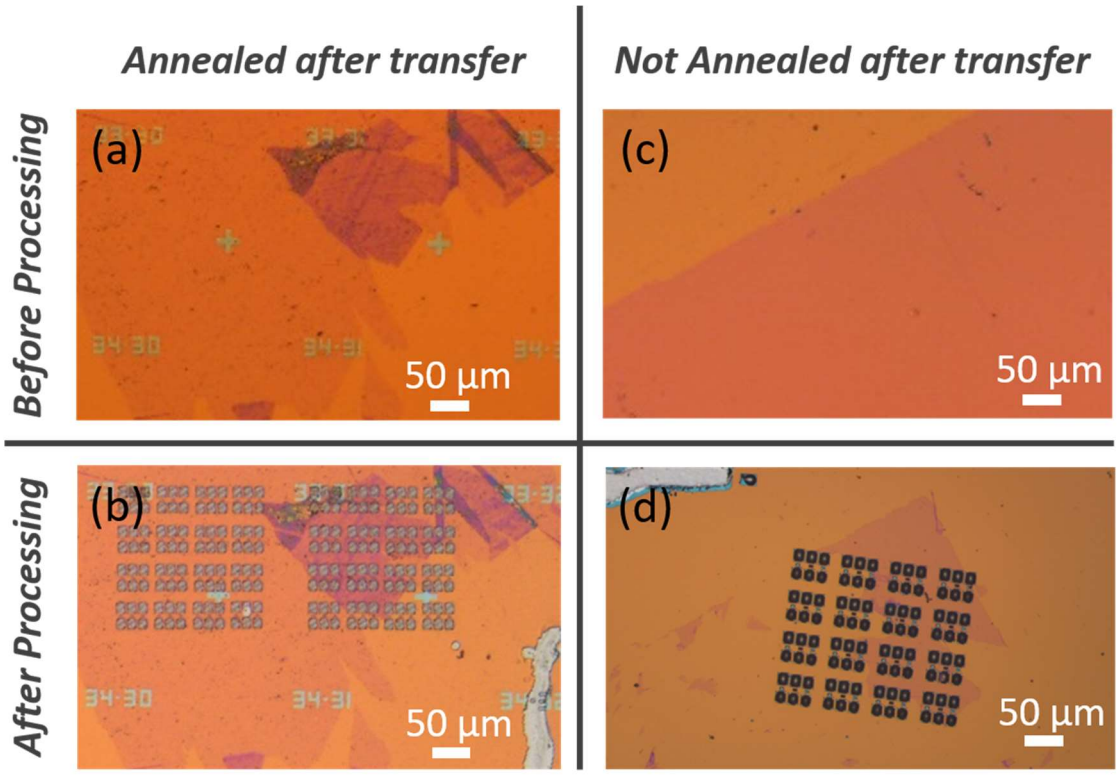

Figure 6.2. Comparison of hBN films annealed and not annealed after transfer. (a) and (b) show the same position of a sample with a hBN film transferred and annealed, before and after all processing steps, respectively. (c) and (d) show the same position of a sample with a hBN film transferred and not annealed, before and after all processing step.

6.3.2 Device Characterisation

An image of a final device comprised of an hBN film integrated with a 1D PCC is shown in Figure 6.3(a). Note that no 2D material is draping over the device as the hBN film is integrated within this architecture. The employed design is a 1D photonic crystal nanobeam with width (w) of 300 nm, thickness (h) of 180 nm, periodicity (a) of 230 nm, and air hole radius (r) of 80 nm.[213] A photonic cavity is introduced by linearly tapering 10 air holes both in radius and in periodicity, for which the centre of the cavity has a periodicity of 0.85a and air hole radius of 0.75r, respectively. The photonic device is analysed based on the finite-difference time-domain (FDTD) method using a commercial photonic simulation tool (Lumerical Inc.). We assume a 5 nm thick hBN layer (n_{hBN} = 2.1) on top of 180 nm Si_3N_4 (n_{SiN} = 2.0). The electric field intensity profiles in the x–y plane and x–z plane are depicted in Figure 6.3(b) and (c), respectively. Here the intensity profile in Figure 6.3(b) is extracted from the centre of the hBN

film. The theoretical Q-factor and mode volume V_m ($V_m = \int \varepsilon E^2 \, dV / \max(\varepsilon E^2)$) at a resonant wavelength of 590 nm correspond to 16 000 and ~1.5 $(n/\lambda)^3$, respectively.

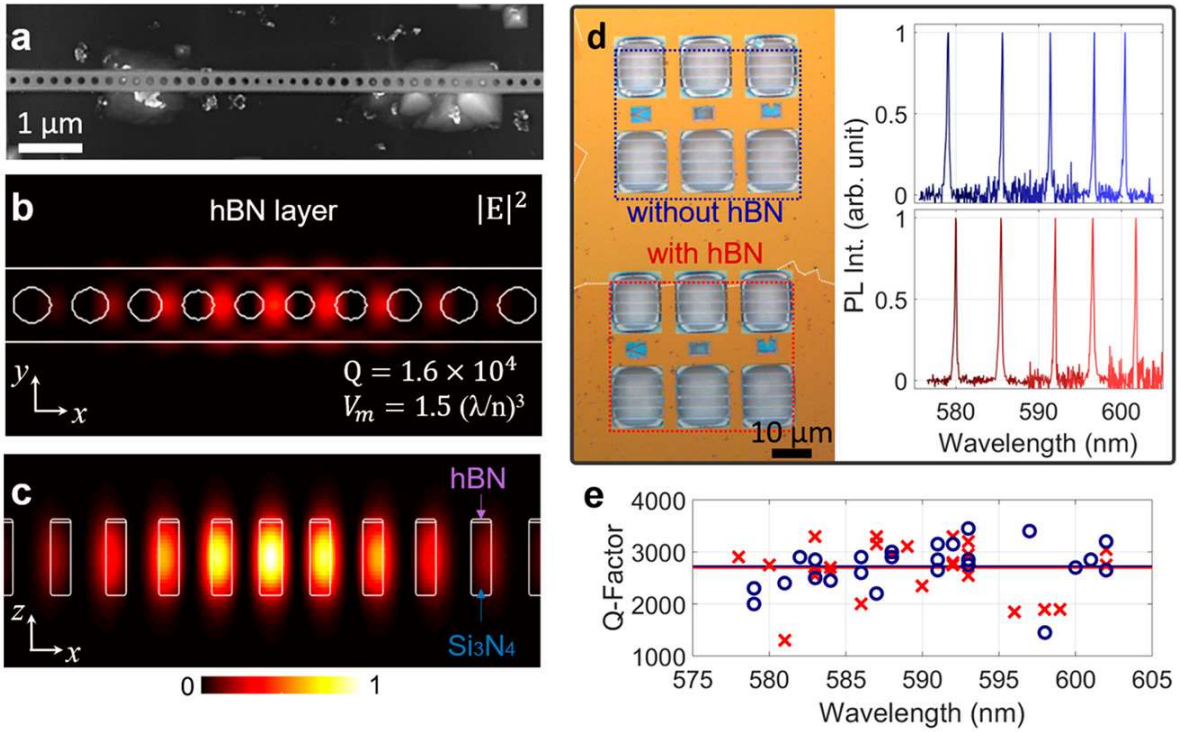

Figure 6.3. Photonic cavity design and properties. (a) Magnified view of a fabricated 1D nanobeam photonic crystal cavity with circular holes. Toward the middle of the cavity, the hole periodicity and diameter are linearly tapered. (b) Top view FDTD simulation of the hBN layer showing the main resonance at 590 nm in the centre of the device with a theoretical Q-factor of 1.6 × 10⁴ and a mode volume of 1.5 (n/λ)³. (c) Side view showing the distribution of the mode and the overlap with the top hBN layer, for which the field overlap is approximately 40% for a 5 nm thick hBN film. (d) Optical image of an area of fabricated devices at the boundary of a transferred hBN film. A direct comparison of the device functionality was taken from cavities fabricated under the same conditions without hBN and cavities with hBN on top showing representative resonances at a target wavelength spanning from 580 to 605 nm shown to their right, respectively. (e) Comparison of the Q-factor from the cavities in the shown area reveals on average values of 2730 ± 430 and 2700 ± 530 for cavities without (crosses) and with (circles) hBN, respectively.

In addition to the advantage of the CVD-grown hBN that alleviates issues of spectral matching, we also achieve a considerably high maximum field overlap at the emitter location, approaching ~40%, as shown in the view through the hBN layer in Figure 6.3(b). The field

overlap is defined as the point intensity measured at the emitter's location divided by the point intensity measured at the cavity mode maximum ($\varepsilon|E(rE)|^2/\max(\varepsilon|E|^2)$). Because of the direct integration method, the optical mode overlaps well with the hBN film. In many of the earlier hybrid approaches,[126] a nanoparticle that is often >30 nm thick is positioned on top of a cavity. In our case, a slightly thinner Si_3N_4 is employed that is then complemented by a smooth 5 nm hBN film that can be considered as a continuation of the original Si_3N_4 cavity, thus resulting in a good mode overlap.

To directly demonstrate the influence of the hBN film on device functionality we compared adjacent regions composed of bare (blue outline) and hBN-covered (red outline) cavities as shown in Figure 6.3(d), respectively. Device characterization was done in a lab-built confocal microscope setup with a 500 μW, 532 nm excitation source, exciting the native background luminescence of the Si_3N_4 to couple into the cavity and collecting PL through a 0.9 NA objective. Representative cavity modes are in the range from 580 to 605 nm, which are displayed to the right side of the respective areas. All measured Q-factors ($Q = \lambda/\Delta\lambda$) from this region are plotted in Figure 6.3(e), which illustrates that the performance of cavities that were covered with hBN (2700 ± 530) is on par with that of plain cavities of 2730 ± 430. The almost identical device performance emphasizes the advantage of the developed fabrication protocol that was used in this study.

6.3.3 Observation of Integrated Single Photon Emitter

We observed quantum emitters at the centre of PCCs, whose ZPL partially or highly overlapped with a resonant mode. Characterization of emitter–cavity systems was done at room temperature under 532 nm laser excitation (cw, 75 μW).Figure 6.4(a),(b) show examples of two coupled emitters, which are referred to below as Cavity 1 and Cavity 2, respectively. For both cases, we observed the emitter location to be near the nanobeam centre, as evidenced by PL maps in Figure 6.4(a),(b) (I). Spectra (II) collected from the white outlined spots show ZPLs at 588 and 593 nm, respectively (red curves), while for Cavity 1 the spectral features of the emitter are distinctive from the cavity resonance at 595 nm, due to a low degree of coupling, and for Cavity 2 the shape of the ZPL could not be clearly distinguished from the cavity mode due to a high degree of coupling. Q-factors of both cavities (insets) were determined by a Lorentzian fit and correspond to 1700 and 2400, respectively. To confirm their single photon nature, we spectrally filtered the collection signal by bandpass filters (578–598 nm and 583–603 nm, respectively) and measured the second-order correlation functions, $g^{(2)}(\tau)$.

Experimental data are fitted (without background correction) to a double exponential function as shown in red, and we obtained $g^{(2)}(0)$ values of 0.3 and 0.1 for the two emitters.

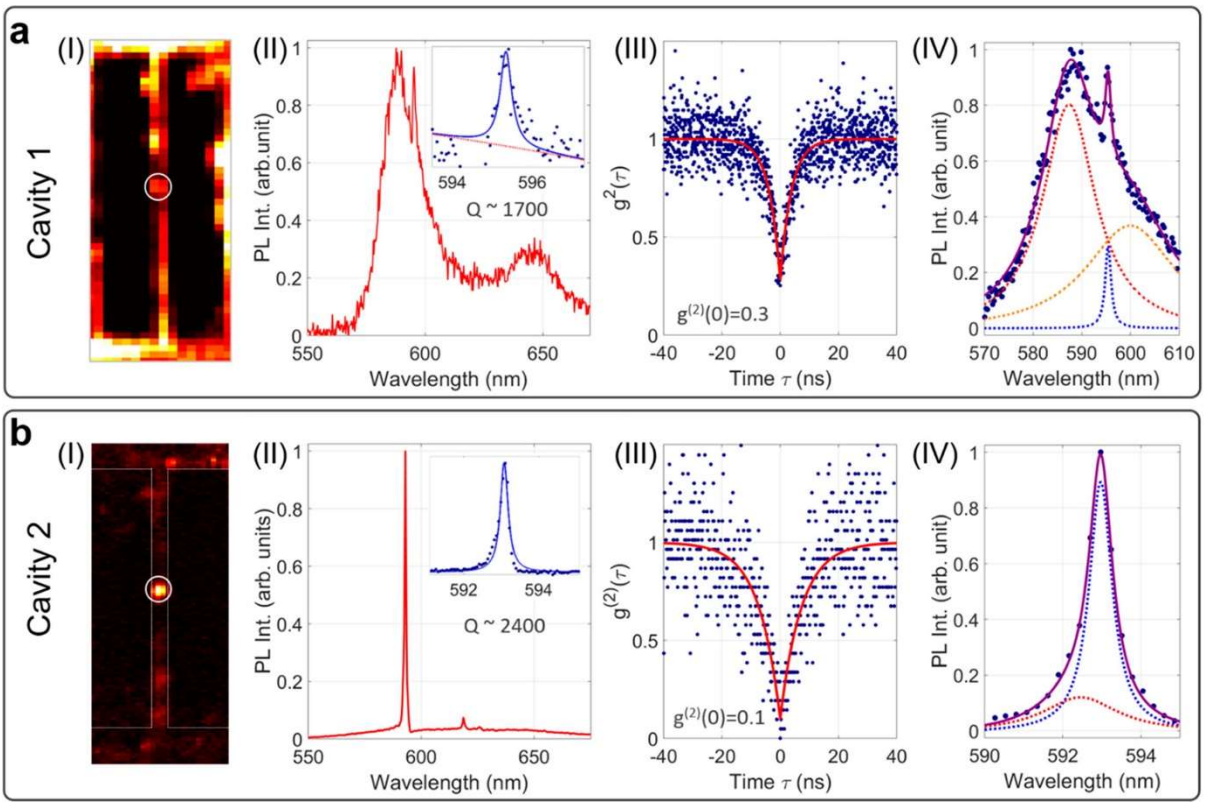

Figure 6.4. Coupled hBN–Si_3N_4 system. Cavity 1 (a) shows partial coupling, while Cavity 2 (b) shows a high degree of coupling. (I) PL maps show the emitter positions within the respective cavities, being at or close to the centre of the device. (II) Spectra from the respective white-marked spots show the emissions of quantum emitters at 588 and 593 nm for Cavity 1 and Cavity 2, respectively. For Cavity 1, a distinctive resonance mode can be seen at 595 nm, while for Cavity 2 the ZPL cannot be clearly distinguished from a cavity mode. Insets show the cavity resonance determined from a measurement with a higher resolution grating. (III) Correlation measurements with $g^2(0)$ values of 0.3 and 0.1, demonstrating the single photon nature of the emitters. (IV) The ZPL from the coupled system was, in each case, fitted with a sum of Lorentzians (purple) to estimate the respective contributions from the emitter (red and yellow) and cavity (blue).

To estimate the PL enhancement at the cavity resonance, we further fitted the respective ZPL and cavity mode as a sum of Lorentzian functions (purple), shown in (IV). For Cavity 1, we considered a sum of three Lorentzians corresponding to the main ZPL (red), the broader red tail of the ZPL at lower energies (yellow), and the cavity mode (blue). We note here that the role of the second Lorentzian is still not fully understood and a current point of debate in the

literature, assuming it to be a second ZPL or an acoustic phonon sideband.[45] In the case of Cavity 2, a sum of two Lorentzians was used for the fit, assuming that the main portion of the coupled system is a Lorentzian cantered at 593 nm (blue) and a partially uncoupled component (red) cantered at 592.5 nm. To evaluate the PL enhancement due to the cavity, we compare the relative intensities of the cavity mode extracted from the fits in Figure 6.4 (IV) relative to the uncoupled emission. In particular, we calculate the enhancement factor as the total emission at the cavity resonance (purple) over the total emission minus the cavity related emission (blue). Thus, Cavity 1 exhibits a PL enhancement up to 1.5, and Cavity 2 is estimated to have up to 9 times PL enhancement. This PL enhancement is the highest achieved value for hBN quantum emitters to date. It can be further increased by improving the field overlap with the resonant mode, *e.g.*, by increasing the angular match between the emitter dipole orientation and the cavity polarization or increasing the spatial match between the emitter location and the mode intensity maximum. In an ideal scenario, emission rate (i.e., lifetime) reduction for the coupled vs uncoupled emission should be measured at cryogenic temperatures. Unfortunately, at this point most studied hBN quantum emitters bleached within the time frame of the experiments, which prohibited controlled tuning of the same system. Techniques to mitigate this problem are currently being pursued. We further note that emitters in unprocessed hBN seemed to be equally unstable and at this point cannot give distinct evidence that the processing steps reduce the quality of the emitters. However, it is very likely that this is the case, similar to other systems, where the introduction of a nanostructure around the quantum emitter does impede its properties.[214]

6.3.4 Observation of Spectral Shifts and Momentary Coupling

Nonetheless, occasional spectral jumps of the emissions enabled us to directly observe coupling between quantum emitters and cavity modes. For hBN quantum emitters, spectral diffusion over a range of several nanometres is common due to fluctuations in local electric fields caused by charge (de)trapping at surrounding defects.[215] Figure 6.5 shows an example of a spectrally jumping quantum emitter and a fixed cavity resonance. Time series of normalized PL spectra to the maximum intensity of the cavity mode is plotted in Figure 6.5(a). The ZPL of a quantum emitter was initially identified at 598 nm, close to a cavity mode at 593 nm. While it was only partially overlapping at first, we observe that, during the course of the PL measurement, a first shift of the ZPL occurred, which resulted in an overlap of the ZPL and the main cavity mode. Consequently, a second shift of the ZPL detuned the emitter from the cavity mode to 584 nm, followed by photobleaching, while the cavity mode was still observable. The

intensity at the ZPL increased from 1.9 to 9.3 after the first shift and decreased to 1.5 after the second shift, and thus we estimate sixfold PL enhancement. At the same time Lorentzian fits in Figure 6.5(b) show that for spectra 1 and 3 the main portion of the ZPL (red) can be clearly distinguished from the cavity mode (blue), while for spectra 2 the main contribution to the ZPL is virtually inextricable from the resonance and only a second phonon related part (yellow) contributes to the spectrum. Therefore, as the emitter location is fixed and the dipole orientation change is negligible, the PL enhancement in the second spectra is due to the maximum spectral matching between the optical mode and the quantum emitter. Note that spectral diffusion can on its own occasionally be associated with increased intensity. However, if that would have been the case, the cavity mode would have been broadened, (i.e., the shoulder of the emitter would have been more visible). Also the intensity of the emitter "as found" and after the second tuning is approximately the same. It is, therefore, safe to assume that the enhancement is due to the cavity and there is no intensity fluctuation due to spectral diffusion in our case.

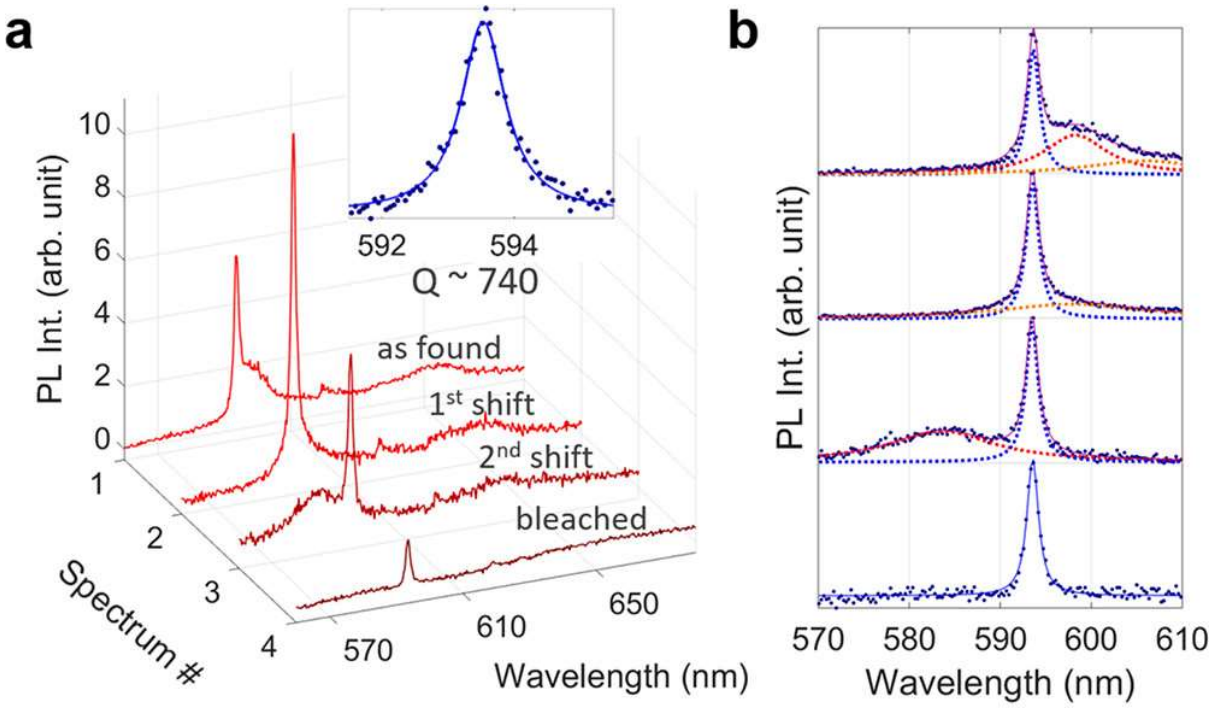

Figure 6.5. Dynamic enhancement of a quantum emitter which spectrally diffused to a cavity mode. (a) PL spectra, which are normalized to the maximum intensity of the cavity mode, measured with spectrally jumping emitter. As found, the emitter was partially overlapping with a cavity mode at 593 nm. A 1st spectral shift caused the ZPL to be coupled with the cavity mode. After a second shift, the ZPL was again detuned by 5 nm from the resonance. Then we observed bleaching of the quantum emitter. (b) The same PL spectra without normalization showing PL enhancement of the emitter. (c)

Lorentzian fits of spectra in (a). The ZPL (red and yellow) and the cavity mode (blue) were used to estimate the relative contributions, shown in the same order as in (a).

6.4 Conclusion

To conclude, we demonstrated a scalable approach for on-chip integration of quantum emitters in hBN with Si_3N_4. We overcome previous challenges where the ZPL was occurring randomly within the visible spectrum, prohibiting systematic investigations on coupling with dielectric cavity resonances. In particular, we make use of few-layer hBN grown by CVD, which yields a clear unimodal distribution of the ZPL cantered at 580 nm. Integration prior to the fabrication process allowed us to achieve large uniform device areas and to maintain high Q-factors up to about 3300. By direct comparison with devices from plain Si_3N_4 we have shown that the functionalities of devices integrated with hBN and without hBN are essentially unchanged, underlining the advantage of this processing approach. Owing to the high spatial density of emitters, we observed several cases of quantum emitters coupled to the mode resonance, achieving emission enhancements up to 9.

At this point, further experimental work was limited by bleaching of the quantum emitters. Therefore, while our work lays a solid foundation toward the realization of integrated quantum photonics with hBN, efforts must be concentrated to the improvement of the stability of hBN quantum emitters. This could potentially be achieved at the same time by encapsulating and protecting the hBN layer with a top Si_3N_4 film. Such an approach would make large scale nanophotonic chip fabrication feasible. Ultimately, the devised approach outlines the path forward to more sophisticated experiments using such hybrid systems based on hBN quantum emitters for integrated quantum networks with potential applications for quantum memories and applications as quantum repeaters.

Finally, we note that this approach is highly advantageous for other 2D materials, such as transition metal dichalcogenides (TMDs) that can also be integrated with dielectric cavities and waveguides. The common approach so far was the fabrication of the devices followed by transfer. Employing the presented technique, fabrication can become easier and more streamlined, particularly since TMDs have a relatively homogeneous emission across the flake. This can result in better monolayer lasers or improved coupling of quantum emitters in TMDs to photonic cavities.

Chapter 7

Nanobeam Cavities with Pockets for Efficient Integration of Nanoparticles

As an alternate pathway for hybrid integration we explored the potential of designing a photonic crystal cavity suitable particularly for hBN QDs [216] or nanodiamonds. Although we did not directly integrate them, due to non-ideal emitter properties of the source material available at that time. Nevertheless, this chapter describes a novel pathway for fabrication and photonic cavities particularly suitable for nanoparticles. The original idea of this project was conceived by Johannes E. Fröch. Johannes E. Fröch, Sejeong Kim and Igor Aharonovich designed the experiments. Johannes E. Fröch developed and fabricated the photonic device samples. Sejeong Kim performed the photonic simulations. Johannes E. Fröch carried out the optical measurement, plotted and analysed the data for figures. Connor Stewart conducted the PL measurement for *Q*-factor characterization. Xiaoxue Xu and Ziqing Du provided UCNPs. Johannes Fröch and Mark Lockrey performed the CL measurement. Johannes Fröch, Sejeong Kim, Milos Toth, and Igor Aharonovich wrote the manuscript. All authors contributed to the discussions.

7.1 Introduction

Fluorescent nanoparticles have become indispensable elements in contemporary fields of science and research.[22,217,218] In the realm of quantum technologies and nanophotonics, there is great interest in increasing the emission rates from nanoparticles by modifying their photonic density of states via coupling to dielectric or plasmonic cavities.[128,130,132,209,219-226] Such hybrid systems can then be harnessed to realize low-threshold lasers or utilized for quantum sensing and quantum cryptography applications.[126,227-233] Moreover, on-chip integration of nanoparticles with scalable photonic elements is essential for the deployment of single photon sources in scalable quantum photonic applications.[127,234]

The advantage of plasmonic cavities lies in their ease of coupling because of spectrally broad resonances. However, the devices are then inherently lossy due to metal absorption. Conversely, photonic crystal cavities (PCCs) offer near-lossless operation, but integration is complicated due to spectrally narrow resonances. In both systems, nanoparticle placement accuracy is essential for efficient coupling to cavities. This is a significant challenge that has thus far not been resolved adequately. Pick-and-place techniques are time-consuming and cumbersome;[235] two-step methods based on device fabrication and subsequent aligned-placement have low success probability and are applicable to a limited range of systems;[222,225] and random dispersion of nanoparticles on cavities often results in unwanted residues that impede device performance.

7.2 Methods

7.2.1 Device Fabrication

A detailed description of the fabrication steps, given in Figure 7.2(a), is as follows: (I) A resist (CSAR 62 11%, ALLRESIST GmbH.) was spun (500 nm) onto a Si_3N_4 (180 nm) on Si substrate and prebaked at 160 °C for 1 min. Then, EBL (Zeiss Supra 55 VP and RAITH EBL system) was used to define the cavity pattern including a hole with an 80 nm diameter at the centre of the nanobeam. After developing the E-beam resist, the pattern was transferred into the underlying substrate using RIE (90 W, 300 V self-bias, 60 sccm, 10 mTorr) with SF_6 as the reactive gas. After RIE, the substrate was immersed in a solution of nanoparticles. During solvent evaporation, nanoparticles are assembled inside pockets. The resist film was then stripped off in a heated acetone bath which removes the remaining resist and excess nanoparticles other than those located in the nanopockets. In a final step the nanobeams were undercut, using a 20 wt. % KOH solution (40 °C, ~20 min) etching the silicon underneath.

7.2.2 CL Characterisation

The device presented in Figure 7.3(a) was analysed in an FEI DB235 instrument equipped with a DELMIC SPARC CL system operated at an acceleration voltage of 10 kV and beam current of 4 nA. Acquisition time per pixel was set to 500 ms and dispersed by a 1800 lines/mm grating with the entry slit opened to 2 mm to maximize the collected signal.

7.3 Results and Discussion

7.3.1 The Pocket Cavity Concept

Here, we provide an elegant solution for hybrid integration of nanoparticles and dielectric cavities. We design and implement a one-dimensional (1D) PCC with a fishbone-shaped geometry and a nanosized pocket for efficient integration of fluorescent nanoparticles, as shown in Figure 7.1(a). This design overcomes problems encountered with common 1D PCCs (Figure 7.1(b)), which consist of a suspended beam and a series of air holes. In this case the altering refractive index between low (L)- and high (H)-index regions, give rise to a photonic band gap, while modulation of the periodicity then introduces a photonic well at the centre, confining light at the core of the nanobeam. However, a nanoparticle located on top of the cavity would only weakly interact with the optical mode formed in such a resonator. To increase this interaction, a pocket can be introduced into the central H region of a PCC as indicated for the fishbone type cavity.[236] In the following, the rationale for the chosen geometry is given by two practical aspects. First, placement of nanoparticles by dispersion may easily clog air holes and hence introduce scattering and decrease the refractive index contrast along the propagation direction of the optical mode. This in turn can easily jeopardize the device functionality. In contrast, for a fishbone type cavity, (excess) nanoparticles can only attach to the sides of the nanobeam; thus, disturbance due to nanoparticles for a propagating mode would only be present in the evanescent field, rendering this design more robust for practical applications. Second, the footprint of a pocket relative to the fishbone structure is smaller as compared to air holes. This directly allows the exploiting of etching-lag in the same fabrication cycle to form a pocket, instead of etching a complete hole, as demonstrated in a later section. Not only does the structure allow for highly efficient coupling of emitters placed inside the pocket to the cavity, but also, the presence of a nanoparticle reduces the effective mode volume and increases the degree of light confinement.

The material of choice for the PCC is silicon nitride (refractive index $n = 2$), due to its wafer scale availability and established fabrication recipes. The interaction with a nanoparticle is analysed using a photonic simulation tool (Lumerical Inc.) based on the finite-difference time-domain (FDTD) method. A nanopocket with both diameter and depth of 80 nm is introduced in the middle of the fishbone cavity, where structural parameters are defined as follows: lattice constant (a) = 230 nm, backbone width (b) = 120 nm, bar width (w_b) = 100 nm, bar length (l_b) = 500 nm, and thickness (t) = 180 nm. To form a photonic well, the periodicity is then linearly

decreased toward the centre of the nanobeam. Electric field intensities for the cases with and without a nanopocket are shown in Figure 7.1(c),(d), respectively, with a top (I), cross-sectional (II), and a magnified cross-sectional (III) view. For comparison, the electric field intensities are normalized to the same scale. This comparison clearly shows that the optical mode and the nanoparticle interaction is stronger when the particle is placed in the pocket. The intensity at its centre is 5.5 times higher than for a nanoparticle placed on top of the cavity. Moreover, nanosized gaps between particles and pocket sidewalls give rise to tight light confinement that results in a mode volume of $V \sim 0.015\ (\lambda/n)^3$.

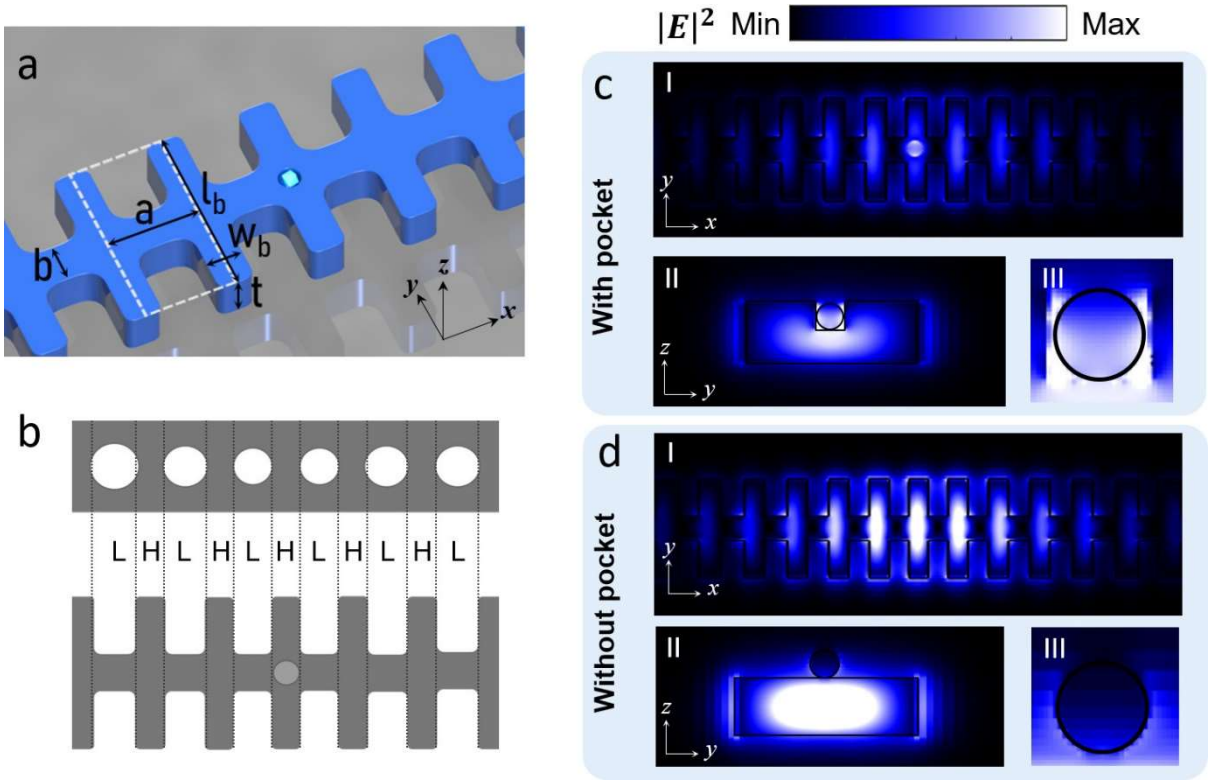

Figure 7.1. One-dimensional fishbone photonic cavity design. (a) 3D schematic of the proposed fishbone photonic crystal cavity (PCC) design with a nanopocket placed in the middle of the cavity to host a fluorescent nanoparticle. The unit cell of the fishbone photonic crystal outlined by white dashed lines with periodicity a, backbone width b, bar length l_b, bar width w_b, and thickness t. (b) Refractive index modulation induced by altering regions of high (H) and low (L) refractive index either via air holes or by placing nanobars periodically on a backbone. FDTD simulation results showing the electric field intensity of the cavity (c) with a nanopocket and (d) without a nanopocket with (I) top-view, (II) cross-sectional view, and (III) magnified view at the nanoparticle cross-section.

To the best of our knowledge, this is the smallest mode volume that was achieved for a dielectric cavity in the visible spectral range and comparable to the most efficient designs in the infrared spectral range.[237-240] The ultrasmall volume can be intuitively considered as a second level of spatial localization, i.e., light is first confined in the photonic band gap, and then, the pocket further localizes the light due to electromagnetic boundary conditions. We note that similar ultrasmall mode volumes were previously achieved using plasmonic cavities, but these suffer from metallic losses, oxidation, and challenges in assembly to typically sub 15 nm hot spots.

7.3.2 Fabrication

Following the conceptual design of the fishbone-pocket cavity, we realized it experimentally, based on the fabrication steps outlined in Figure 7.2(a) (detailed in the Methods Section). The process flow consists of (I) spin coating of the resist on a substrate, (II) electron beam lithography (EBL), (III) reactive ion etching (RIE) and immersion of the patterned substrate in a nanoparticle solution for particle placement, and (IV) resist stripping and undercutting. A critical aspect of this work is the development of a single-cycle fabrication process, in which the cavity and the pocket are patterned and etched during the same EBL and RIE steps, respectively. This is possible, by taking advantage of RIE lag, where smaller features of the mask are etched at a slower rate, as compared to larger ones. Accordingly, a nanopocket is automatically formed while the outline of the fishbone cavity is etched entirely. The described mechanism was observable by inspection in an SEM, as shown in Figure 7.2(b) for a set of free-standing PCCs after fabrication. In a magnified view (Figure 7.2(c),(d)) of the highlighted areas, it is clear that the outlines of the device are clearly defined and etched entirely. Moreover, we observed successful particle placement inside pockets as shown in Figure 7.2(d). Furthermore, the characteristics of the pocket were directly confirmed by taking a cross-section, shown in Figure 7.2(e). Here, a cross-section along the centre of the device clearly shows the formation of the intended pocket, which is etched approximately halfway through the slab. We emphasize that achieving different etching depths in a single RIE step is crucial and practical as scalable applications require minimum fabrication steps. In addition, it alleviates the stringent requirements of high alignment precision to create a pocket in a subsequent fabrication step for a prefabricated cavity.

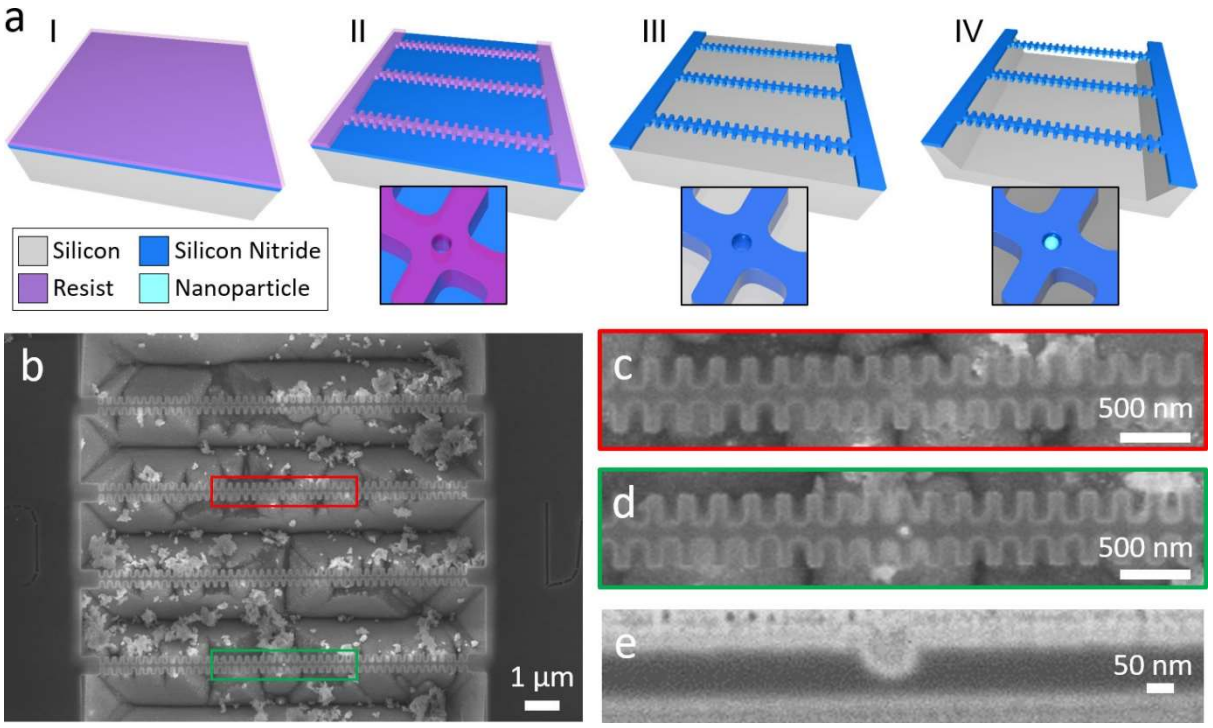

Figure 7.2. Fabrication of pocket cavities. (a) Schematic outline of the cavity fabrication scheme: (I) resist application on a SiN/Si substrate, (II) patterning of the cavity outline and the nanopocket in the centre by EBL, (III) RIE placement in a nanoparticle solution, and (IV) final undercut of the cavity structure. (b) Set of PCCs after fabrication showing no nanoparticle contamination on the top of the cavity. Magnified SEM images showing cavities (c) without a nanoparticle and (d) with a nanoparticle in the nanopocket, respectively. (e) Cross-section of a pocket cavity showing halfway through the etched area of the nanopocket due to the RIE lag effect.

7.3.3 Device Characterisation

In the next step, we fabricated PCCs with resonances over a larger spectral region, 590–670 nm, a range relevant to a myriad of commonly deployed nanoparticle types (e.g., nanodiamonds, colloidal quantum dots, upconversion nanoparticles). Mode properties, device characteristics, and the influence of the introduced pocket were then assessed using cathodoluminescence (CL) and photoluminescence (PL), as specified in the Methods Section. An SEM image of the fishbone cavity investigated for the conducted CL measurement is shown in Figure 7.3(a). To reveal the spatial extent of the optical mode, a CL spectral map was collected in the blue outlined area with a pixel size of 20 nm. The average collected spectrum in the entire region (blue) is shown in Figure 7.3(b) and compared to an averaged spectrum

over the cavity centre (red), showing a clear resonance at 595 nm. We note that the line width of the displayed resonance is limited by the spectral resolution, with the entrance slit fully opened (2 mm) to maximize the collection during measurement. By integrating the CL signal from 593 to 597 nm an intensity map of the resonant mode could be reconstructed and correlated to the SEM image as shown in Figure 7.3(c). This result matches well to the simulation, shown in Figure 7.3(d), visualizing the fundamental cavity mode with the maximum intensity at the centre of the device.

Spectral device characteristics were then determined by PL measurements (532 nm excitation). A representative direct comparison of 2 PCCs, fabricated under identical fabrication conditions, with and without pocket, is shown in Figure 7.3(d). As could be expected, the cavity with a nanopocket has a lower *Q*-factor (Q = 1100) compared to a cavity without pocket (Q = 2400) with a resonance blue-shifted by 3 nm due to a reduced effective refractive index. A statistical analysis of over 20 cavities with (red circles) and without (blue crosses) pockets is shown in Figure 7.3(e), showing both tendencies over the entire range. Moreover, we observed an increasing trend of *Q*-factor with resonant wavelength for pocket cavities, which is likely the result of reduced scattering from the nanopockets. Specifically, for features such as surface roughness or in this case a nanopocket the scattering cross section is determined by the feature size relative to the wavelength with an increased scattering cross section as the feature size is larger.[241] Therefore, if the feature size of the nanopocket is maintained, but the wavelength of the resonance is increased, the scattering due to the nanopocket is reduced and hence the *Q*-factor is larger.

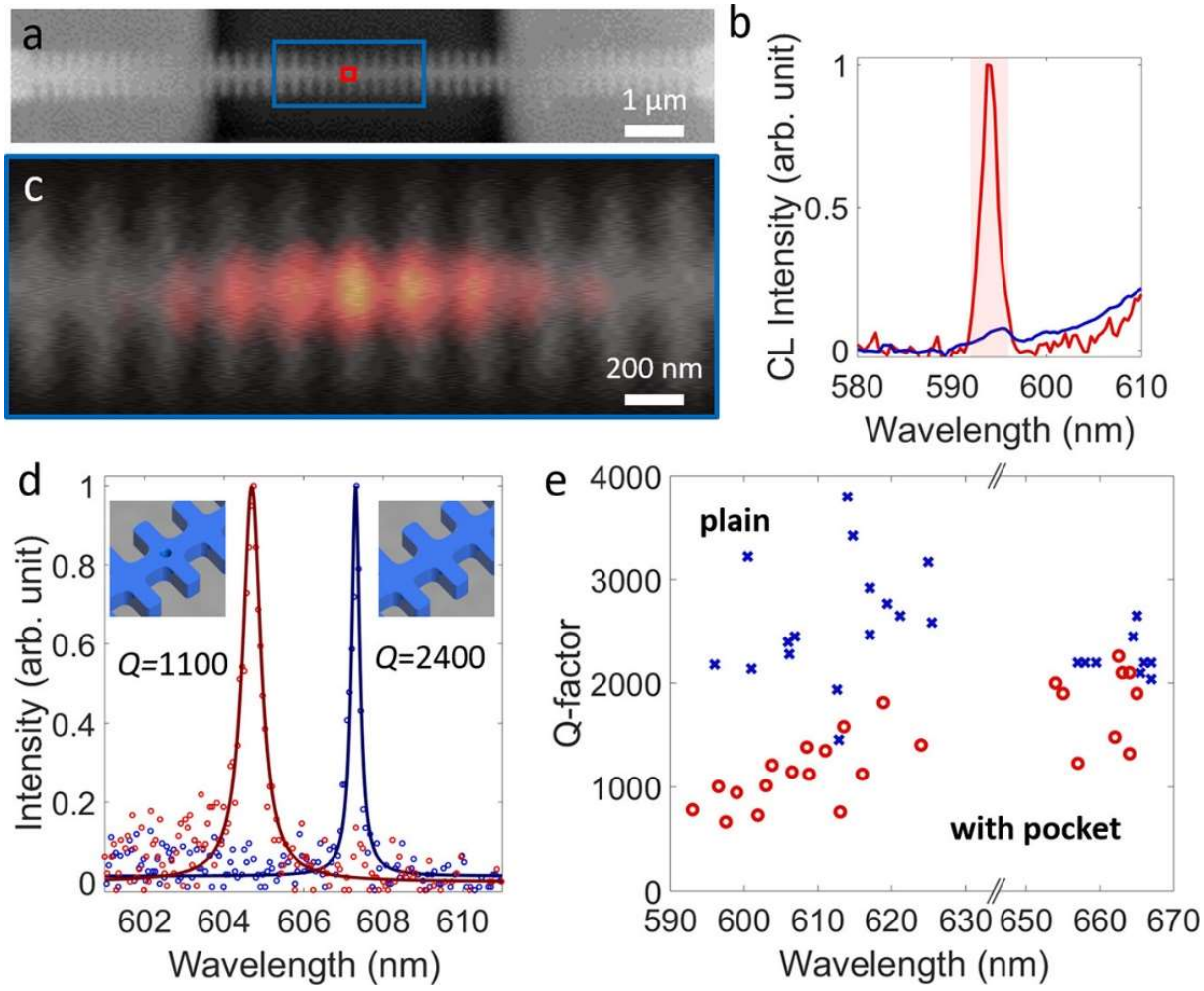

Figure 7.3. Spatial and spectral characterization of pocket cavities. (a) SEM image of the cavity investigated for the CL measurement. (b) Spectral response in CL of the structure averaged over the entire mapped area (red) and over the cavity centre (blue), showing a resonant mode at 595 nm. (c) 2D intensity map showing the spatial distribution of the optical mode at the cavity centre. (d) Representative PL spectra showing cavity modes from PCCs with and without a nanopocket. (e) Q-factors of all investigated PCCs in the range 600–680 nm, determined from PL spectra (grating: 1200 lines/mm).

7.3.4 Coupled Cavity Particle System

Next, we demonstrate the operation of the pocket cavity by enhancing the emission of the upconversion nanoparticles (UCNPs) and directly compare the cases of particles placed outside vs inside a pocket. For the pristine UCNPs we observe a representative emission spectrum as shown in Figure 7.4(a), with bands located at 521 nm, 544 nm, and 658 nm, corresponding to

de-excitation of the Er^{3+} after energy transfer from the primarily excited Yb^{3+}, shown schematically with the corresponding level diagram in Figure 7.4(b).

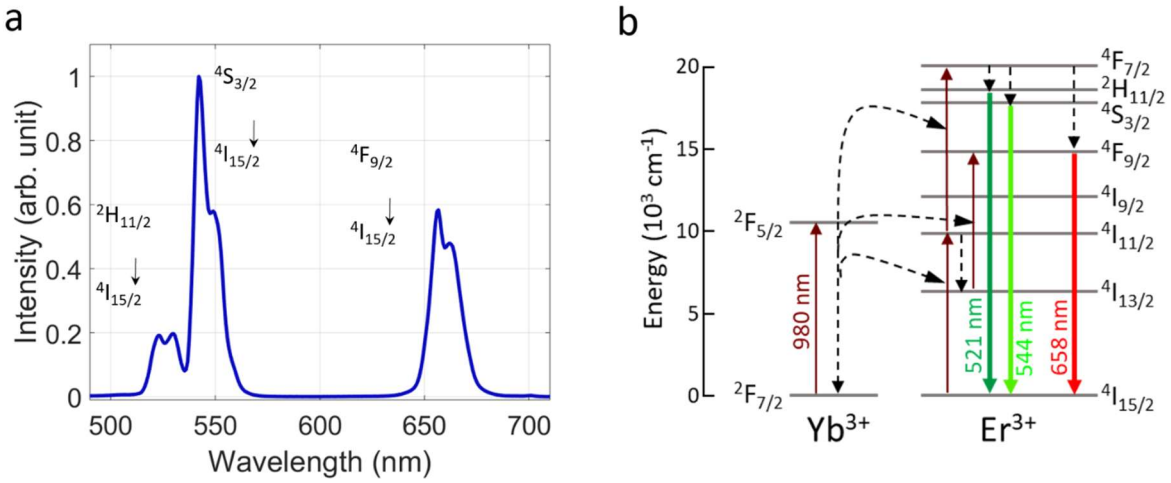

Figure 7.4. Spectral properties of the utilised UCNP. (a) Emission Spectrum under 980 nm excitation with notable emission bands at 520 nm, 540 nm, and 660 nm. (b) Level diagram for the upconversion excitation process of the Er^{3+}.

The spherical UCNPs (40 nm in diameter) of $NaYF_4$: 48%Yb, 2%Er dispersed in cyclohexane were drop-casted onto the cavities (during step IV, Figure 7.2), yielding devices with nanoparticles as shown in Figure 7.5(a),(b). For clarity, the excitation spot is marked red and the pocket indicated by a yellow arrow. While, for the device shown in Figure 7.5(a), particles (appearing dark in contrast) are placed aside the central pocket, we did observe clearly a nanoparticle in the centre for the second cavity, shown in Figure 7.5(b). Some UCNPs are visible on top and in between the bars of the fishbone cavity, but those did not degrade the experimentally measured Q as shown below. Fluorescent properties were determined at room temperature by PL measurement under 980 nm laser excitation (cw, 300 µW). Targeting the red emission band at 658 nm (the $^4F_{9/2} \rightarrow {}^4I_{15/2}$ transition, Figure 7.4), we then observed coupled emission of UCNPs to cavities, as shown in Figure 7.5(c),(d), for the case of a particle outside and particle inside a pocket. In particular, at the same resonance wavelength of 668 nm, we observed a 3.5-fold PL enhancement for particles placed outside the pocket (Figure 7.5(c)), as compared to a 20-fold enhancement for the particle in the pocket (Figure 7.5(d)). Despite a slightly lower Q-factor (1200) of the cavity in Figure 7.5(d) than in Figure 7.5(c), Figure 7.5(d) shows a higher PL enhancement than Figure 7.5(c) due to better spatial overlap between the optical mode and the UCNP.

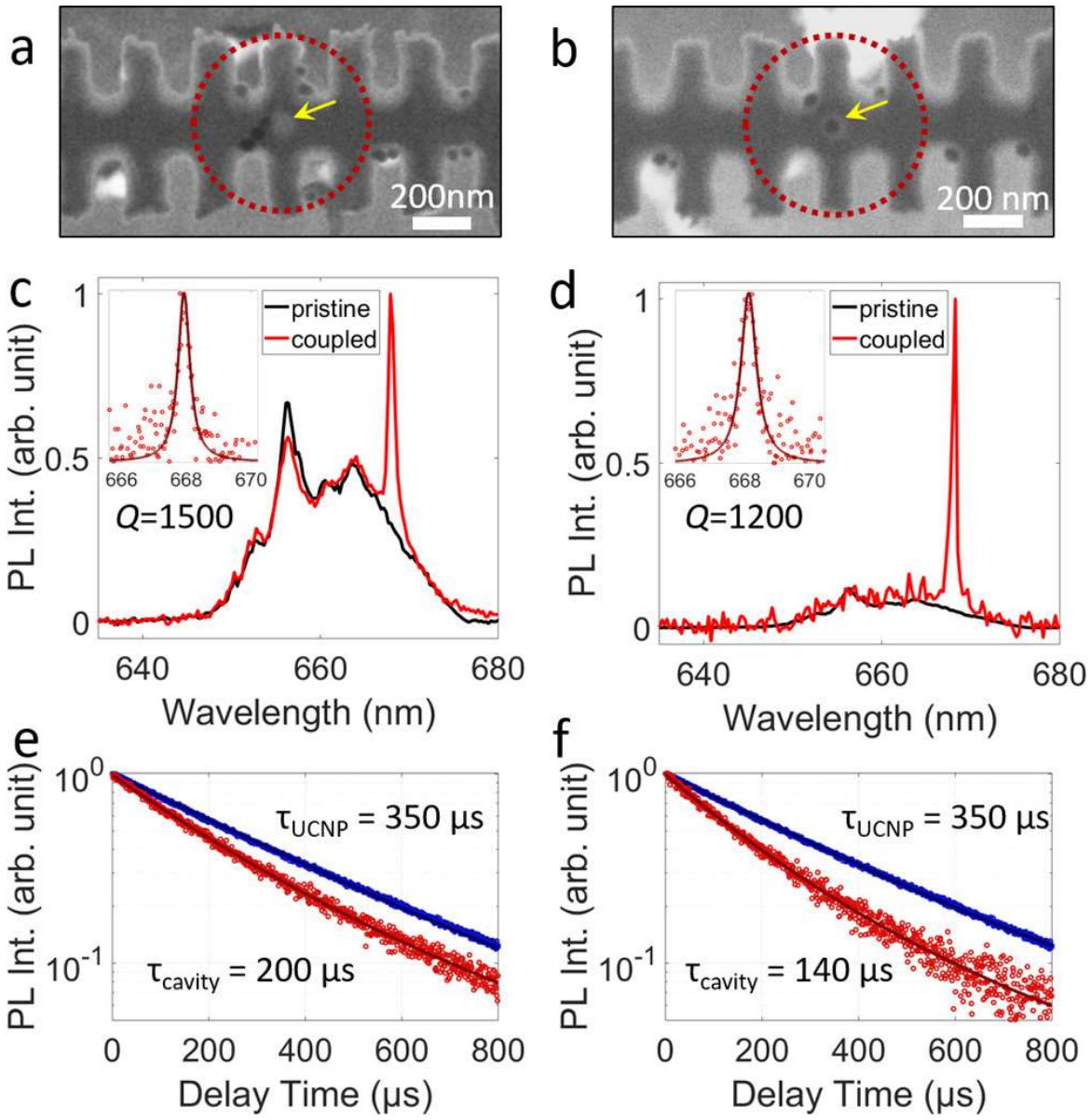

Figure 7.5. Fluorescent nanoparticles coupled to a pocket cavity. SEM images of UCNPs (black spots) on top of a cavity with particles placed (a) aside the pocket and (b) in the pocket, indicated by the yellow arrow. The red outline represents the approximate size and position of the pumping spot to identify particles that contribute primarily to the PL signal. (c, d) Spectra recorded from the respective cavities with a 980 nm cw excitation laser. (c) For the cavity with particles aside the pocket, we observe a 3.5-fold PL enhancement at the resonance (668 nm) with a Q-factor of 1500 (inset). (d) For the cavity with a particle in the pocket, we observe a 20-fold PL enhancement at the resonance (668 nm) with cavity Q-factor of 1200 (inset). Lifetime measurements for cavities, without and with a particle in the pocket, are shown in parts e and f, respectively. In both cases, a representative lifetime measurement of the UCNP is shown in blue, with a single exponential fit yielding a lifetime of 350 µs. Measurements on

cavities are shown in red, with a double exponential fit. For the cavity with particles outside the pocket, a lifetime of 200 µs was obtained. For the cavity with a particle in the pocket, a lifetime of 140 µs was obtained.

Further insight into the system was gained by lifetime measurements, pulsing the 980 nm laser, using an AOM. The collection was filtered with a bandpass filter and correlated to the pulsed excitation using a time correlator (Swabian Instruments). Background corrected lifetime measurements of pristine UCNPs (blue circles) and coupled to the cavity (red circles) are shown in Figure 7.5(e),(f), for the respective cavities. In the case of pristine particles, the lifetime is best described by a single exponential fit yielding a value of 350 µs. To determine the lifetime of the coupled part, a double exponential fit was used, with the first exponential factor fixed to the natural UCNP decay. From the fit, we then obtained reduced lifetime values of 200 and 140 µs for cavities, without and with the particle in a pocket, respectively. We note here that the presented factors for emission enhancement and lifetime reduction are in fact lower bounds. Because more particles are present in the excitation/collection spot, it is expected that only a portion of the observed PL (i.e., from the particles in the pocket or close by) was directly enhanced by the resonator.

Both the luminescence enhancement (20 vs 3.5) and lifetime reduction (2.5 vs 1.75) are significantly higher for a particle placed in the pocket, which directly underlines the general advantage of the integration strategy, where the field overlap is increased, and the mode volume is reduced. To estimate the Purcell factor of the presented cases, we followed the discussion, as presented in Englund et al.,[220] wherein the experimental Purcell factor F_e is derived as in Equation 7.1.

$$F_e(\lambda) = \frac{I_C(\lambda)}{I_0(\lambda)} \frac{\tau_0}{\tau_C} \qquad (7.1)$$

The Purcell factor at wavelength λ is given as the product of the ratios of the intensity enhancement and the lifetime reduction. This yields values of approximately ~50 and 6, for cavities with and without pockets. We emphasize, however, that these values are lower bounds for F, as more particles are present in the excitation/collection spot, which would then lead to a relative increase in the PL enhancement and lower lifetime. Particularly for the particle in the pocket, the relative discrepancy due to a better mode overlap and smaller mode volume is expected to be higher.

This value is compared to a theoretical value F_t, considering the fundamentally broader spectral width of the UCNP emission relative to the cavity resonance, in a modified Purcell factor, Equation 7.2. Here, λ is the resonant wavelength, V the mode volume, Q_{emitter} ($\simeq$ 50) the emission line width, μ the dipole alignment, and $\psi(r)$ the field overlap at the emitter position r.[132,226,242]

$$F_t(\lambda) = 1 + \frac{3\lambda^3}{4\pi^2 n^2}\frac{Q_e}{V}\mu\psi(r) \qquad (7.2)$$

We assume mode volumes of $\simeq$1 $(\lambda/n)^3$ for the cavity without the particle in the pocket and 0.015 $(\lambda/n)^3$ for the case of a particle in the pocket. Moreover, we consider field overlaps of 0.6 and 0.3 for the respective cases. For the dipole alignment a value of 0.3 is considered, corresponding to a spatial average for an ensemble randomly aligned to the fixed cavity polarization. In this case, we obtain theoretical values of 90 and 2, for a cavity with particle and cavity not in the pocket. The discrepancy for the former case can be attributed to the aforementioned underestimation of the PL enhancement and lifetime reduction, respectively. For the latter case, the mode volume on the other side may have been reduced, as compared to a typical value of $\simeq$1 $(\lambda/n)^3$, due to the introduction of additional gaps or the pocket itself. Nevertheless, the approximate difference in order of magnitude is mirrored in experiment and theory.

Although the enhancement was demonstrated with UCNPs, the cavity design is very applicable to enhance quantum emitters in nanodiamonds, especially the emerging group IV defects[23] that emit at the visible spectral range. Other immediate applications include nanoscale lasing with a vision of achieving single particle lasing that can be feasible with the current ultra-small mode volume. Placement of a single particle may be ultimately achieved by a 2-step EBL process, whereas in the first step the structure would be fabricated, while in the second step apertures would be opened directly at the centre of the pocket which would enable placement of single nanoparticles as discussed in similar works.[222] Finally, we note that the cavity design is also suitable for single molecules[197] that could be inserted into the cavity pockets.

7.4 Conclusion

To summarize, we proposed and realized novel 1D fishbone cavities with a nanoscale pocket for fluorescent nanoparticles. The presence of a nanoparticle inside the pocket reduces the mode volume significantly leading to a calculated modal volume of 0.015 $(\lambda/n)^3$. The cavities

are fabricated using a single step EBL-RIE, and the cavities exhibit high quality factors exceeding 1×10^3. As a proof of concept, we ultimately demonstrated the advantage of coupling a UCNP to a pocket cavity, where we achieved a 20-fold PL intensity enhancement and 2.5 lifetime reduction (corresponding to a Purcell enhancement of ∼50). This case is directly compared to a cavity with a particle not placed in a pocket, which yielded a 3.5 PL enhancement and 1.75-fold lifetime reduction. Overall, the demonstrated design is universally and immediately applicable to all types of fluorescent nanoparticles, such as nanodiamonds, UCNPs, or colloidal quantum dots, and tailored toward applications in nanoscale laser quantum photonics and sensing.

Chapter 8

Versatile Direct-Writing of Dopants in a Solid State Host

Based on the previous work, we determined that for future efforts of quantum emitter device integration a method for site specific creation of such is needed. However, at this point the most suitable technique for implantation into photonic nanostructures was Focused Ion Beam irradiation. This technique was however limited, due to the requirement of an appropriate source and special instrumentation. Therefore we explored other strategies for creation of quantum emitters. The original idea of this project was conceived by Johannes E. Fröch, Igor Aharonovich, and Milos Toth. Johannes E. Fröch carried out the experimental work, including sample preparation, ion beam irradiation, PL measurements, electron beam induced etching and AFM measurements. Alan Bahm performed simulations of recoil implantation. Mehran Kianinia, Sejeong Kim, and Carlo Bradac helped with optical measurements. Mu Zhao carried out cryogenic measurements, supervised by Weibo Gao. Vijay Bhatia and Julie M. Cairney helped with operation of the Dual Beam Microscope. Igor Aharonovich and Milos Toth supervised the work. All authors contributed to discussions. Johannes E. Fröch, Carlo Bradac., Igor Aharonovich and Milos Toth composed the manuscript with inputs from all authors.

8.1 Introduction

Much of solid-state science revolves around modification of materials at the atomic scale, where site-selective control over the incorporation and formation of defects within a host lattice enables control of physical, chemical and optoelectronic properties. Ion implantation has become a key tool in this regard, allowing for the modification of material properties for nanoelectronics, spintronics and quantum photonics.[53,243-245] Of particular interest is the generation of optically addressable qubits such as colour centres in diamond, silicon carbide (SiC) or yttrium orthovanadate (YVO_4) which are considered prime candidates for scalable quantum technologies.[54,123,138,246] Examples include the nitrogen vacancy (NV)

centre[76] and more recently the group IV elements[23,86,90,91,93,94,247] in diamond that exhibit excellent optical and coherence properties suitable for quantum circuitry.[88,98,248]
Over the last few decades, significant efforts have been committed to the deterministic creation of colour centres in solid state host materials by ion implantation.[37,249-255] While the technique is well established, there are fundamental constraints which limit its application in nanotechnology realisations. For instance, standard ion implanters employ beams that are too wide for direct-write patterning with a precision of tens of nanometres — requiring integration with mask-based lithographic techniques to achieve sub-micron lateral resolution. They are also generally ineffective for the implantation of foreign species into atomically thin materials such as graphene or transition metal dichalcogenides, [256] especially when high positional accuracy and lateral resolution is needed. To overcome these intrinsic limitations, focused ion beam (FIB) systems which can operate at low energies and can perform direct writing have been developed. The main drawback of these systems, however, is the narrow range of atomic species available to them: most are limited to elements that can be implanted from a liquid metal ion source. [257]
Here, we demonstrate a feasible method that targets these limits. Stemming from recoil implantation and ion beam mixing, [258-261] the method utilises an inert primary FIB to implant secondary species into a solid host by transfer of momentum. When the method was proposed over half a century ago, ion beam mixing/recoil implantation was mostly studied with a focus on mixing at the interface of adjacent layers, without demonstration of working devices. Nevertheless, the technique combines features which are usually displayed—individually—by different approaches: it works for a large variety of elements, it is maskfree, and it is capable of incorporating dopants with high spatial resolution (approximately tens of nanometres) and at shallow depth (approximately few nanometres). By combining capabilities that typically require a range of instruments and methods, the demonstrated approach to recoil-implantation is complementary to existing ion implanters and FIB instruments, and will broaden their capabilities and reach. It works for a wide variety of chemical species, it is particularly appealing for multi-elemental implantation—both in the context of co-irradiations and serial irradiation—and it can be used on target samples with non-trivial spatial features and geometries. We showcase this versatility by fabricating a range of optically active, atom-like emitters from solid-state precursors in bulk diamond as well as at the apex of an optical fibre—the latter being a particularly challenging sample for standard mask-based lithographic techniques due its nonplanar geometry.

8.2 Methods

8.2.1 Sample Preparation

A CVD-grown electronic grade diamond (<1 ppb Nitrogen) was purchased from Element Six. Before all subsequent experiments were carried out, the sample was cleaned in hot (150 °C) Piranha Acid (H_2SO_4:H_2O_2 (30%) 2:1) for at least 2 h. All thin film depositions were carried out in a lab-built magnetron sputter deposition chamber, pumped to a pressure of 1×10^{-5} Torr or lower before deposition. For deposition, argon was introduced with a pressure of 1.5×10^{-3} Torr and a plasma was ignited, for which the power was adjusted to yield a deposition rate of 0.5 Å s^{-1}. For the experiments were species were implanted into diamond, the sample was coated at four different corners with the respective thin films, whilst being masked during subsequent deposition steps to avoid cross deposition of different materials. For the patterning of the UTS logo, thin films were deposited on rectangular sections, lithographically defined using EBL. For implantation into an optical fibre or SiO_2, a 15-nm Eu film was deposited on top in a thermal evaporator using Eu pellets. Specifically, for implantation into the optical fibre, the entire fibre was rolled up and placed inside the evaporator chamber. The fibre was protected by aluminium foil, whereas only the end facets were exposed such that a thin film could be evaporated on it. We note that for potential industrial applications it would be more suitable to deposit a thin film on a shorter section of optical fibre and subsequently splice it if a longer fibre is required. Sputter targets and evaporation material were purchased from Changsha Xinkang Advanced Materials Co., Ltd with a purity of 99.99% or higher.

8.2.2 FIB Irradiation

All ion beam irradiations were carried out in a Thermo Fisher Scientific Helios G4 PFIB with exchangeable plasma ion source. For irradiation, a Xe^+ beam was used with an acceleration voltage of 30 kV and current of 10 pA. For irradiation of spot arrays and the UTS logo, custom patterning files (stream files) were created, defining the time per spot for individual spots (pixels). Box irradiations were performed, defining squares with 4-µm length and increasing the number of passes during the irradiation, using the built-in pattern generator.

8.2.3 Post Irradiation Treatment

For experiments on diamond, after irradiation with the Xe^+ FIB, the coated thin films were chemically stripped. We used subsequently two cycles of various solutions with intermittent water rinsing in between. First, the sample was held in KOH (30 min., 50 °C, 30 wt.%), then

HCl (30 min., 75 °C, 37 wt. %), followed by Piranha Acid (30 min, 150 °C H_2SO_4:H_2O_2 (30%) 2:1) to efficiently eliminate any residue of thin film coating on the substrate surface. After the chemical treatments the sample was annealed in a tube furnace (Lindberg Blue Mini-mite) under high vacuum with pressure lower than 2×10^{-6} Torr for the entire annealing cycle. The temperature was ramped up to 950 °C and held for 2 h. Then the furnace was cooled down to room temperature before breaking vacuum. After annealing the sample was again cleaned in hot (150 °C) Piranha Acid (H_2SO_4:H_2O_2 (30%) 2:1) for at least 2 h and stored in a desiccator in between experiments. For experiments on SiO2 and the optical fibre, the Eu thin film was removed after implantation in warm HCl 50 °C and subsequently water. No annealing step was performed to activate the Eu^{3+} related emission.

8.2.4 PL Measurements

All PL measurements were performed on lab-built confocal setups. The UTS logo was characterised using a 405-nm, 1-mW cw laser as the excitation source, which was directed through an arrangement of a dichroic mirror, scanning mirror and lens relay system and focused on the sample surface by a 0.9 NA air objective. PL from the sample was collected from the same objective and directed into a multimode fibre guiding the signal either to an APD (Excelitas) for mapping or to a spectrometer (Princeton Instruments). Lifetime measurements were conducted on the same configuration using either a 512 nm (for Si, Ge, Sn) or 405 nm (for Pb) pulsed laser diode as the excitation source. The fluorescence was correlated to the laser pulse using a correlator (Pico Harp 300, Picoquant). For the characterisation of the fibre core, the fibre was mounted in front of the air objective and a 2-mW, 532-nm cw laser was connected to the unimplanted end of the fibre to excite implanted Eu^{3+} in the core on the other end. At the same time, the collection was scanned in the same configuration. The characterisation of spot arrays and second order correlation measurements were done on a different setup. A 532-nm laser (cw, 2 mW) was used as the excitation source, and focused onto the sample by using an oil-immersion objective (1.3 NA). PL was collected through the same objective and coupled into a single mode fibre. The signal was either guided to a Spectrometer (Andor), or a 50/50 fibre splitter with the respective outputs connected to an APD. Their signals were then correlated by a time correlator (Swabian Instruments).

8.2.5 Electron Beam Induced Etching (EBIE)

EBIE of the diamond was done in a Zeiss EVO, under 15 keV, 2 nA and 100 mTorr H2O vapour. A rectangular area (16-µm length, 10-µm width) was irradiated (5-µs dwell time, 20-nm point pitch) in a raster scan. The length of the rectangle was reduced in subsequent steps by 2 µm, whilst the time/ area ($\simeq$1 s µm^{-1}) for each rectangle was held constant, thus achieving a linear fluence gradient resulting in the shown etch profile. After etching the diamond was again cleaned in hot (150 °C) Piranha Acid (H2SO4:H2O2 (30%) 2:1).

8.2.6 AFM Measurements

AFM measurements were done on a Park XE-7 AFM. Postprocessing of AFM data was done in XEI and Gwyddion to remove artefacts of the scan and to extract height profiles.

8.2.7 Ion Solid Modelling

The Monte Carlo ion-solid modelling (ISM) code used here is a multithreaded implementation of the binary collision algorithm (BCA), allowing fast computation as well as flexible definitions of surfaces and materials.[262] ISM has been validated against the commonly used SRIM program (Stopping and Range of Ions in Matter).[263]

8.3 Results

8.3.1 Concept

To implement the recoil implantation technique, we employ a readily available, unmodified dual beam system consisting of a coincident scanning electron microscope (SEM) and a FIB with a xenon (Xe) plasma ion source, as shown in Figure 8.1(a). The doping is performed by site-selective Xe^+ beam irradiation of a target that contains the desired dopant species precursor in the form of a thin film. At the atomic scale, momentum transfer from Xe (purple circles in Figure 8.1(a) inset) to the precursor atoms (red circles) causes the latter to be implanted into the underlying target. The process can yield ultra-shallow implant profiles, which is desirable for many applications.

As a benchmark for illustrating the versatility of this technique, we choose diamond, with a primary focus on a range of group IV elements in the periodic table: silicon (Si), germanium (Ge), tin (Sn), and lead (Pb). The reasons for the choice of host and dopants are as follows. First, diamond is available as an ultra-pure material with a wide bandgap and exceptional

chemical inertness, making it an ideal platform for investigations of extrinsic dopants. Second, colour centres in diamond, particularly the group IV-related negatively charged vacancy complexes, are currently front runner systems for a plethora of quantum photonic and quantum sensing applications.[23] Hence, a robust method to create these centres is desirable. Finally, these defects in diamond are optically active and can be imaged at a single photon level. This, in turn, allowed us to establish the efficacy of the proposed technique in the extreme case of advanced material systems which require engineering of individual, isolated atomic point defects. To perform the recoil implantation, the aforementioned group IV elements were deposited onto diamond using a standard sputtering technique (15-nm thickness). Then, a 30 keV, focused Xe+ ion beam was used to pattern the University of Technology Sydney logo, and the acronym "UTS" into the thin film sections using an ion beam fluence of 2.5×10^{13} cm^{-2}. After irradiation, the thin film was stripped using chemical processes and the diamond was annealed to activate the emitters (i.e. vacancy complexes of Pb, Sn, Ge and Si). Figure 8.1(b) shows a photoluminescence (PL) map of the implanted area. The UTS emblem and the letters U, T and S are clearly visible. Importantly, the emblem and each of the letters consist of a different dopant—Pb, Sn, Ge and Si, respectively—implanted using the same inert Xe^{+} ion beam. We stress that the doping is achieved by momentum transfer from the Xe beam to the aforementioned elements in the thin films deposited atop the diamond. The pattern is formed by electrostatic scanning of the ion beam with no additional lithography steps. The process is performed using a dual FIB-SEM system. All imaging and spatial alignments are therefore performed using the electron beam which is coincident with the ion beam at the diamond surface and serves as a passive imaging tool free from undesired implantation. Figure 8.1(c) shows PL spectra from the respective areas, featuring characteristic emissions of the four colour centres with zero phonon lines (ZPLs) at ≅550m (PbV), ≅620m (SnV), ≅600 nm (GeV) and ≅740 m (SiV). Remarkably, the colour centres are all optically active and bright, despite the fact that the dopant profiles are ultra-shallow, as is discussed below.

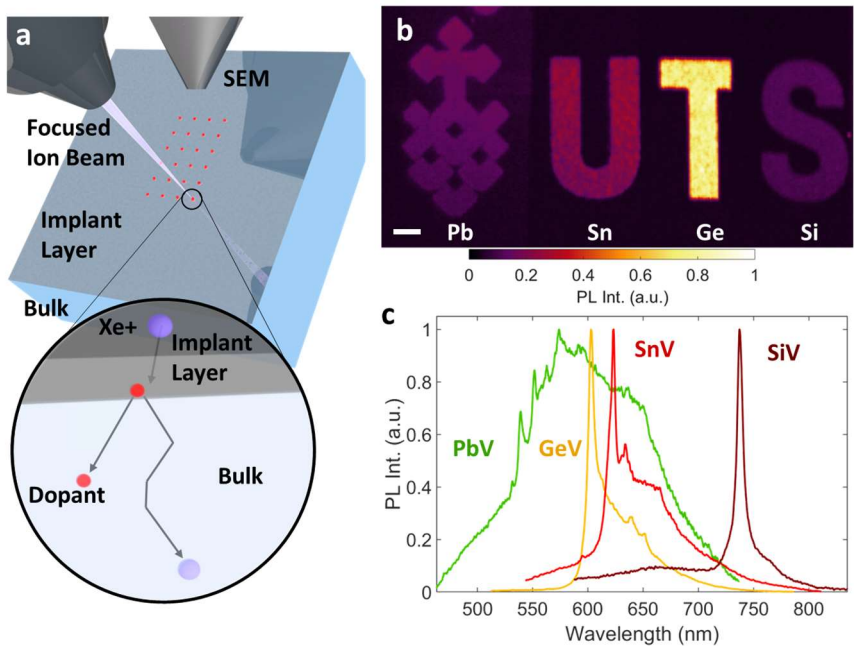

Figure 8.1. Creation of colour centres in a diamond target by recoil-implantation. (a) Schematic illustration of the process inside a standard electron-ion dual beam microscope. The inset shows an atomic picture of the process: momentum is transferred from inert primary ions to the atoms of a thin film comprised of the dopants, resulting in implantation of the latter into the underlying target. (b) Photoluminescence map of a pattern fabricated in a single region of diamond using four dopant species that were implanted by momentum transfer from an electrostatically scanned Xe^+ beam. The emblem is patterned in Pb, and the letters U, T, and S in Sn, Ge, and Si, respectively. The scale Bar corresponds to 5 µm. (c) Photoluminescence spectra recorded from the implants in (b), showing characteristic emissions from defect complexes that contain the Pb (green), Ge (orange), Sn (red), and Si (maroon) dopants.

8.3.2 Fluence and Spatial Control

We now turn to an in-depth analysis of the technique and the fabricated dopants, starting with the photophysical properties of the emitters. For this purpose, spot arrays (10 × 10) were patterned as a function of Xe^+ fluence, which was varied logarithmically for each of the aforementioned dopants. Analysis of the implanted areas was then conducted at room temperature using a confocal setup with an oil-immersion objective. A representative map of a Xe^+ fluence-dependent implantation series is shown in Figure 8.2(a). The image refers specifically to the case of silicon-vacancy (SiV) emitters, but identical arrays were also patterned for the other three elements (GeV, PbV and SnV). For all four elements, we observe

the emergence of the corresponding colour centre emission beyond a particular ion beam fluence (specified in Figure 8.2(a)). We note that the optical signals emerge after an annealing step, which promotes the formation of the fluorescent defect complexes, i.e. impurity atom adjacent to vacancy(ies), displaying PL emission. The observation of the emission above a particular Xe^+ fluence is related to the stochastic nature of the activation process, further discussed in Section 8.4.3.

The ion beam fluence needed to form an unambiguous observable pattern, specific to the 15-nm dopant film thickness used in our experiments, is on the order of 2.5×10^{13} cm^{-2}, 2.5×10^{13} cm^{-2}, 5×10^{13} cm^{-2}, and 5×10^{13} cm^{-2} for Si, Ge, Sn and Pb, respectively. This trend with atomic weight is intuitive given that the Xe^+ ions mill the 15-nm films via sputtering and simultaneously implant the dopants into the underlying diamond via momentum transfer. Additional details about the creation yield and further characterisation (atomic force microscopy (AFM) and PL) are presented and discussed in Section 8.4.3 and 8.4.4, respectively. We note that co-implanted Xe ions may also form luminescent colour centres in diamond, yet, their spectral features appear at 795 and 815 nm and do not overlap spectrally with the studied centres.[264]

Throughout the implanted arrays (fabricated as a function of Xe+ fluence), prominent ZPLs are observed at 738 nm (SiV), 602 nm (GeV), 620 nm (SnV) and 550 nm (PbV), as shown in Figure 8.2(b), which are characteristic of the respective colour centres. We note that an additional broad peak at 630 nm appearing in some of the spectra is the Raman signal of the immersion oil. Also, in the case of SnV, an additional peak at 595 nm is present, associated with intermediate defect configurations.[92] To confirm the quantum nature of the emitted light at the lowest implantation fluence, a second order autocorrelation function, ($g^{(2)}(\tau)$), was recorded from each of the emitters. The background-corrected $g^{(2)}$ (τ) curves are shown as insets in Figure 8.2(b). A clear dip below 0.5 at zero-delay time is observed for GeV, SnV and PbV-related emitters, confirming the single-photon nature of the implanted colour centres. We did not observe anti-bunching from the fabricated SiV colour centres, most likely due to their very low quantum efficiency.[265]

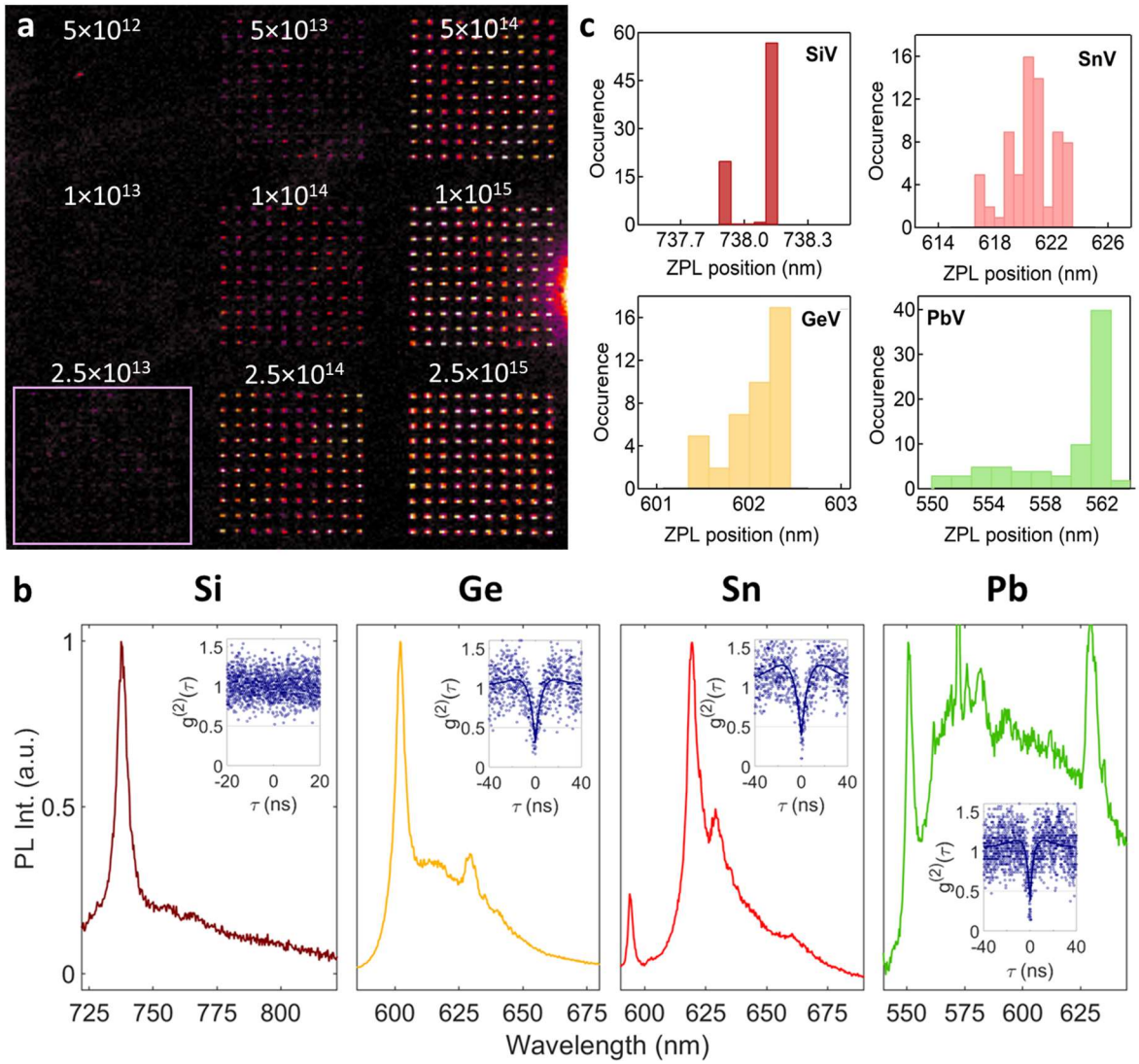

Figure 8.2. Spot arrays of dopants implanted into diamond as a function of Xe^+ fluence. (a) Photoluminescence map of a representative array, here shown for Si dopants. The framed area shows the lowest fluence of Xe^+ that yielded an unambiguous observable array in this case. The number above each array specifies the Xe^+ fluence in units of cm^{-2}. (b) Photoluminescence spectra of emitters from the lowest observable fluence of SiV (maroon), GeV (orange), SnV (red) and PbV-related emissions (green). An additional peak at 630 nm corresponds to the Raman signal of the utilised immersion oil. Insets show second order correlation measurements (background corrected), illustrating the quantum nature of the colour centres. (c) Histograms showing variability in ZPL wavelength in spot arrays of the colour centre ensembles.

Time-resolved PL measurements of ensemble colour centres, created in 4x4 um^2 boxes with a fluence of 3.1×10^{12} cm^{-2} were acquired using a 512-nm pulsed laser as excitation source and set to 20 MHz repetition rate. For acquisition of Pb-related colour centres, a 405 nm laser was

used as the excitation source. For all ensembles, the PL was spectrally filtered, such that a spectral window of ~20 nm with ZPL at the centre was collected. The signal was acquired by an avalanche photo detector and correlated to the laser using a high-resolution time correlator (Picoharp 300, PicoQuant). The decay curves are presented in Figure 8.3 for Si (a), Ge (b), Sn (c), and Pb (d), respectively. The data was fitted with a single exponential decay function shown as a solid line in each figure. We obtained values for the lifetimes of (1.5 ± 0.1) ns for SiV, (4.7 ± 0.1) ns for GeV, (3.9 ± 0.1) ns for SnV, and (3.5 ± 0.2) ns for PbV. The excited state lifetimes of the created defects are in accord with previously reported values.[23]

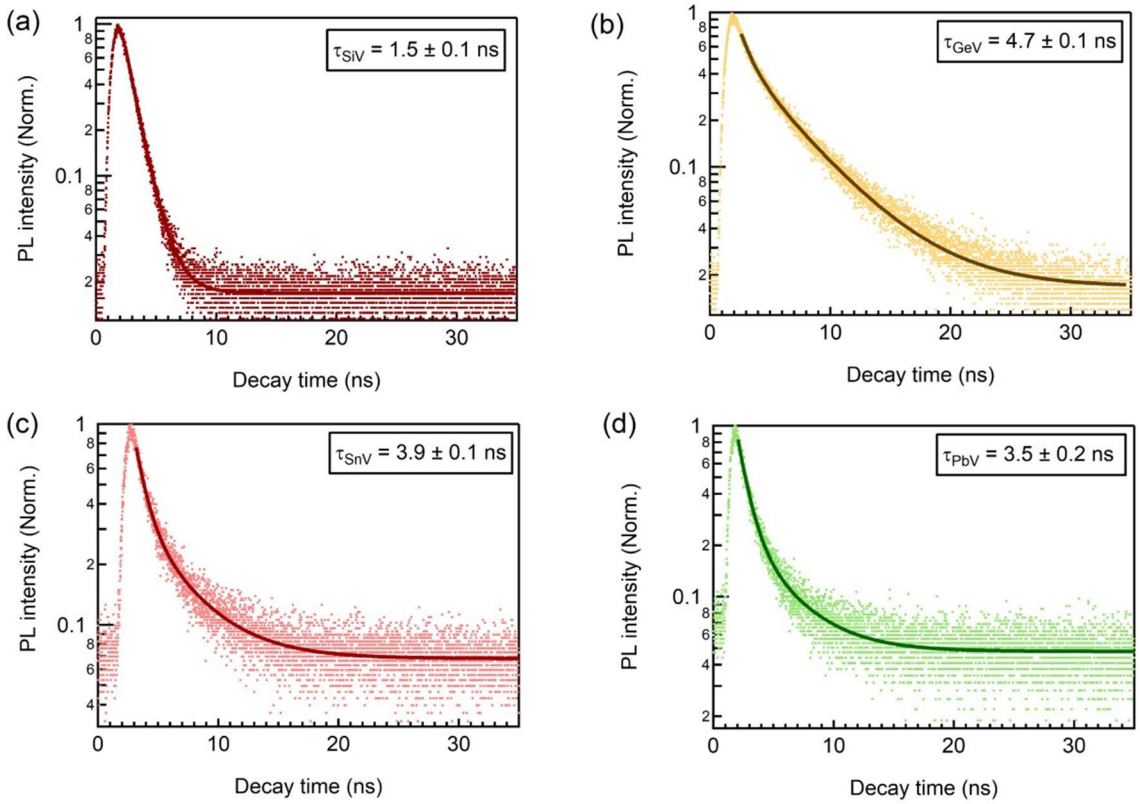

Figure 8.3. Lifetime measurements of implanted regions for SiV (a), GeV (b), SnV (c), and PbV (d) with the respective lifetimes determined from a single exponential fit, given in the top right corner.

To gain further insights into the emitter characteristics, the spot-implanted sites were studied at a cryogenic temperature of 4 K. PL spectra as well as photoluminescent excitation (PLE) spectra,[266] collected under excitation with narrowband lasers are shown in Figure 8.4 for SiV in (a) and (b), GeV in (c) and (d), PbV in (e) and (f), respectively. The central laser

frequency was set to 406.7THz for SiV, 497.743 THz for GeV, and 542.947 THz for PbV, respectively. From Lorentzian fits we obtained linewidths in PLE for SiV and GeV of 3.84 GHz and 4.73 GHz for the C Transition, respectively. Whilst for PbV spectral diffusion was observed and no conclusive value for the linewidth could be derived. This is likely related to the larger atomic size of Pb, and the associated large strain in the diamond lattice, which may in the future be alleviated by better annealing treatments. Nonetheless, resonant excitation of the emitters can be clearly observed for the SiV and GeV with sub 5 GHz linewidths. To the best of our knowledge, this is the first evidence of resonant excitation of sub-surface emitters. So far, resonant excitation was only carried out in bulk or in photonic nanocavities that still have a thickness of over 100 nm. Hence, it is remarkable that resonant excitation is even possible, despite the proximity to the surface.

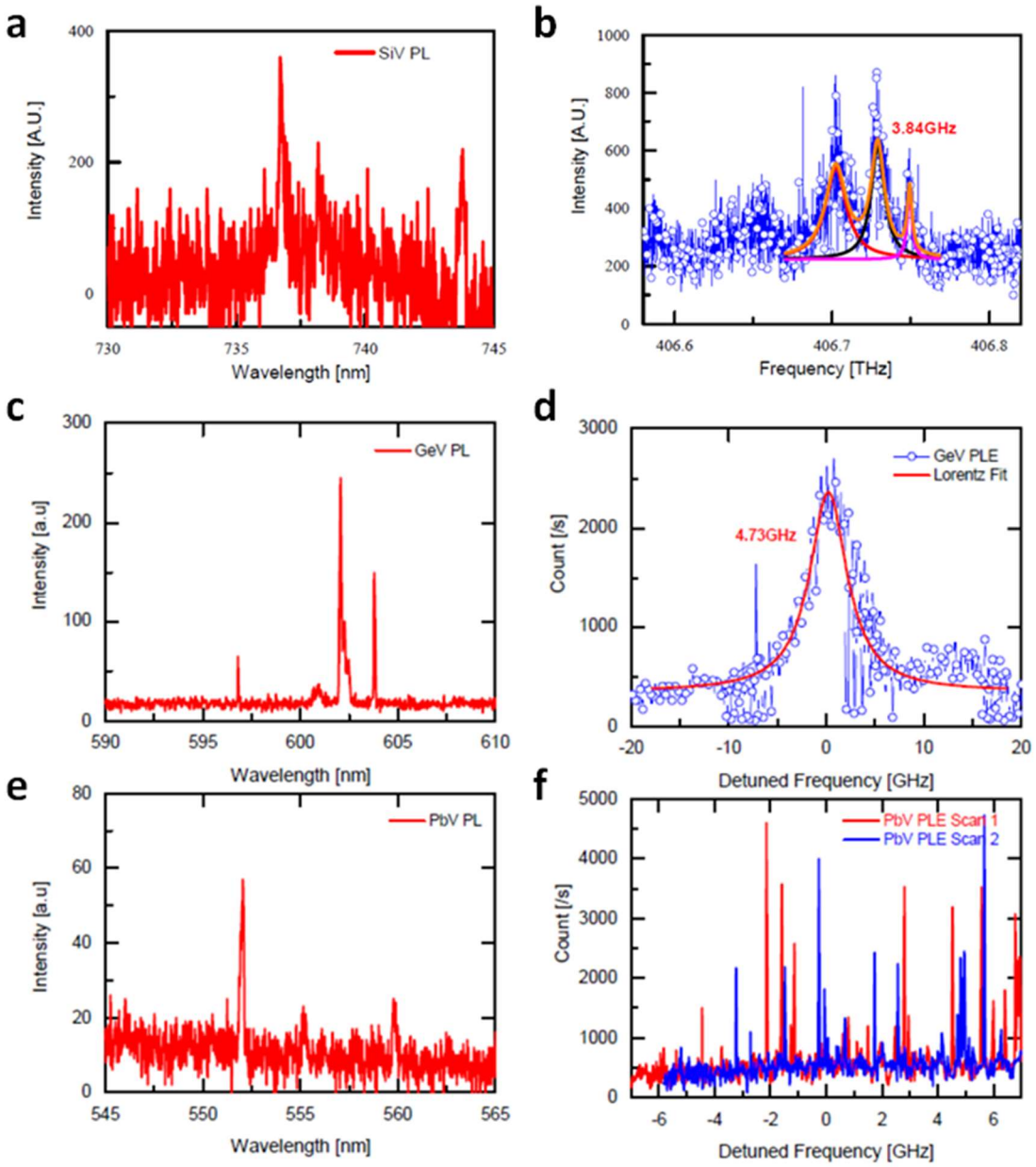

Figure 8.4. Characterisation at 4 K. PL (a) and PLE (b) spectra for spot implanted sites of SiV, (c) and (d) for GeV, (e) and (f) for PbV, respectively.

However, for applications relying on the coherence of the spin state of these defects, further post-processing steps (e.g. high-pressure, high-temperature annealing) may be needed to remove residual crystal damage. We further analysed the ZPL spectral properties of the ultrashallow emitters. Interestingly, the frequency of additional spectral lines increases with the size of the implanted species, which potentially indicates that these lines may be associated with intermediate defect states caused by additional strain in the diamond crystal. [92,93,267]

In particular, for SiV, as shown in Figure 8.5 (a), we only observed the main ZPL at 738 nm. For GeV, shown in (b), we observed primarily the main ZPL, and additional lines at ≅608 nm, ≅612 nm, ≅615 nm and ≅640 nm. Their occurrence was relatively low compared to the main ZPL, therefore these appear weaker in the spectra. On the other hand, For SnV (Figure 8.5 (c)), the number of additional lines and their relative intensity increased dramatically. We almost always observe a peculiar line at ≅595 nm. Additionally, lines at ≅630 nm seem to appear, which are however superimposed on the Raman signal of the on the immersion oil. Also, lines in the range 642 nm–647 nm, as well as ≅655 nm were observed. For PbV Figure 8.5 (d), the main ZPL was observed at 550 nm–560 nm, whilst further line-like features occur at ≅569 nm, ≅575 nm, ≅581 nm, as well as at ≅738 nm. Whilst some of these characteristics can be attributed to an increase in strain associated with dopant size, these results warrant further investigation, in particular towards optimisation of the annealing process. [92,97] Nonetheless, the recoil implantation technique is robust and can produce colour centres on demand, as demonstrated here with the group IV family in diamond.

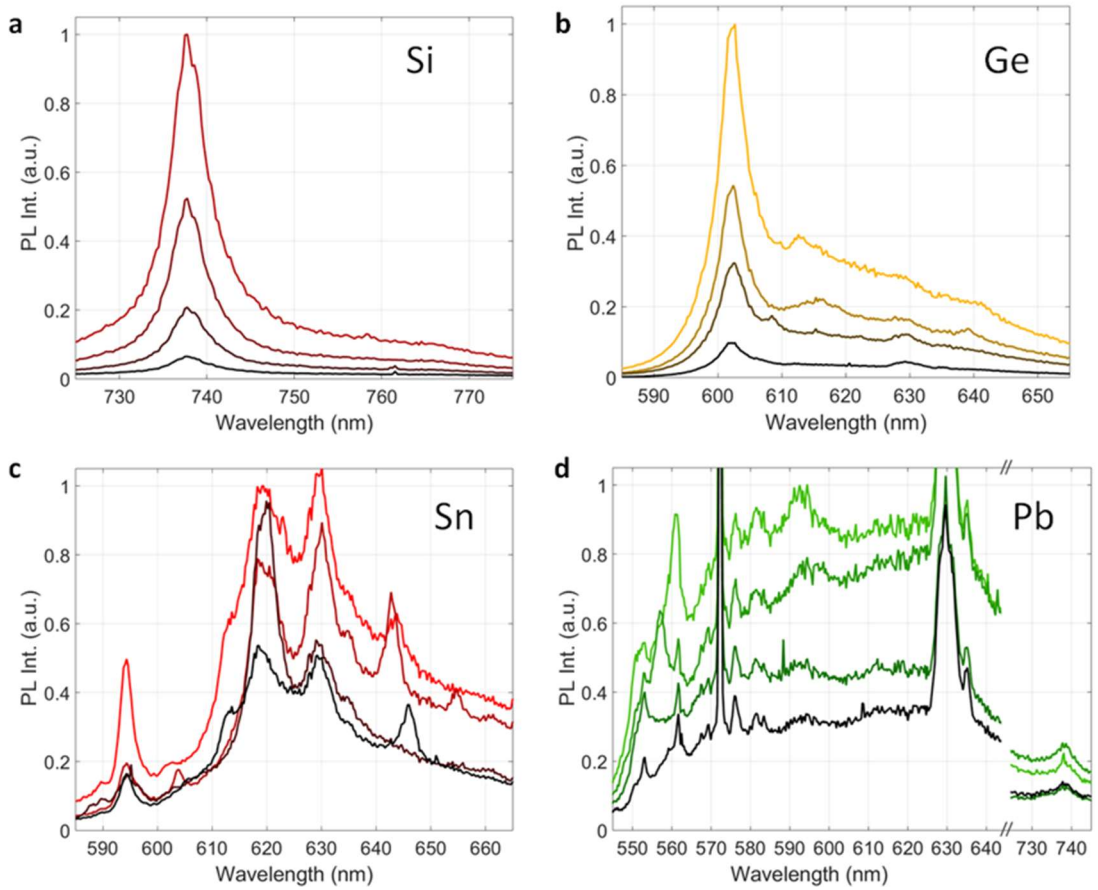

Figure 8.5. Averaged spectra over different dosages, normalised to the maximum of the highest fluence for Si (a), Ge (b), Sn (c), and Pb (d). The black lines correspond to the spectral average for the lowest observed fluence of the spot implantation series. The second lowest line (one shade brighter) corresponds to the next spot series and so forth.

8.3.3 Emitter Activation

Here we provide a rough estimate of the average creation yield for the GeV, SnV and PbV colour centres deduced from the dependence of PL intensity on fluence. We extracted the pixel intensities at emitter sites from PL maps (such as the one shown in Figure 8.2(a)). The average PL intensity as a function of the fluence for the various colour centres is shown in Figure 8.6(a). While these values for individual defects are comparable, we note that their absolute comparison should be taken with a high degree of caution, due to the utilisation of different spectral filters during the acquisition of the PL maps, used to maximise the contrast and clearly distinguish the spots. For each colour centre we observed the emergence of luminescence above a particular fluence, as mentioned in the main text, followed by a clear increase of intensity with fluence, which saturates for SiV and GeV at higher fluences, while no such saturation is observed in the case of SnV and PbV. The saturation is expected, as quenching is likely to

occur at higher fluences due to increased damage. The emergence of emission above a certain fluence is also expected, due the stochastic nature of the colour centre activation process. For implantation from a FIB the conversion yield was reported to be ~4% for SiV, [250] and ~0.4–0.7% for GeV, [251] respectively. However, in this case a focused ion beam was used, for which the conversion yield can be directly determined from the number of colour centres and the number of implanted ions. Since, in our case, the number of recoil implanted atoms does not directly correlate 1:1 to the primary Xe^+ ion fluence, we used the creation yield (colour centres generated per primary Xe^+ ion) as a comparable measure. In detail, the pixel intensity was related to the intensity of single emitters and a rough estimate of the created centres per Xe^+ ion was determined as shown in Figure 8.6(b). The number of created centres for SiV is not shown here, as it was not possible to unambiguously identify a single emitter experimentally. Therefore, the PL intensity of an actual SiV single emitter is likely lower, hence for similar average intensities, a higher number of colour centres as compared to other elements is expected. Comparing the different yields with each other, the lighter element Ge has at least 2 times higher number of created centres per Xe ion than the other elements. Moreover, for all colour centres we observe the highest creation yield at a fluence of 5×10^{13} cm^{-2}, followed by a reduction in the creation yield. This indicates that at higher fluences, the damage in the diamond lattice—introduced by primary Xe ions and recoil implanted atoms—was likely too high, causing quenching of the created colour centres. However, at this point it should be noted that all colour centres were created on the same diamond, which has undergone the same annealing treatment. This annealing treatment (limited by our tube furnace setup), likely resulted in a higher conversion efficiency for lighter implanted atoms into an optically active defect, which may explain the higher creation yields for lighter elements.

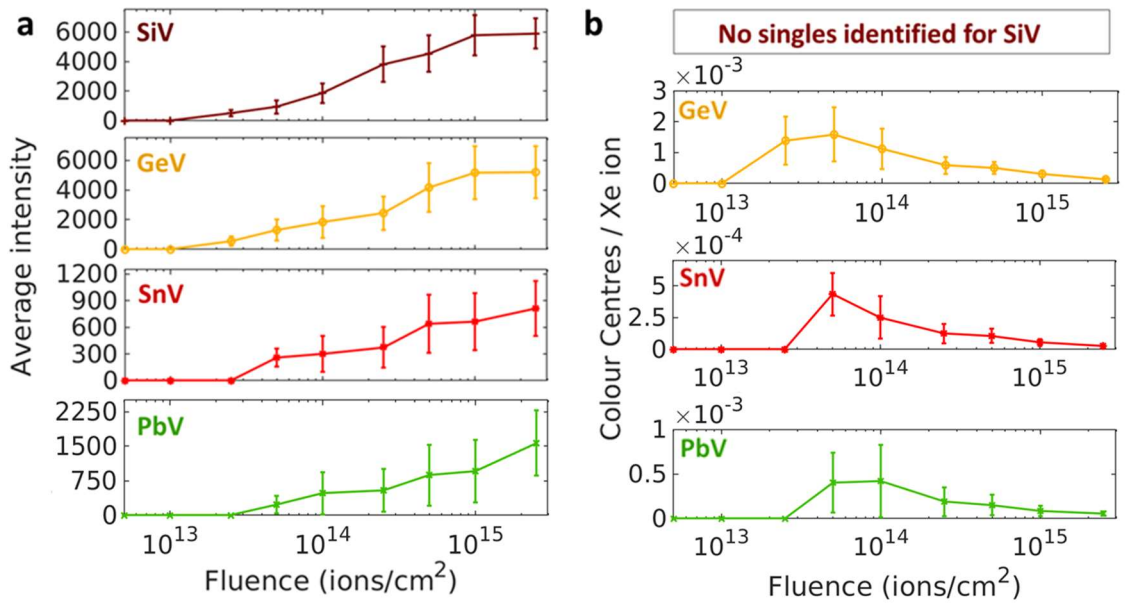

Figure 8.6. Determination of the creation yield for different colour centres versus Xe^+ fluence. a) The average pixel intensity was extracted from PL maps. Error bars indicate standard deviation of the average. b) Colour centres created per primary Xe ion, estimated by comparison of the average intensity to the intensity of identified single photon emitters. Error bars indicate standard deviation of the average pixel intensity.

8.3.4 Further Characterisation

To estimate the damage to the bulk diamond due to the implantation, we irradiated square areas (4 x 4) μm^2 with increasing fluences as shown in Figure 8.7(a). The primary Xe ion fluence of the first field was 1.6×10^{12} cm^{-2}, for each following field the fluence was doubled, with values of 3.1×10^{12} cm^{-2}, 6.2×10^{12} cm^{-2}, 1.3×10^{13} cm^{-2}, 2.5×10^{13} cm^{-2}, 5×10^{13}, 1×10^{14}, 2×10^{14}, 4×10^{14}, 8×10^{14}, 1.6×10^{15}, 3.2×10^{15} for fields 2–12, respectively. From the PL maps (Figure 8.7(b)) we observed, as the fluence increased, the PL intensity increased accordingly from fluence 1–4, followed by a decrease from 4–9 until the PL intensity increased again from 9–12. We note that this trend was observed for all elements. The initial increase can be attributed to a direct increase of the implanted species, leading to an increased concentration of luminescent colour centres. With further increase in fluence, we infer that degradation of the material leads to quenching of the PL signal. Note also that the thin film was exhausted during irradiation (removed by concurrent sputtering). The final increase in PL intensity is related to damage-related luminescence. We note that in comparison to spot irradiations, (discussed in 8.3.3) the

PL intensity decreased for an increasing fluence. This discrepancy is likely related to a higher degree of accumulated damage in larger irradiated regions, where the flux density is significantly higher as opposed to spot irradiations.

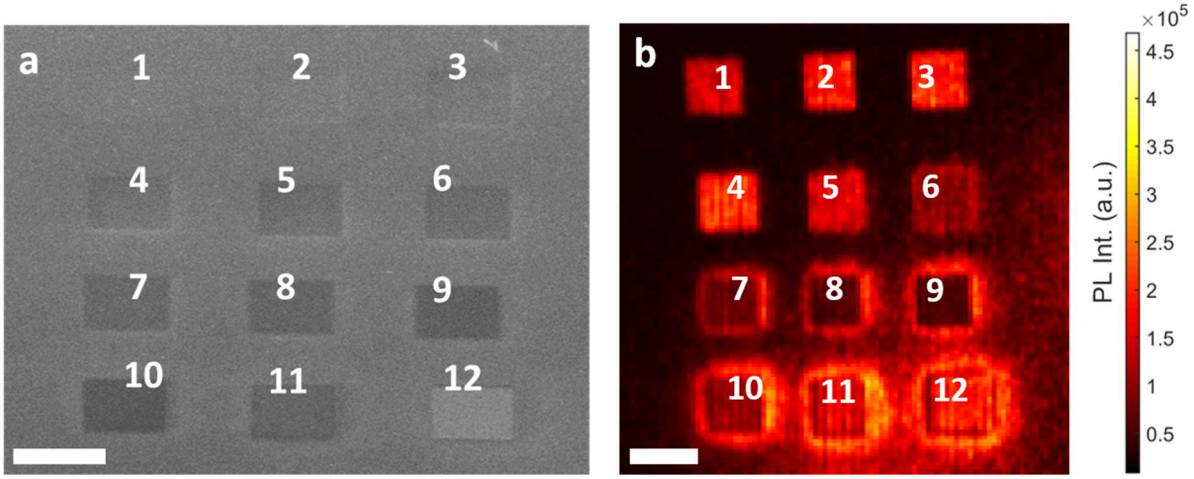

Figure 8.7. Square fluence series used to estimate the damage related to the technique. a) SEM image of a square series directly after irradiation (52° tilt). b) Representative PL map (Sn) of the fluence dependent series. Scale bars are 5 µm.

For the lower fluence range, despite the relatively high number of primary ions required for emitter creation, we observed that pronounced damage is virtually absent for low fluences in PL spectra (Figure 8.8) or AFM profiles (Figure 8.9). From the PL spectra we observe that for low fluence (spectrum 1) the background is lower in comparison to higher fluences, as seen particularly well in the case of Si, where essentially no PL is observed in the range 600 nm–700 nm. On the other hand, the diamond Raman line (1332 cm^{-1} / 572 nm and 2nd order 2664 cm^{-1} / 620 nm) is clearly present for all fluences and species. We also observe the emergence and increase of the G-band (1580 cm^{-1} / 581 nm) with increasing fluence. Whereas the former is indicative of the presence of diamond, the latter is direct evidence of damage in the form of sp^2- amorphisation. We note that even for high fluences (where the amount of sputtered material is significant), the diamond Raman line is present, as the implanted/ damaged layer is only present within a small section at the surface. At the highest fluence, clear formation of NV centres is observed (evidenced by the shapes of the PL spectra, resembling a ZPL at 637 nm with a broad phonon side band). We assume that despite their low natural concentration in the material, enough vacancies are formed ion beam to activate even the low concentration of nitrogen.

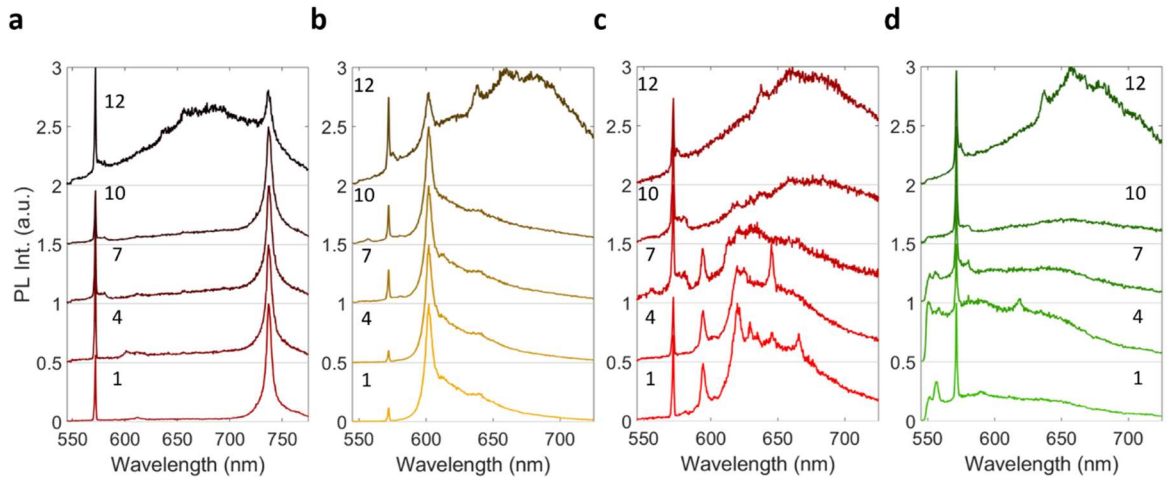

Figure 8.8. Spectra taken from the centres of the squares shown in Figure 8.7(b). The number indicates the fluence mentioned in the text. (a) Si, (b) Ge, (c) Sn and (d) Pb.

AFM scans and height profiles of the implanted areas are shown in Figure 8.9 for Si in (a) and (b), for Ge in (c) and (d), for Sn in (e) and (f), for Pb in (g) and (h), respectively. Regions 1–4 are non-discernible from the surrounding region for all species, as evident by a non-changing height profile in the AFM map. With further increasing of the fluence, in regions 5–8 the height profile distinctly increases above the height level of the surrounding area. This increase is evidence of swelling, due to implantation from primary Xe ions, as well as from the target layer. Moreover, we observe that the amount of swelling appears to increase with the mass of the implanted species, i.e. for Pb the highest swelling can be seen for fluence 10 with a change in height of ≅15 nm, whereas for lighter elements this value is lower, ≅ 5 nm for Sn (fluence 9), ≅3 nm for Ge (fluence 8), and ≅1 nm for Si (fluence 7). Note that the depth and PL cannot directly be correlated to the implantation profile as discussed below in Section 8.4.5. As we demonstrated throughout this work, atoms can be implanted directly from a thin film into the underlying bulk, and already-implanted species may be buried deeper by subsequent momentum transfer.

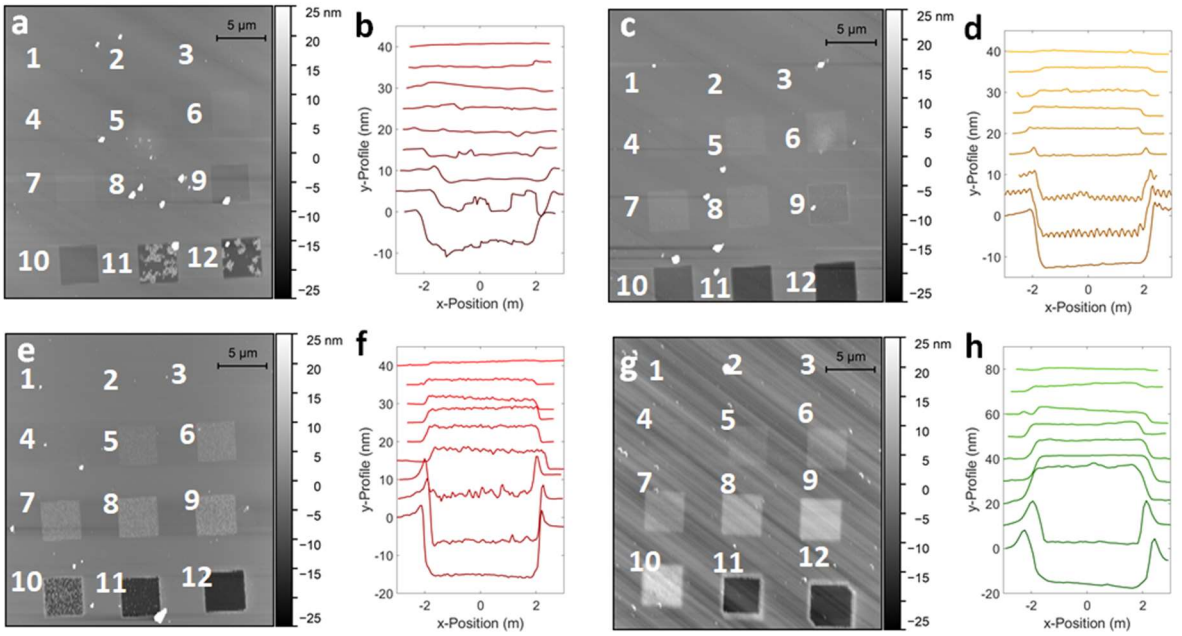

Figure 8.9. AFM scans and depth profiles of the implanted squares for Si (a) and (b), Ge (c) and (d), Sn (e) and (f), Pb (g) and (h). The numbers denote the aforementioned fluences. The depth profiles are offset in the y-direction for better visibility. For each graph, the first profile corresponds to fluence 4, the second to fluence 5 and so on. The diagonal streaks visible in the AFM maps are polishing marks of the as-purchased diamond.

8.3.5 Ion Beam Profile

Before we turn to a discussion about the spatial profile of the implanted species, we briefly discuss the ion beam profile, a decisive parameter for the precision of implanted species. To determine this parameter for our specific equipment under working conditions, we irradiated spots on a plain silicon substrate, as shown in Figure 8.10(a). The spot dwell time was increased column-wise from left to right, to identify the lowest dwell time that would yield identifiable distinctive spots (red outline). These spots were then averaged (Figure 8.10(b)) and fitted with a Gaussian function (Figure 8.10(c)). Figure 8.10(d), showing the suitability of this function to reproduce the shape of the beam. The fit yielded a standard deviation of σ = 36 nm, giving a FWHM of 85 nm as a rough estimate of the beam diameter. We emphasise that the comparison of spots from the lowest observable dwell time is valid as, the spot irradiations as discussed in Section 8.4.2 were done using a lower dwell time (<2.5 ms) than the spots shown here (12.5 ms). The range and straggle (defined below) in depth and radial direction for the implanted Ge atoms were determined using a code described elsewhere with a delta spike ion beam. We obtained the following values, depth range R_p = 0.12 nm (Equation 8.1), depth straggle

σ = 0.19 nm (Equation 8.2), radial range R_r= 6.04 nm (Equation 8.3), radial straggle: σ_R = 3.64 nm (Equation 8.4).[263,268] Here x_i, y_i, and z_i are the coordinates of the ith ion, N is the total number of ions simulated, and r_i is the radial distance of ion i from the centre of the beam. The given descriptions of the ion range corresponds to the average distance from point of impact, while the straggle corresponds to the width of the distribution.

$$R_p = \sum_i ({}^{x_i}/_N) \qquad (8.1)$$

$$\sigma = [\sum_i ({}^{x_i^2}/_N) - R_P^2)]^{1}/_2 = \langle(\Delta x_i)^2\rangle^{\frac{1}{2}} \qquad (8.2)$$

$$R_r = \sum_i {(y_i^2 + z_i^2)^{1/2}}/_N \qquad (8.3)$$

$$\sigma_r = [\sum_i {(y_i^2 + z_i^2)}/_N - R_r^2]^{1/2} = \langle(\Delta r_i)^2\rangle^{1/2} \qquad (8.4)$$

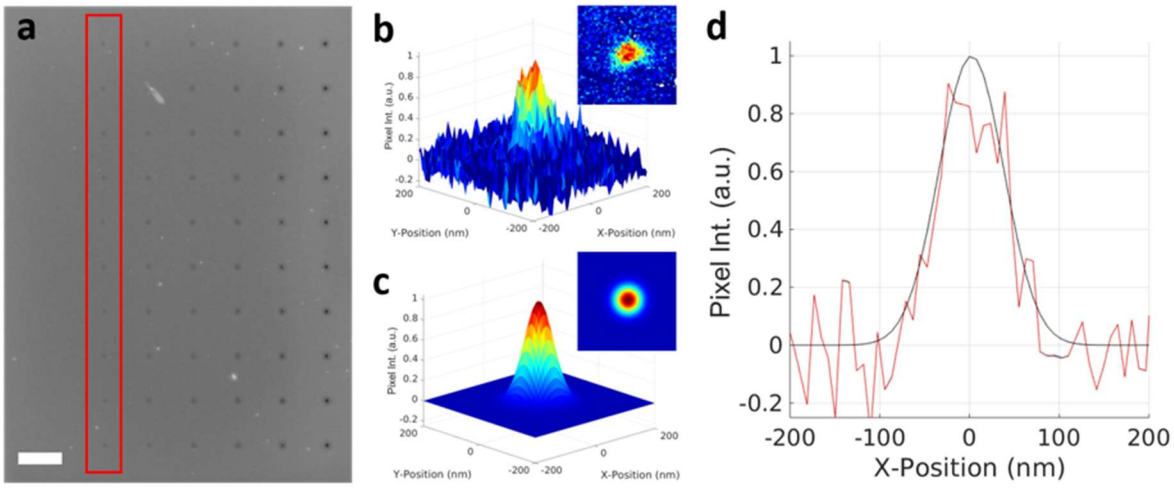

Figure 8.10 Determination of the beam diameter. a) A plain Si substrate was irradiated by spots with dwell times increasing column-wise from left to right. The scale bar corresponds to 1 µm. b) The normalised inverse pixel intensity of the average for the spots highlighted in (a). c) A Gaussian fit was used to approximate the ion beam shape. d) Direct comparison of measured and fitted beam shape.

From the simulation[262] of recoil doping of diamond from a 15-nm (amorphous) Ge film, we additionally extracted the angular distribution of the Ge atoms at the film-diamond interface. The distribution is shown in Figure 8.11. The abscissa represents the angle relative to the normal vector of the diamond surface (described in the inset). Values from 0° to 90° correspond

to Ge atoms that left the diamond and were scattered back into the Ge thin film, whilst entry angles from 90° to 180° correspond to atoms entering the diamond. The distribution peaks at ~140°, it is broad, asymmetric and lacks the forward-directionality of the incident Xe^+ beam.

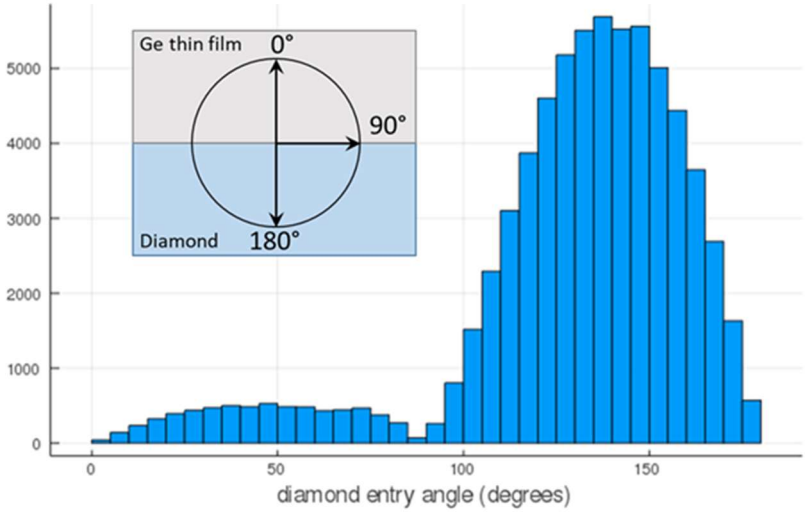

Figure 8.11. Angular distribution of Ge atoms trajectories as they cross the thin-film diamond interface. The orientation of the angle relative to the thin-film diamond interface is shown in the inset.

8.3.6 Spatial and Depth Profile

Next, we analyse the dopant depth profiles, as well as positional accuracy of the recoil implantation. Lateral precision was determined using PL maps of spot arrays of low fluence (5 × 10^{13} cm^{-2}) GeV ensembles. The ensemble locations were determined by local fits of the PL signal at the nominal implantation sites to 2D Gaussian functions and related to a fitted grid, as shown in Figure 8.12. In detail, we acquired a large area scan of a 10 x 10 spot array. To minimise the influence of setup-related aberrations (e.g. due to large map areas), as well as distortions due to drift (during the PL mapping), several subarrays of 4 x 4 points were considered. Horizontal and vertical lines were fitted through these points, with the constraint of equivalent slopes and equidistant line offsets for individual subarrays. Gridline intersections were then taken as the nominal implantation sites. Examples of the subarrays of 4 x 4 spots (fitted by a 2D Gaussian) are shown in Figure 8.12(a), (b), and (c). Some spots were counted twice, due to their presence in different subarrays, therefore yielding a total number higher than 100 in Figure 8.13(a). We note that the 4 top right and 4 bottom right points were excluded from the analysis, as we observed a systematic deviation compared to other sub grids, likely

due to a too large aberration and drift at the corner of the PL map. Therefore, the sub grid in Figure 8.12(c), only considered rows 6–9.

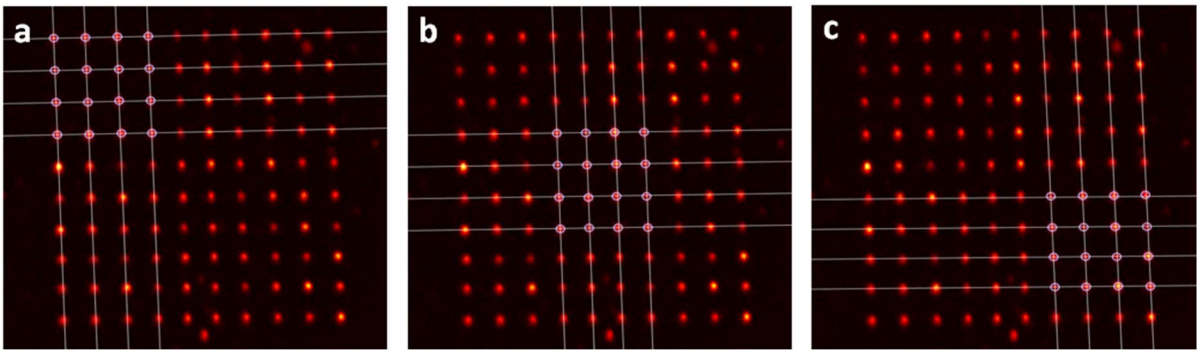

Figure 8.12. A large area scan (10 x 10 array), was analysed by fitting 8 sub grids (4 x 4). In (a), (b), and (c) three examples of subgrids are shown. We note that the subgrids in the most right section (right 4 columns) excluded the top and bottom 4 points, due to a systematic deviation.

The distance of the nominal position (i.e. the grid intersections) to the centre of the Gaussian fit was calculated, yielding a Rayleigh distribution of the relative ensemble position, as shown in Figure 8.13(a), whereas the extracted relative position did not show any skewness in the x or y direction (inset). A fit to a Rayleigh distribution, yields a mode of (44 ± 4) nm, representative of the implant-placement accuracy of the technique, whereas 4 nm is given by the uncertainty of the fit module (Matlab nonlinearfit). This value is better than that required for engineering of quantum emitters within photonic devices, e.g. in the high field region of a 2D photonic crystal cavity.[250]

To determine the ultimate lateral resolution of the technique, the above measure of accuracy should be considered in the context of the ion beam diameter, and that of straggle of atoms implanted, both discussed in Section 8.3.5. It should be noted that, in the case of the plasma FIB used here, the beam diameter is limited by the virtual source size and the ion beam focusing optics. [269] It can be improved in a number of ways, such as utilisation of a Gas Field Ionisation Source,[270] or a pierced cantilever with a hole that is smaller than the beam diameter[36] and thus reduces it in the plane of the target. Beyond the beam diameter, a fundamental limit on resolution is imposed by the radial range and straggle of the implanted atoms. To illustrate the magnitude of this effect, we simulated the spatial distribution of Ge implanted into diamond from a 15-nm film by an ideal 30 keV Xe^+ beam (i.e., a beam with a diameter of 0 nm). The results, detailed in Section 8.3.5, reveal that the radial range and straggle

are ~6 and 4 nm, respectively—a minor component of the measured accuracy of (44 ± 4) nm. The integration of FIB with a coincident high-resolution SEM in the same tool enables accurate and localised defect engineering at a particular target site (e.g. the high field region of a photonic resonator). We note that concurrent imaging using the SEM does not lead to any unwanted implantation or alteration of the diamond.

We now discuss the ultra-shallow implant depth profile. Monte Carlo modelling indicates that the technique yields dopants within the very top layer of the target surface, with a range and straggle of ~0.2 and 0.6 nm, respectively. In more detail, the Ge depth distribution, shown on a log-linear scale in Figure 8.12(b), reveals that over 90% of the implanted species are located within a depth of 1 nm, and the tail extends to ~10 nm. This is in good agreement with the measured value of (8 ± 2) nm that is discussed below. For comparison, the depth distribution of the co-implanted Xe is also shown in Figure 8.13(b). The Xe depth profile is much more uniform and not as concentrated as that of Ge within the top few nanometres of the diamond surface.

Experimentally, we cannot conclusively confirm by direct optical imaging that the emitters are ≤5 nm from the interface. Therefore, to verify the depths of the implanted emitters, we employed Electron Beam Induced Etching (EBIE) in an environmental SEM with H_2O vapour as the etch precursor.[7] EBIE allows us to locally remove the top material of the implanted areas, without damaging the material underneath. [189] During EBIE the electron beam locally induces a chemical reaction with the environmental species (H_2O) forming a volatile complex that either desorbs spontaneously or is removed by electron beam induced desorption. The rationale for the deployment of this technique is given by the fact that no further physical alteration of the implanted species is expected, as the etching process is driven chemically at the diamond surface. Using EBIE, a wedge-shaped feature was etched along a square implanted area (3.1×10^{12} cm^{-2}), as is shown schematically in Figure 8.13(c). In the following, we correlated the depth (AFM scan, shown in Figure 8.13(d)) to the local fluorescence intensity (PL map, shown in Figure 8.13(e)). Using three etched spots (white circles) as fiducial markers to correlate both maps, the average depth and PL profiles of the wedge were extracted (Figure 8.13(f)). In particular, we observe a PL emission maximum from a mean depth of less than ≃1.5 nm in the section—along the x-axis—between the 11 and 13 μm mark. We note that the initial increase observable in the PL line profile may be caused by an increase in surface roughness. This hypothesis is supported by the observation that the increase in PL correlates with spot-like features clearly discernible in the PL map in Figure 8.13(e).

Consequently, as the mean depth drops below 1.5 nm, the PL intensity decreases sharply to less than 50%, in the section along the x-axis, x ≅ 13–14 µm and down to 20% at about (5 ± 2) nm at x ≅ 15 µm. However, a residual PL signal is still present at a depth of (8 ± 2) nm, which is in good agreement with the tail of the simulated depth profile (Figure 8.13(b)). Specifically, at a depth of ≅8 nm, the number of Ge atoms drops below 1, which in combination with a conversion efficiency on the order of ≅1%[251] make it unlikely that colour centres are created beyond this depth. We note that the simulations do not account for channelling, which is likely insignificant, as indicated by an analysis of the simulated Ge atom momentum distribution at the film-diamond interface. Specifically, the momentum analysis shown discussed in 8.4.5 reveals that the strong forward-directionality of the Xe+ beam is not retained by the Ge atoms. Returning to Figure 8.12(f), the luminescence signal is restored at x ≅ 22 µm, corresponding to the end of the etched wedge. As one progresses further along the x-axis, the luminescence drops again to zero at the edge of the implanted area at x ≅ 25 µm.

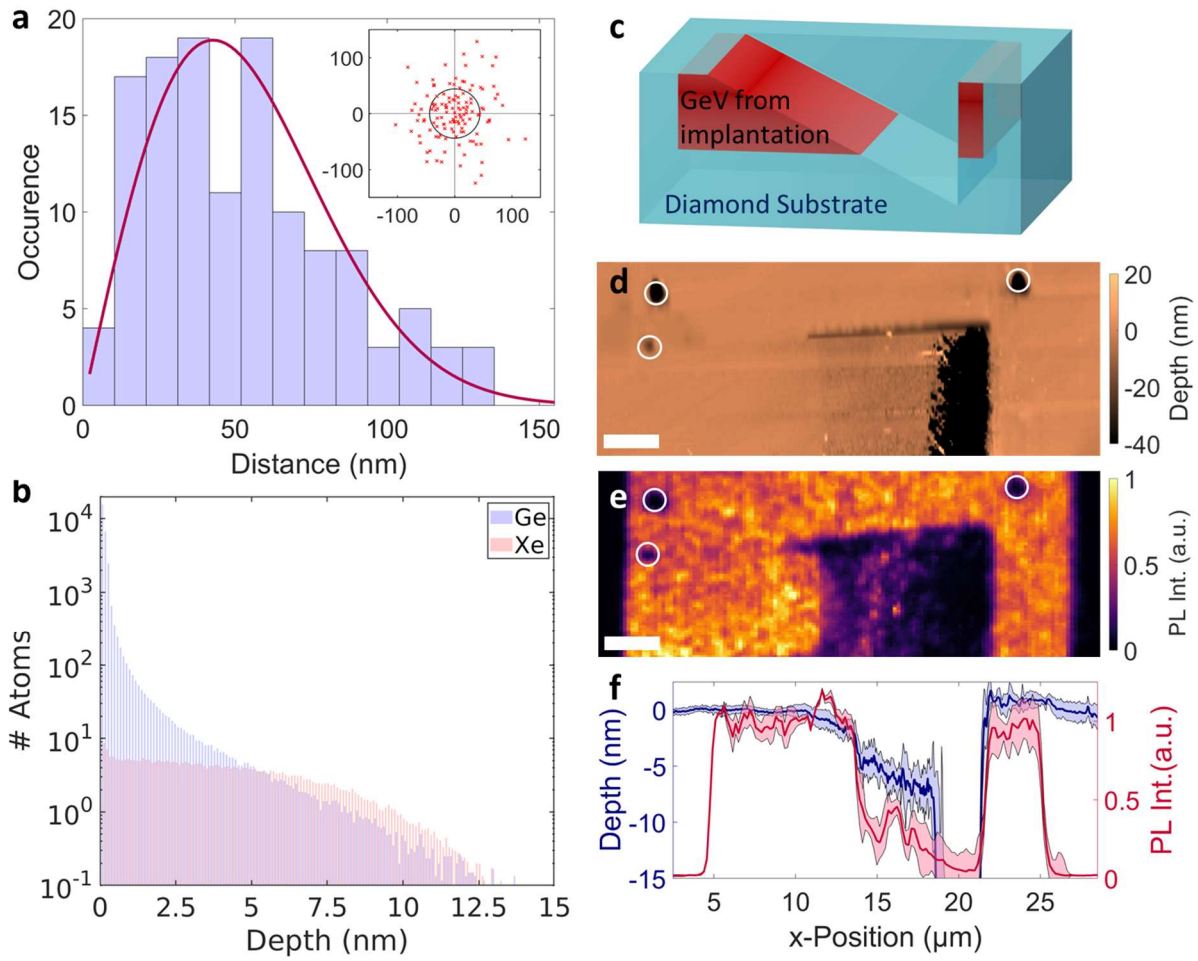

Figure 8.13. Spatial distribution of the dopants. (a) Distribution of the ensemble position (GeV) relative to the nominal implantation site, fitted by a Rayleigh function with a mode of (44 ± 4)

nm. The inset shows directly the relative ensemble position. (b) Monte Carlo simulations of the depth distribution of Ge in diamond from a Xe+ recoil-implantation process and of the co-implanted Xe. (c) Schematic of the wedge edge to access the implantation profile of an area with the implanted species. (d) AFM map of the wedge prepared by EBIE. (e) PL map of the same Ge-implanted area. The positions of both maps were correlated by the three marked spots. Scale bars in (d),(e) correspond to 2.5 µm. (f) Average profile of depth (blue) and PL (red) along the wedge feature. The shaded areas represent the standard deviation.

8.3.7 Implantation into other Systems and Restrictive Geometries

To demonstrate the versatility in material systems that may be achievable with this technique, we demonstrate the implantation of a Europium into SiO_2. We choose Europium to emphasise three key features. (1) Europium is heavier than Xe, which together with the Pb data in shows that the technique is applicable to most elements in the periodic table. (2) The implantation of Eu at low energies is challenging by conventional methods since it is difficult to form the stable negative Eu ions needed by some ion implanters. [271] (3) The integration of rare earth elements is generally sought after for integrated photonics. The choice of substrate was motivated for a later experiment for which it is similar. As per the previous experiments a thin film of 15 nm Europium was evaporated and irradiated with increasing fluences as follows, **1:** 1.6×10^{12} cm^{-2}, **2:** 2.4×10^{12} cm^{-2}, **3:** 3.6×10^{12} cm^{-2}, **4:** 5.4×10^{12} cm^{-2}, **5:** 8.1×10^{12} cm^{-2}, **6:** 1.2×10^{13} cm^{-2}, **7:** 1.8×10^{13} cm^{-2}, **8:** 2.7×10^{13} cm^{-2}, **9:** 4.1×10^{13} cm^{-2}, **10:** 6.2×10^{13} cm^{-2}, **11:** 9.2×10^{13} cm^{-2}, **12:** 1.4×10^{14} cm^{-2}, **13:** 2.1×10^{14} cm^{-2}, **14:** 3.1×10^{14} cm^{-2}, **15:** 4.7×10^{14} cm^{-2}. After irradiation, the Eu thin film was removed by dilute HCl at 50 ºC for 30 min. The sample was then studied in PL without further post processing. A PL map of the regions irradiated is shown in Figure 8.14(a). Spectra of the irradiated regions are shown in Figure 8.14(b). Notably, the emission is unchanged throughout the fluence series with a prominent peak at ~620 nm, corresponding to the $^5D_0 \rightarrow {}^7F_2$ transition of the Eu^{3+} ion. The fluence yielding the highest PL intensity was then used for the subsequent experiment, the implantation into an optical fibre core.

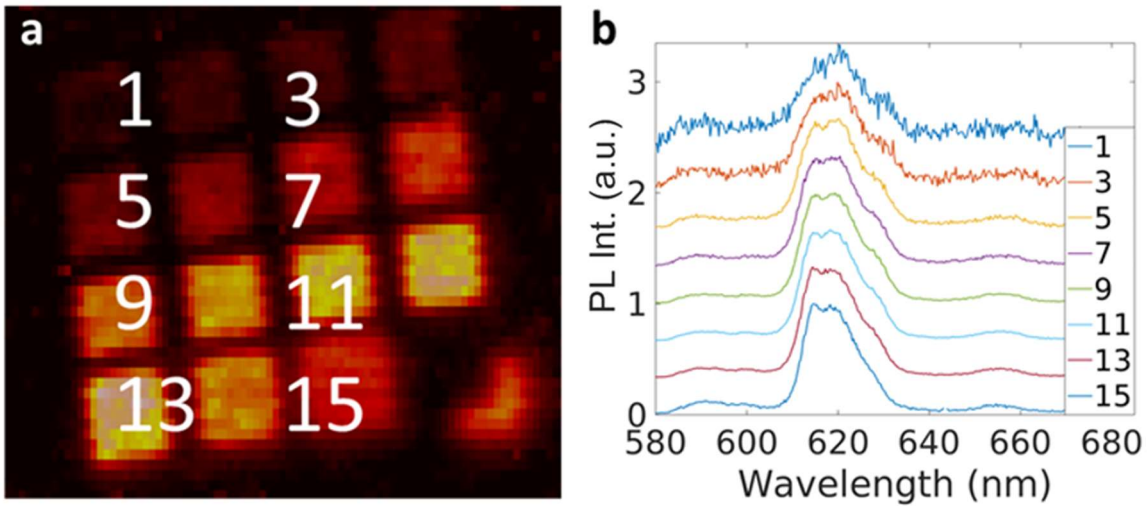

Figure 8.14. Implantation of Eu into SiO_2. a) Fluence series with values as mentioned in the main text. b) Normalised Spectra from the square regions.

Next, we demonstrate another key feature of the recoil implantation technique by implanting a specific site of a target that has a restrictive geometry. Most common implantation methods do not use FIBs, but instead achieve site-specificity using mask-based lithographic techniques that are often inapplicable to relatively small, high aspect ratio, non-planar samples. To showcase how this constraint is overcome in an extreme example, we implanted a rare earth element, Europium, into the end face of a commercial single-mode optical fibre (Figure 8.15(a)). Analogous to the above experiments, a thin film of Europium was deposited on the fibre end. The fibre was then mounted in the FIB-SEM dual beam microscope and the fibre core was identified using the SEM, as shown in Figure 8.15(b). The inset of Figure 8.15(b) is an optical image of the fibre, with the core lit up in blue by backflowing light from a torch through the opposite end of the fibre. The mark "x" is a fiducial marker used to correlate the optical and SEM images. To implant the Eu, the core of the fibre was irradiated using a Xe+ fluence of 4.1 $\times$ 10^{13} cm^{-2}, as determined beforehand. Subsequently, the thin film was removed and the implanted area was investigated by PL analysis. As shown in Figure 8.15(c), we observed the emission related to the $^5D_0 \rightarrow {}^7F_2$ transition of the Eu^{3+} ion centred at a wavelength of $\cong$620 nm. The emission is confined to the core of the fibre, as shown by the confocal PL map obtained by exciting the Eu^{3+} from the back of the fibre.

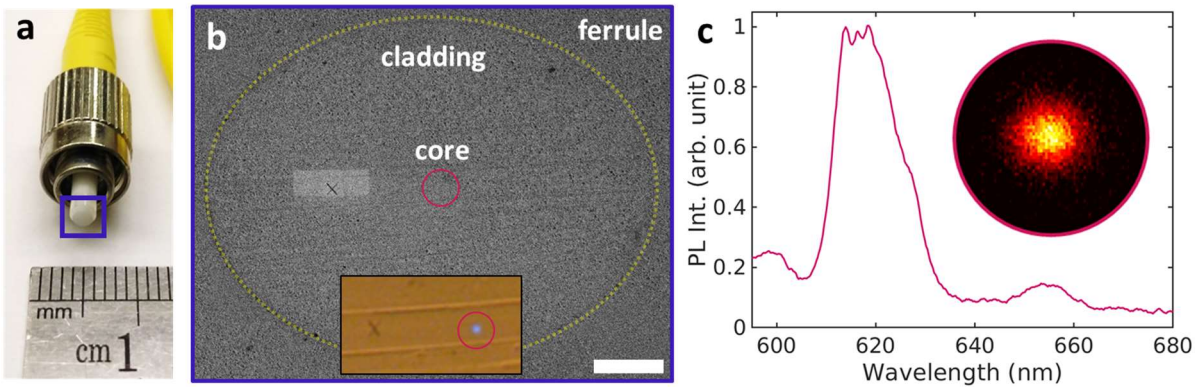

Figure 8.15. Implantation of rare earth ions into a commercial optical fibre. (a) Picture of the fibre used in this experiment. The end face is highlighted. (b) SEM image of the fibre end face during the implantation process. The yellow outline marks the boundary of the cladding to the ferrule, which was used to identify the core. The inset shows the core (back illuminated) relative to a correlation marker. The scale bar corresponds to 20 µm. (c) Emission of the implanted Eu3+, excited through the other fibre end (PL map shown as inset).

8.4 Conclusion

To conclude, we demonstrated versatile creation of shallow implants in a solid-sate host using recoil implantation. This is achieved by utilising momentum transfer from a Xe+ FIB to atoms of a thin target film deposited on top of a target of choice. In our work this is demonstrated by implantation from solid thin films deposited on the sample surface (diamond in our case). A compelling aspect of the technique is the ability to achieve ultrashallow implants. We used the method to create optically active, atom-like defects in diamond and demonstrated their formation within the top 6 nm from the surface. To demonstrate the applicability of the technique to non-conventional samples, we engineered rare earth elements directly in the core of a single mode optical fibre. Beyond the field of quantum technologies, the recoil implantation technique is appealing for shallow doping of single electron transistors,[272] deterministic direct writing of near surface dopants[273,274] or controlled introduction of magnetic elements for magnetism at the nanoscale. [275] Finally, one of the biggest advantages of this technique is the ability to engineer selected defects in atomically thin materials, which by definition requires ultra-shallow implants.

Chapter 9

Conclusion and Outlook

9.1 Summary

In this work the fabrication and integration of quantum emitters and photonic devices from hBN and diamond was demonstrated.

In more detail, in chapter 4, we have introduced a fabrication scheme that is suitable to achieve monolithic hBN cavities. In short, hBN flakes are exfoliated onto a trenched Silicon substrate. Subsequently, the substrate is coated with a tungsten thin film. Then EBL is used to define a mask, outlining the design of the desired cavity. The mask is transferred into the underlying tungsten film and hBN by RIE. However, it was found that RIE alone was not sufficient to completely etch through a 300 nm thick hBN layer and produce vertical side walls. Therefore, EBIE was deployed as an additional etching step with the tungsten layer as a hard mask. After fabrication, Q-factors of up to 1500 were measured. It was found that the fabrication steps also created single photon emitters in the processed regions as compared to unprocessed regions. Yet, the ZPL of the created emitters did not follow a clear distribution, which hindered the spectral matching of cavity resonances with emitters at that point. However, we showed that, if a method could be found to create emitters with a distinct ZPL, then cavities with a resonance close to the emission wavelength could be tuned by direct EBIE. This tuning method directly utilises mask free etching with an electron beam, and allows for a reproducible tuning of the cavity resonance.

In chapter 5, we have detailed the fabrication method further and expanded the demonstration to a set of common photonic devices, such as microrings, waveguides, and bulls eye gratings. In this part of the thesis a close look on the fabrication method reveals several artefacts that might occur during device fabrication and effective measures are described to avoid such fabrication artefacts during the combined, EBL-RIE-EBIE process.

In chapter 6, the integration of CVD grown hBN with Silicon Nitride nanobeam cavities is described. Here we exploit the observation that the ZPL of emitters found in CVD hBN display clear emission around 585 nm. We successfully, demonstrate the integration of such quantum

emitters into Silicon Nitride Cavities and achieve PL enhancements of up to 9. Yet, a full determination of the Purcell factor was not possible due to the emitter instabilities, which will require further work as discussed below.

In chapter 7, an alternate route for hybrid integration of quantum emitters from fluorescent particles is introduced. Particularly, we demonstrate a design that achieves a higher mode overlap than usual and achieves an ultrasmall mode volume on the order of 0.02 $(\lambda/n)^3$. To demonstrate the functionality of the designed cavity, upconversion nanoparticles were dispersed. This facilitated a background free PL analysis, which showed a pure 20-fold luminescence enhancement for a nanoparticle placed inside a pocket. For the shown device we derived a Purcell factor of at least 60 at room temperature, which to the best of my knowledge is among the highest achieved Purcell factors for dielectric cavities at room temperature.

In chapter 8 we introduced a method for the site specific creation of quantum emitters using a standard Focused Ion Beam with an arbitrary ion source. Specifically, the creation of all group IV colour centres in diamond was shown, for which even single photon emitter were demonstrated. By means of PL and AFM analysis we detailed the characteristics of the underlying technique, and showed that a near damage free implantation on par with standard ion implantation is possible. Beyond that this technique is versatile to all elements that can be deposited as a thin film onto a substrate and we could also demonstrate the creation of Rare Earth Ion emitters in SiO_2. Finally, we showcased a main advantage over standard ion implantation, which was the mask free site specific creation of luminescent colour centres in a commercial optical fibre.

9.2 Future Work

Here, the outlook for future experiments are discussed. These suggestions can be seen as the logical extrapolation of the main findings in this work and will hopefully help to stimulate new ideas for related projects.

For monolithic hBN devices, despite initial success in the fabrication and the capability to tune the resonance frequency of single devices by EBIE, the work suffered from the somewhat unpredictable emission wavelength of the created single photon emitter after the fabrication process. Yet, recent findings on the nature of hBN defects with emission at 585 nm, suggest the involvement of Carbon in the defect. Hence, future effort should be put towards the predictable and site specific creation of hBN single emitter. Certainly, the same route was

successful for diamond colour centres, where the integration of SiV colour centres by ion beam implantation has enabled a plethora of ground breaking works for cavity integrated colour centres. This topic is indeed well combinable with the work on site specific generation of quantum emitter through recoil implantation. Another factor that may limit monolithic hBN devices thus far is the availability of large scale high quality hBN layers with sufficient thickness. In this case recent efforts of wafer scale growth for single crystal hBN may alleviate this obstacle. Beyond single photon emitters with emission at 600 nm, future works should focus on the VB^- defect, a defect that has been recently identified exhibiting ODMR and that can be simply generated by ion beam irradiation. Particularly, for this emitter a suitable monolithic resonator geometry with a broad resonance and low mode volume is required. This will enhance the relatively broad emission of this particular defect, which may facilitate the identification of single VB^- emitter. The developed fabrication methods certainly build the basis for the work in this direction.

For hybrid integration methods utilising SiN as the carrier platform, the next step would be the stabilisation of SPEs that can are obtained from CVD grown hBN. Indeed this was the major obstacle encountered in the efforts to couple emitters to cavity resonances. Towards this goal, two steps have to be taken, (1) the hBN quality by CVD growth has to be increased, which will require experiments on different substrate types and under different growth conditions. Recent works by Mendelson et al. certainly seem promising, where it was found that hBN emitter, grown by CVD on nickel exhibit a higher stability as those grown on copper.[276] (2) As a subsequent step, it will be required to integrate the hBN film within the SiN platform. This may be achievable for example by LPCVD growth of Silicon Nitride (or other high refractive index dielectrics) on top of hBN on SiN. By this means hBN emitter will be more suitable shielded from the environment and thus should be less susceptible to charge transfer and field fluctuations in their environment, for example by physisorption of gas molecules on the surface. In addition the integration of hBN in a sandwich structure will achieve higher field overlaps in photonic devices, which will increase their efficiency.

The next step for the deployment of photonic nanobeam cavities with pockets will be the integration of particles that contain single photon emitters. Particularly, for this effort a more precise method for integration of the particle will be required, such as the application of a deterministic pick and place technique. This will then enable the observation of Purcell enhancement in cavities with ultrasmall mode volume.

Last, but not least, the next step for the recoil implantation method, will be towards a reduction of the related damage. Especially, diamond overgrowth may be applicable, which recently demonstrated the suppression of extraneous lines related to the SnV colour centre. In the following the integration with photonic and plasmonic cavities may be appealing, due to the high degree of spatial precision that can be achieved. Beyond that, emitters generated by this technique have great potential for interfacing with other material platforms, due to their close proximity to the surface. This can be realised in either of two ways, fabrication of photonic structures directly on top of the diamond, for example through material deposition, as recently demonstrated by TiO_2,[277] or by combining intrinsic material properties that may give rise to new phenomena. Related to the latter is also the potential to use near surface emitters as sensors, which could for example be utilised to locally determine physical quantities such as temperature, magnetic or electric fields.

Bibliography

[1] Kim, S. *et al.* Photonic crystal cavities from hexagonal boron nitride. *Nat. Commun.* **9**, 2623 (2018).

[2] Shandilya, P. K. *et al.* Hexagonal Boron Nitride Cavity Optomechanics. *Nano Lett.* **19**, 1343-1350 (2019).

[3] Fröch, J. E., Hwang, Y., Kim, S., Aharonovich, I. & Toth, M. Photonic Nanostructures from Hexagonal Boron Nitride. *Advanced Optical Materials* **7**, 1801344 (2019).

[4] Fröch, J. E. *et al.* Photonic Nanobeam Cavities with Nanopockets for Efficient Integration of Fluorescent Nanoparticles. *Nano Lett.* **20**, 2784-2790 (2020).

[5] Fröch, J. E. *et al.* Coupling Hexagonal Boron Nitride Quantum Emitters to Photonic Crystal Cavities. *ACS Nano* **14**, 7085-7091 (2020).

[6] Fröch, J. E. *et al.* Knock-on doping: A universal method to direct-write dopants in a solid state host. *arXiv e-prints*, arXiv:2001.06985 (2020).

[7] Bishop, J. *et al.* Deterministic Nanopatterning of Diamond Using Electron Beams. *ACS Nano* **12**, 2873-2882 (2018).

[8] Elbadawi, C., Fröch, J. E., Aharonovich, I., Toth, M. & Lobo, C. J. One-Step Nanoscale Patterning of Silver Nanowire–Nitride Heterostructures Using Substrate-Assisted Chemical Etching. *The Journal of Physical Chemistry C* **123**, 945-949 (2019).

[9] Chen, D. *et al.* Optical Gating of Resonance Fluorescence from a Single Germanium Vacancy Color Center in Diamond. *Phys. Rev. Lett.* **123**, 033602 (2019).

[10] Kim, S. *et al.* Second-harmonic generation in multilayer hexagonal boron nitride flakes. *Opt. Lett.* **44**, 5792-5795 (2019).

[11] Regan, B. *et al.* Plastic Deformation of Single-Crystal Diamond Nanopillars. *Advanced Materials* **32**, 1906458 (2020).

[12] Bernhardt, N. *et al.* Quasi-BIC Resonant Enhancement of Second-Harmonic Generation in WS2 Monolayers. *Nano Lett.* **20**, 5309-5314 (2020).

[13] Kianinia, M., White, S., Fröch, J. E., Bradac, C. & Aharonovich, I. Generation of Spin Defects in Hexagonal Boron Nitride. *ACS Photonics* **7**, 2147-2152 (2020).

[14] Mu, Z. *et al.* Coherent Manipulation with Resonant Excitation and Single Emitter Creation of Nitrogen Vacancy Centers in 4H Silicon Carbide. *Nano Lett.* **20**, 6142-6147 (2020).

[15] Mu, Z. *et al.* Observation of Binary Spectral Jumps in Color Centers in Diamond. *Advanced Optical Materials* **n/a**, 2000495 (2020).

[16] Rohdenburg, M., Fröch, J. E., Martinović, P., Lobo, C. J. & Swiderek, P. Combined Ammonia and Electron Processing of a Carbon-Rich Ruthenium Nanomaterial Fabricated by Electron-Induced Deposition. *Micromachines* **11** (2020).

[17] Schematic of a Quantum Dot. https://warwick.ac.uk/fac/sci/physics/current/postgraduate/regs/mpagswarwick/ex5/lds/qd/qds.jpg

(2020).

[18] Anders, S. *et al.* Bimodal size distribution of self-assembled In_xGa_1-xAs quantum dots. *Physical Review B* **66**, 125309 (2002).

[19] Aharonovich, I., Englund, D. & Toth, M. Solid-state single-photon emitters. *Nat. Photonics* **10**, 631-641 (2016).

[20] He, X. *et al.* Carbon nanotubes as emerging quantum-light sources. *Nature Materials* (2018).

[21] Palacios-Berraquero, C. *et al.* Large-scale quantum-emitter arrays in atomically thin semiconductors. *Nat. Commun.* **8**, 15093 (2017).

[22] Schirhagl, R., Chang, K., Loretz, M. & Degen, C. L. Nitrogen-Vacancy Centers in Diamond: Nanoscale Sensors for Physics and Biology. *Annu. Rev. Phys. Chem.* **65**, 83-105 (2014).

[23] Bradac, C., Gao, W., Forneris, J., Trusheim, M. E. & Aharonovich, I. Quantum nanophotonics with group IV defects in diamond. *Nat. Commun.* **10**, 5625 (2019).

[24] Tran, T. T., Bray, K., Ford, M. J., Toth, M. & Aharonovich, I. Quantum emission from hexagonal boron nitride monolayers. *Nat. Nanotechnol.* **11**, 37-41 (2016).

[25] Bourrellier, R. *et al.* Bright UV Single Photon Emission at Point Defects in h-BN. *Nano Lett.* **16**, 4317-4321 (2016).

[26] Tran, T. T. *et al.* Robust Multicolor Single Photon Emission from Point Defects in Hexagonal Boron Nitride. *ACS Nano* **10**, 7331-7338 (2016).

[27] Camphausen, R. *et al.* Observation of near-infrared sub-Poissonian photon emission in hexagonal boron nitride at room temperature. *APL Photonics* **5**, 076103 (2020).

[28] Jungwirth, N. R. *et al.* Temperature Dependence of Wavelength Selectable Zero-Phonon Emission from Single Defects in Hexagonal Boron Nitride. *Nano Lett.* **16**, 6052-6057 (2016).

[29] Proscia, N. V. *et al.* Near-deterministic activation of room temperature quantum emitters in hexagonal boron nitride. *Optica* **5**, 1128 (2018).

[30] Mendelson, N. *et al.* Engineering and Tuning of Quantum Emitters in Few-Layer Hexagonal Boron Nitride. *ACS Nano* **13**, 3132-3140 (2019).

[31] Mendelson, N. *et al.* Identifying Carbon as the Source of Visible Single Photon Emission from Hexagonal Boron Nitride. *arXiv e-prints*, arXiv:2003.00949 (2020).

[32] Johnson, S. G. & Joannopoulos, J. D. Three-dimensionally periodic dielectric layered structure with omnidirectional photonic band gap. *Appl. Phys. Lett.* **77**, 3490-3492 (2000).

[33] Englund, D., Fushman, I. & Vuckovic, J. General recipe for designing photonic crystal cavities. *Opt. Express* **13**, 5961-5975 (2005).

[34] Vuckovic, J. Quantum optics and cavity QED with quantum dots in photonic crystals. *arXiv e-prints*, arXiv:1402.2541 (2014).

[35] Toyli, D. M., Weis, C. D., Fuchs, G. D., Schenkel, T. & Awschalom, D. D. Chip-Scale Nanofabrication of Single Spins and Spin Arrays in Diamond. *Nano Lett.* **10**, 3168-3172 (2010).

[36] Pezzagna, S. *et al.* Nanoscale Engineering and Optical Addressing of Single Spins in Diamond. *Small* **6**, 2117-2121 (2010).

[37] Groot-Berning, K. *et al.* Deterministic Single-Ion Implantation of Rare-Earth Ions for Nanometer-Resolution Color-Center Generation. *Phys. Rev. Lett.* **123**, 106802 (2019).

[38] Schröder, T. *et al.* Scalable focused ion beam creation of nearly lifetime-limited single quantum emitters in diamond nanostructures. *Nat. Commun.* **8**, 15376 (2017).

[39] MacFarlane, A. G. J., Dowling, J. P. & Milburn, G. J. Quantum technology: the second quantum revolution. *Philosophical Transactions of the Royal Society of London. Series A: Mathematical, Physical and Engineering Sciences* **361**, 1655-1674 (2003).

[40] Yu, Y. *et al.* Entanglement of two quantum memories via fibres over dozens of kilometres. *Nature* **578**, 240-245 (2020).

[41] Yin, J. *et al.* Satellite-based entanglement distribution over 1200 kilometers. *Science* **356**, 1140-1144 (2017).

[42] Zhong, H.-S. *et al.* Quantum computational advantage using photons. *Science* **370**, 1460 (2020).

[43] O'Brien, J. L., Furusawa, A. & Vuckovic, J. Photonic quantum technologies. *Nat. Photonics* **3**, 687-695 (2009).

[44] Fox, M. Quantum Optics: An Introduction. *Quantum optics* **67**, 441-441 (2006).

[45] Bommer, A. & Becher, C. New insights into nonclassical light emission from defects in multi-layer hexagonal boron nitride. *Nanophotonics* **8**, 2041-2048 (2019).

[46] Couteau, C. Spontaneous parametric down-conversion. *Contemporary Physics* **59**, 291-304 (2018).

[47] Steinbrecher, G. R., Olson, J. P., Englund, D. & Carolan, J. Quantum optical neural networks. *npj Quantum Information* **5**, 60 (2019).

[48] Carolan, J. *et al.* Variational quantum unsampling on a quantum photonic processor. *Nature Physics* **16**, 322-327 (2020).

[49] García-Ripoll, J. J., Zoller, P. & Cirac, J. I. Quantum information processing with cold atoms and trapped ions. *Journal of Physics B: Atomic, Molecular and Optical Physics* **38**, S567-S578 (2005).

[50] Niffenegger, R. J. *et al.* Integrated multi-wavelength control of an ion qubit. *Nature* **586**, 538-542 (2020).

[51] Samutpraphoot, P. *et al.* Strong Coupling of Two Individually Controlled Atoms via a Nanophotonic Cavity. *Phys. Rev. Lett.* **124**, 063602 (2020).

[52] Goban, A. *et al.* Atom–light interactions in photonic crystals. *Nat. Commun.* **5**, 3808 (2014).

[53] Awschalom, D. D., Hanson, R., Wrachtrup, J. & Zhou, B. B. Quantum technologies with optically interfaced solid-state spins. *Nat. Photonics* **12**, 516-527 (2018).

[54] Atatüre, M., Englund, D., Vamivakas, N., Lee, S.-Y. & Wrachtrup, J. Material platforms for spin-based photonic quantum technologies. *Nat. Rev. Mater.* **3**, 38-51 (2018).

[55] Lee, C. B., Audrius, A., Annemarie, L. E. & Kai-Mei, C. F. Quantum defects by design. *Nanophotonics* **8**, 1867-1888 (2019).

[56] Toth, M. & Aharonovich, I. Single Photon Sources in Atomically Thin Materials. *Annu. Rev. Phys. Chem.* **70**, 123-142 (2019).

[57] Hepp, S., Jetter, M., Portalupi, S. L. & Michler, P. Semiconductor Quantum Dots for Integrated Quantum Photonics. *Advanced Quantum Technologies* **2**, 1900020 (2019).

[58] Aharonovich, I. & Neu, E. Diamond Nanophotonics. *Advanced Optical Materials* **2**, 911-928 (2014).

[59] Lohrmann, A., Johnson, B. C., McCallum, J. C. & Castelletto, S. A review on single photon sources in silicon carbide. *Reports on Progress in Physics* **80**, 034502 (2017).

[60] Tian, Z. & Philippe, G. Emerging rare-earth doped material platforms for quantum nanophotonics. *Nanophotonics* **8**, 2003-2015 (2019).

[61] Tonndorf, P. *et al.* Single-photon emission from localized excitons in an atomically thin semiconductor. *Optica* **2**, 347-352 (2015).

[62] Chakraborty, C., Kinnischtzke, L., Goodfellow, K. M., Beams, R. & Vamivakas, A. N. Voltage-controlled quantum light from an atomically thin semiconductor. *Nat Nano* **10**, 507-511 (2015).

[63] Srivastava, A. *et al.* Optically active quantum dots in monolayer WSe2. *Nat Nano* **10**, 491-496 (2015).

[64] He, Y.-M. *et al.* Single quantum emitters in monolayer semiconductors. *Nat Nano* **10**, 497-502 (2015).

[65] Koperski, M. *et al.* Single photon emitters in exfoliated WSe2 structures. *Nat. Nanotechnol.* **10**, 503-506 (2015).

[66] Chejanovsky, N. *et al.* Quantum Light in Curved Low Dimensional Hexagonal Boron Nitride Systems. *Sci. Rep.* **7**, 14758 (2017).

[67] Klein, J. *et al.* Site-selectively generated photon emitters in monolayer MoS2 via local helium ion irradiation. *Nat. Commun.* **10**, 2755 (2019).

[68] Thomas, S. & Senellart, P. The race for the ideal single-photon source is on. *Nat. Nanotechnol.* **16**, 367-368 (2021).

[69] Reimer, M. E. & Cher, C. The quest for a perfect single-photon source. *Nat. Photonics* **13**, 734-736 (2019).

[70] Morfa, A. J. *et al.* Single-Photon Emission and Quantum Characterization of Zinc Oxide Defects. *Nano Lett.* **12**, 949-954 (2012).

[71] Stewart, C. *et al.* Quantum emission from localized defects in zinc sulfide. *Opt. Lett.* **44**, 4873-4876 (2019).

[72] Berhane, A. M. *et al.* Bright Room-Temperature Single-Photon Emission from Defects in Gallium Nitride. *Advanced Materials* **29**, 1605092 (2017).

[73] Xue, Y. *et al.* Single-Photon Emission from Point Defects in Aluminum Nitride Films. *The Journal of Physical Chemistry Letters* **11**, 2689-2694 (2020).

[74] Park, Y.-S., Guo, S., Makarov, N. S. & Klimov, V. I. Room Temperature Single-Photon Emission from Individual Perovskite Quantum Dots. *ACS Nano* **9**, 10386-10393 (2015).

[75] Moerner, W. E. Single-photon sources based on single molecules in solids. *New Journal of Physics* **6**, 88-88 (2004).

[76] Doherty, M. W. *et al.* The nitrogen-vacancy colour centre in diamond. *Physics Reports* **528**, 1-45 (2013).

[77] Shanley, T. W., Martin, A. A., Aharonovich, I. & Toth, M. Localized chemical switching of the charge state of nitrogen-vacancy luminescence centers in diamond. *Appl. Phys. Lett.* **105**, 063103 (2014).

[78] Iakoubovskii, K., Adriaenssens, G. J. & Nesladek, M. Photochromism of vacancy-related centres in diamond. *Journal of Physics-Condensed Matter* **12**, 189-199 (2000).

[79] Fu, K. M. C., Santori, C., Barclay, P. E. & Beausoleil, R. G. Conversion of neutral nitrogen-vacancy centers to negatively charged nitrogen-vacancy centers through selective oxidation. *Appl. Phys. Lett.* **96**, 121907 (2010).

[80] Aslam, N., Waldherr, G., Neumann, P., Jelezko, F. & Wrachtrup, J. Photo-induced ionization dynamics of the nitrogen vacancy defect in diamond investigated by single-shot charge state detection. *New Journal of Physics* **15**, 013064 (2013).

[81] Beha, K. *et al.* Diamond nanophotonics. *Beilstein Journal of Nanotechnology* **3**, 895-908 (2012).

[82] Faraon, A., Santori, C., Huang, Z. H., Acosta, V. M. & Beausoleil, R. G. Coupling of Nitrogen-Vacancy Centers to Photonic Crystal Cavities in Monocrystalline Diamond. *Phys. Rev. Lett.* **109** (2012).

[83] Faraon, A., Barclay, P. E., Santori, C., Fu, K. M. C. & Beausoleil, R. G. Resonant enhancement of the zero-phonon emission from a colour centre in a diamond cavity. *Nat. Photonics* **5**, 301-305 (2011).

[84] Barclay, P. E., Fu, K.-M. C., Santori, C., Faraon, A. & Beausoleil, R. G. Hybrid Nanocavity Resonant Enhancement of Color Center Emission in Diamond. *Phys. Rev. X* **1**, 011007 (2011).

[85] Zhao, H.-Q., Fujiwara, M. & Takeuchi, S. Suppression of fluorescence phonon sideband from nitrogen vacancy centers in diamond nanocrystals by substrate effect. *Opt. Express* **20**, 15628-15635 (2012).

[86] Neu, E. *et al.* Single photon emission from silicon-vacancy centres in CVD-nano-diamonds on iridium *New Journal of Physics* **13**, 025012 (2011).

[87] Sipahigil, A. *et al.* Indistinguishable Photons from Separated Silicon-Vacancy Centers in Diamond. *Phys. Rev. Lett.* **113**, 113602 (2014).

[88] Sipahigil, A. *et al.* An integrated diamond nanophotonics platform for quantum optical networks. *Science* **354**, 847 (2016).

[89] Evans, R. E. *et al.* Photon-mediated interactions between quantum emitters in a diamond nanocavity. *Science* **362**, 662-665 (2018).

[90] Iwasaki, T. *et al.* Germanium-Vacancy Single Color Centers in Diamond. *Sci. Rep.* **5**, 12882 (2015).

[91] Tchernij, S. D. *et al.* Single-Photon-Emitting Optical Centers in Diamond Fabricated upon Sn Implantation. *ACS Photonics* **4**, 2580-2586 (2017).

[92] Iwasaki, T. *et al.* Tin-Vacancy Quantum Emitters in Diamond. *Phys. Rev. Lett.* **119**, 253601 (2017).

[93] Trusheim, M. E. *et al.* Lead-related quantum emitters in diamond. *Physical Review B* **99**, 075430 (2019).

[94] Ditalia Tchernij, S. *et al.* Single-Photon Emitters in Lead-Implanted Single-Crystal Diamond. *ACS Photonics* **5**, 4864-4871 (2018).

[95] Minh, N. *et al.* Photodynamics and quantum efficiency of germanium vacancy color centers in diamond. *Advanced Photonics* **1**, 1-7 (2019).

[96] Siyushev, P. *et al.* Optical and microwave control of germanium-vacancy center spins in diamond. *Physical Review B* **96**, 081201 (2017).

[97] Rugar, A. E. *et al.* Generation of Tin-Vacancy Centers in Diamond via Shallow Ion Implantation and Subsequent Diamond Overgrowth. *Nano Lett.* **20**, 1614-1619 (2020).

[98] Trusheim, M. E. *et al.* Transform-Limited Photons From a Coherent Tin-Vacancy Spin in Diamond. *Phys. Rev. Lett.* **124**, 023602 (2020).

[99] Breitweiser, S. A. *et al.* Efficient Optical Quantification of Heterogeneous Emitter Ensembles. *ACS Photonics* **7**, 288-295 (2020).

[100] Ngoc My Duong, H. *et al.* Effects of High-Energy Electron Irradiation on Quantum Emitters in Hexagonal Boron Nitride. *ACS Applied Materials & Interfaces* (2018).

[101] Choi, S. *et al.* Engineering and Localization of Quantum Emitters in Large Hexagonal Boron Nitride Layers. *ACS Applied Materials & Interfaces* **8**, 29642-29648 (2016).

[102] Ziegler, J. *et al.* Deterministic Quantum Emitter Formation in Hexagonal Boron Nitride via Controlled Edge Creation. *Nano Lett.* **19**, 2121-2127 (2019).

[103] Hou, S. *et al.* Localized emission from laser-irradiated defects in 2D hexagonal boron nitride. *2D Materials* **5**, 015010 (2017).

[104] Xu, Z.-Q. *et al.* Single photon emission from plasma treated 2D hexagonal boron nitride. *Nanoscale* **10**, 7957-7965 (2018).

[105] Vogl, T., Campbell, G., Buchler, B. C., Lu, Y. & Lam, P. K. Fabrication and Deterministic Transfer of High-Quality Quantum Emitters in Hexagonal Boron Nitride. *ACS Photonics* **5**, 2305-2312 (2018).

[106] Chejanovsky, N. *et al.* Structural Attributes and Photodynamics of Visible Spectrum Quantum Emitters in Hexagonal Boron Nitride. *Nano Lett.* **16**, 7037-7045 (2016).

[107] Gottscholl, A. *et al.* Initialization and read-out of intrinsic spin defects in a van der Waals crystal at room temperature. *Nature Materials* **19**, 540-545 (2020).

[108] Tawfik, S. A. *et al.* First-principles investigation of quantum emission from hBN defects. *Nanoscale* **9**, 13575-13582 (2017).

[109] Yablonovitch, E. INHIBITED SPONTANEOUS EMISSION IN SOLID-STATE PHYSICS AND ELECTRONICS. *Phys. Rev. Lett.* **58**, 2059-2062 (1987).

[110] John, S. Strong localization of photons in certain disordered dielectric superlattices. *Phys. Rev. Lett.* **58**, 2486-2489 (1987).

[111] Hsu, C. W., Zhen, B., Stone, A. D., Joannopoulos, J. D. & Soljačić, M. Bound states in the continuum. *Nat. Rev. Mater.* **1**, 16048 (2016).

[112] Arcari, M. *et al.* Near-Unity Coupling Efficiency of a Quantum Emitter to a Photonic Crystal Waveguide. *Phys. Rev. Lett.* **113**, 093603 (2014).

[113] Fushman, I. *et al.* Controlled Phase Shifts with a Single Quantum Dot. *Science* **320**, 769 (2008).

[114] Kim, J.-H., Aghaeimeibodi, S., Richardson, C. J. K., Leavitt, R. P. & Waks, E. Super-Radiant Emission from Quantum Dots in a Nanophotonic Waveguide. *Nano Lett.* **18**, 4734-4740 (2018).

[115] Englund, D. *et al.* Controlling cavity reflectivity with a single quantum dot. *Nature* **450**, 857-861 (2007).

[116] Majumdar, A., Rundquist, A., Bajcsy, M. & Vučković, J. Cavity quantum electrodynamics with a single quantum dot coupled to a photonic molecule. *Physical Review B* **86**, 045315 (2012).

[117] Sun, S., Kim, H., Luo, Z., Solomon, G. S. & Waks, E. A single-photon switch and transistor enabled by a solid-state quantum memory. *Science* **361**, 57 (2018).

[118] Sun, S., Kim, H., Solomon, G. S. & Waks, E. A quantum phase switch between a single solid-state spin and a photon. *Nat. Nanotechnol.* **11**, 539-544 (2016).

[119] Zhang, J. L. *et al.* Strongly Cavity-Enhanced Spontaneous Emission from Silicon-Vacancy Centers in Diamond. *Nano Lett.* **18**, 1360-1365 (2018).

[120] Sun, S. *et al.* Cavity-Enhanced Raman Emission from a Single Color Center in a Solid. *Phys. Rev. Lett.* **121**, 083601 (2018).

[121] Kindem, J. M. *et al.* Control and single-shot readout of an ion embedded in a nanophotonic cavity. *Nature* **580**, 201-204 (2020).

[122] Zhong, T. *et al.* Optically Addressing Single Rare-Earth Ions in a Nanophotonic Cavity. *Phys. Rev. Lett.* **121**, 183603 (2018).

[123] Zhong, T. *et al.* Nanophotonic rare-earth quantum memory with optically controlled retrieval. *Science* **357**, 1392 (2017).

[124] Zhong, T., Kindem, J. M., Miyazono, E. & Faraon, A. Nanophotonic coherent light–matter interfaces based on rare-earth-doped crystals. *Nat. Commun.* **6**, 8206 (2015).

[125] Lesik, M. *et al.* Maskless and targeted creation of arrays of colour centres in diamond using focused ion beam technology. **210**, 2055-2059 (2013).

[126] Benson, O. Assembly of hybrid photonic architectures from nanophotonic constituents. *Nature* **480**, 193-199 (2011).

[127] Böhm, F. *et al.* On-chip integration of single solid-state quantum emitters with a SiO2 photonic platform. *New Journal of Physics* **21**, 045007 (2019).

[128] Wolters, J. *et al.* Enhancement of the zero phonon line emission from a single nitrogen vacancy center in a nanodiamond via coupling to a photonic crystal cavity. *Appl. Phys. Lett.* **97**, 141108 (2010).

[129] Barclay, P. E., Fu, K. M., Santori, C. & Beausoleil, R. G. Hybrid photonic crystal cavity and waveguide for coupling to diamond NV-centers. *Opt. Express* **17**, 9588-9601 (2009).

[130] Hoang, T. B., Akselrod, G. M. & Mikkelsen, M. H. Ultrafast Room-Temperature Single Photon Emission from Quantum Dots Coupled to Plasmonic Nanocavities. *Nano Lett.* **16**, 270-275 (2016).

[131] Nguyen, M. *et al.* Nanoassembly of quantum emitters in hexagonal boron nitride and gold nanospheres. *Nanoscale* **10**, 2267-2274 (2018).

[132] Chen, Y. *et al.* Deterministic Positioning of Colloidal Quantum Dots on Silicon Nitride Nanobeam Cavities. *Nano Lett.* **18**, 6404-6410 (2018).

[133] Duong, N. M. H. *et al.* Enhanced Emission from WSe2 Monolayers Coupled to Circular Bragg Gratings. *ACS Photonics* **5**, 3950-3955 (2018).

[134] Fryett, T. K. *et al.* Encapsulated Silicon Nitride Nanobeam Cavity for Hybrid Nanophotonics. *ACS Photonics* **5**, 2176-2181 (2018).

[135] Peyskens, F., Chakraborty, C., Muneeb, M., Van Thourhout, D. & Englund, D. Integration of single photon emitters in 2D layered materials with a silicon nitride photonic chip. *Nat. Commun.* **10**, 4435 (2019).

[136] Kim, J.-H. *et al.* Hybrid Integration of Solid-State Quantum Emitters on a Silicon Photonic Chip. *Nano Lett.* **17**, 7394-7400 (2017).

[137] Elshaari, A. W. *et al.* On-chip single photon filtering and multiplexing in hybrid quantum photonic circuits. *Nat. Commun.* **8**, 379 (2017).

[138] Mouradian, S. L. *et al.* Scalable Integration of Long-Lived Quantum Memories into a Photonic Circuit. *Phys. Rev. X* **5**, 031009 (2015).

[139] Wan, N. H. *et al.* Large-scale integration of artificial atoms in hybrid photonic circuits. *Nature* **583**, 226-231 (2020).

[140] Elshaari, A. W., Pernice, W., Srinivasan, K., Benson, O. & Zwiller, V. Hybrid integrated quantum photonic circuits. *Nat. Photonics* **14**, 285-298 (2020).

[141] Kim, J.-H., Aghaeimeibodi, S., Carolan, J., Englund, D. & Waks, E. Hybrid integration methods for on-chip quantum photonics. *Optica* **7**, 291-308 (2020).

[142] Karouta, F. A practical approach to reactive ion etching. *Journal of Physics D: Applied Physics* **47**, 233501 (2014).

[143] Utke, I., Moshkalev, S. & Russell, P. *Nanofabrication Using Focused Ion and Electron Beams*. (Oxford University Press, New York, 2012).

[144] Sekoguchi, H., Takahashi, Y., Asano, T. & Noda, S. Photonic crystal nanocavity with a Q-factor of ~9 million. *Opt. Express* **22**, 916-924 (2014).

[145] Shen, Y. *et al.* Deep learning with coherent nanophotonic circuits. *Nat. Photonics* **11**, 441-446 (2017).

[146] Mauranyapin, N. P., Madsen, L. S., Taylor, M. A., Waleed, M. & Bowen, W. P. Evanescent single-molecule biosensing with quantum-limited precision. *Nat. Photonics* **11**, 477 (2017).

[147] Wu, S. *et al.* Monolayer semiconductor nanocavity lasers with ultralow thresholds. *Nature* **520**, 69-72 (2015).

[148] Lodahl, P., Mahmoodian, S. & Stobbe, S. Interfacing single photons and single quantum dots with photonic nanostructures. *Rev. Mod. Phys.* **87**, 347-400 (2015).

[149] Kim, H., Bose, R., Shen, T. C., Solomon, G. S. & Waks, E. A quantum logic gate between a solid-state quantum bit and a photon. *Nat. Photonics*, 373-377 (2013).

[150] He, X. *et al.* Tunable room-temperature single-photon emission at telecom wavelengths from sp3 defects in carbon nanotubes. *Nat. Photonics* **11**, 577 (2017).

[151] Chu, X.-L., Götzinger, S. & Sandoghdar, V. A single molecule as a high-fidelity photon gun for producing intensity-squeezed light. *Nat. Photonics* **11**, 58 (2016).

[152] Senellart, P., Solomon, G. & White, A. High-performance semiconductor quantum-dot single-photon sources. *Nat. Nanotechnol.* **12**, 1026 (2017).

[153] Englund, D. *et al.* Controlling the spontaneous emission rate of single quantum dots in a two-dimensional photonic crystal. *Phys. Rev. Lett.* **95**, 013904 (2005).

[154] Englund, D. *et al.* Resonant excitation of a quantum dot strongly coupled to a photonic crystal nanocavity. *Phys Rev Lett* **104**, 073904 (2010).

[155] Khasminskaya, S. *et al.* Fully integrated quantum photonic circuit with an electrically driven light source. *Nat. Photonics* **10**, 727 (2016).

[156] Davanco, M. *et al.* Heterogeneous integration for on-chip quantum photonic circuits with single quantum dot devices. *Nat. Commun.* **8**, 889 (2017).

[157] Tonndorf, P. *et al.* On-Chip Waveguide Coupling of a Layered Semiconductor Single-Photon Source. *Nano Lett.* **17**, 5446-5451 (2017).

[158] Cai, T. *et al.* Coupling Emission from Single Localized Defects in Two-Dimensional Semiconductor to Surface Plasmon Polaritons. *Nano Lett.* **17**, 6564-6568 (2017).

[159] Schell, A. W., Takashima, H., Tran, T. T., Aharonovich, I. & Takeuchi, S. Coupling Quantum Emitters in 2D Materials with Tapered Fibers. *ACS Photonics* **4**, 761-767 (2017).

[160] Cassabois, G., Valvin, P. & Gil, B. Hexagonal boron nitride is an indirect bandgap semiconductor. *Nat. Photonics* **10**, 262-266 (2016).

[161] Shotan, Z. *et al.* Photoinduced Modification of Single-Photon Emitters in Hexagonal Boron Nitride. *ACS Photonics* **3**, 2490-2496 (2016).

[162] Exarhos, A. L., Hopper, D. A., Grote, R. R., Alkauskas, A. & Bassett, L. C. Optical Signatures of Quantum Emitters in Suspended Hexagonal Boron Nitride. *ACS Nano* **11**, 3328-3336 (2017).

[163] Giles, A. J. *et al.* Ultralow-loss polaritons in isotopically pure boron nitride. *Nature Materials* (2017).

[164] Caldwell, J. D. *et al.* Sub-diffractional volume-confined polaritons in the natural hyperbolic material hexagonal boron nitride. *Nat. Commun.* **5**, 5221 (2014).

[165] Ahn, B.-H. *et al.* One-dimensional parabolic-beam photonic crystal laser. *Optics Express* **18**, 5654-5660 (2010).

[166] Taniguchi, T. & Watanabe, K. Synthesis of high-purity boron nitride single crystals under high pressure by using Ba–BN solvent. *Journal of Crystal Growth* **303**, 525-529 (2007).

[167] Elbadawi, C. *et al.* Electron beam directed etching of hexagonal boron nitride. *Nanoscale* **8**, 16182-16186 (2016).

[168] Kim, S., Toth, M. & Aharonovich, I. Design of photonic microcavities in hexagonal boron nitride. *Beilstein Journal of Nanotechnology* **9**, 102-108 (2018).

[169] Tran, T. T. *et al.* Robust Multicolor Single Photon Emission from Point Defects in Hexagonal Boron Nitride. *ACS Nano* **10**, 7331-7338 (2016).

[170] Kim, S., Kim, H.-M. & Lee, Y.-H. Single nanobeam optical sensor with a high Q-factor and high sensitivity. *Opt. Lett.* **40**, 5351-5354 (2015).

[171] Riedrich-Moller, J. *et al.* One- and two-dimensional photonic crystal microcavities in single crystal diamond. *Nat. Nanotechnol.* **7**, 69-74 (2012).

[172] Rousseau, I. *et al.* Quantification of scattering loss of III-nitride photonic crystal cavities in the blue spectral range. *Physical Review B* **95**, 125313 (2017).

[173] Bracher, D. O. & Hu, E. L. Fabrication of High-Q Nanobeam Photonic Crystals in Epitaxially Grown 4H-SiC. *Nano Lett.* **15**, 6202-6207 (2015).

[174] Burek, M. J. *et al.* High quality-factor optical nanocavities in bulk single-crystal diamond. *Nat. Commun.* **5**, 5718 (2014).

[175] Novoselov, K. S., Mishchenko, A., Carvalho, A. & Castro Neto, A. H. 2D materials and van der Waals heterostructures. *Science* **353**, 461 (2016).

[176] Fiori, G. *et al.* Electronics based on two-dimensional materials. *Nat. Nanotechnol.* **9**, 768-779 (2014).

[177] Mak, K. F. & Shan, J. Photonics and optoelectronics of 2D semiconductor transition metal dichalcogenides. *Nat. Photonics* **10**, 216-226 (2016).

[178] Xia, F., Wang, H., Xiao, D., Dubey, M. & Ramasubramaniam, A. Two-dimensional material nanophotonics. *Nat. Photonics* **8**, 899-907 (2014).

[179] Dai, S. *et al.* Tunable Phonon Polaritons in Atomically Thin van der Waals Crystals of Boron Nitride. *Science* **343**, 1125-1129 (2014).

[180] Flatten, L. C. *et al.* Microcavity enhanced single photon emission from two-dimensional WSe2. *Appl. Phys. Lett.* **112**, 191105 (2018).

[181] Ren, T., Song, P., Chen, J. & Loh, K. P. Whisper Gallery Modes in Monolayer Tungsten Disulfide-Hexagonal Boron Nitride Optical Cavity. *ACS Photonics* **5**, 353-358 (2018).

[182] Barik, S. *et al.* A topological quantum optics interface. **359**, 666-668 (2018).

[183] Noh, G. *et al.* Stark Tuning of Single-Photon Emitters in Hexagonal Boron Nitride. *Nano Lett.* **18**, 4710-4715 (2018).

[184] Hovington, P., Drouin, D. & Gauvin, R. CASINO: A new monte carlo code in C language for electron beam interaction —part I: Description of the program. *Scanning* **19**, 1-14 (1997).

[185] Grosso, G. *et al.* Tunable and high-purity room temperature single-photon emission from atomic defects in hexagonal boron nitride. *Nat. Commun.* **8**, 705 (2017).

[186] Kotakoski, J., Jin, C. H., Lehtinen, O., Suenaga, K. & Krasheninnikov, A. V. Electron knock-on damage in hexagonal boron nitride monolayers. *Physical Review B* **82**, 113404 (2010).

[187] Toth, M. *et al.* Nanostructure Fabrication by Ultra-High-Resolution Environmental Scanning Electron Microscopy. *Nano Lett.* **7**, 525-530 (2007).

[188] Grenadier, S., Li, J., Lin, J. & Jiang, H. Dry etching techniques for active devices based on hexagonal boron nitride epilayers. *Journal of Vacuum Science & Technology A* **31**, 061517 (2013).

[189] Martin, A. A., Toth, M. & Aharonovich, I. Subtractive 3D Printing of Optically Active Diamond Structures. *Sci. Rep.* **4**, 5022 (2014).

[190] Wang, J., Sciarrino, F., Laing, A. & Thompson, M. G. Integrated photonic quantum technologies. *Nat. Photonics* **14**, 273-284 (2019).

[191] Lo, H.-K., Curty, M. & Tamaki, K. Secure quantum key distribution. *Nat. Photonics* **8**, 595-604 (2014).

[192] Takemoto, K. *et al.* Quantum key distribution over 120 km using ultrahigh purity single-photon source and superconducting single-photon detectors. *Sci. Rep.* **5**, 14383 (2015).

[193] Liu, J. *et al.* A solid-state source of strongly entangled photon pairs with high brightness and indistinguishability. *Nat. Nanotechnol.* **14**, 586-593 (2019).

[194] Ding, X. *et al.* On-Demand Single Photons with High Extraction Efficiency and Near-Unity Indistinguishability from a Resonantly Driven Quantum Dot in a Micropillar. *Phys. Rev. Lett.* **116**, 020401 (2016).

[195] Dory, C. *et al.* Inverse-designed diamond photonics. *Nat. Commun.* **10**, 3309 (2019).

[196] Schröder, T. *et al.* Quantum nanophotonics in diamond [Invited]. *J. Opt. Soc. Am. B* **33**, B65-B83 (2016).

[197] Lombardi, P. *et al.* Photostable Molecules on Chip: Integrated Sources of Nonclassical Light. *ACS Photonics* **5**, 126-132 (2018).

[198] Türschmann, P. *et al.* Chip-Based All-Optical Control of Single Molecules Coherently Coupled to a Nanoguide. *Nano Lett.* **17**, 4941-4945 (2017).

[199] Radulaski, M. *et al.* Scalable Quantum Photonics with Single Color Centers in Silicon Carbide. *Nano Lett.* **17**, 1782-1786 (2017).

[200] Li, X., Scully, R. A., Shayan, K., Luo, Y. & Strauf, S. Near-Unity Light Collection Efficiency from Quantum Emitters in Boron Nitride by Coupling to Metallo-Dielectric Antennas. *ACS Nano* **13**, 6992-6997 (2019).

[201] Caldwell, J. D. *et al.* Photonics with hexagonal boron nitride. *Nat. Rev. Mater.* **4**, 552-567 (2019).

[202] Jungwirth, N. R. & Fuchs, G. D. Optical Absorption and Emission Mechanisms of Single Defects in Hexagonal Boron Nitride. *Phys Rev Lett* **119**, 057401 (2017).

[203] Vogl, T., Lecamwasam, R., Buchler, B. C., Lu, Y. & Lam, P. K. Compact Cavity-Enhanced Single-Photon Generation with Hexagonal Boron Nitride. *ACS Photonics* **6**, 1955-1962 (2019).

[204] Exarhos, A. L., Hopper, D. A., Patel, R. N., Doherty, M. W. & Bassett, L. C. Magnetic-field-dependent quantum emission in hexagonal boron nitride at room temperature. *Nat. Commun.* **10**, 222 (2019).

[205] Nikolay, N. *et al.* Direct measurement of quantum efficiency of single-photon emitters in hexagonal boron nitride. *Optica* **6**, 1084-1088 (2019).

[206] Vogl, T. *et al.* Radiation tolerance of two-dimensional material-based devices for space applications. *Nat. Commun.* **10**, 1202 (2019).

[207] Nicholas, V. P. *et al.* Microcavity-coupled emitters in hexagonal boron nitride. *Nanophotonics* **9**, 2937-2944 (2020).

[208] Stern, H. L. *et al.* Spectrally Resolved Photodynamics of Individual Emitters in Large-Area Monolayers of Hexagonal Boron Nitride. *ACS Nano* **13**, 4538-4547 (2019).

[209] Radulaski, M. *et al.* Nanodiamond Integration with Photonic Devices. *Laser Photonics Rev.* **13**, 1800316 (2019).

[210] Dutta, S. *et al.* Coupling quantum emitters in WSe2 monolayers to a metal-insulator-metal waveguide. *Appl. Phys. Lett.* **113**, 191105 (2018).

[211] Liu, C.-h., Zheng, J., Chen, Y., Fryett, T. & Majumdar, A. Van der Waals materials integrated nanophotonic devices [Invited]. *Opt. Mater. Express* **9**, 384-399 (2019).

[212] Behura, S. *et al.* Chemical Interaction-Guided, Metal-Free Growth of Large-Area Hexagonal Boron Nitride on Silicon-Based Substrates. *ACS Nano* **11**, 4985-4994 (2017).

[213] Khan, M., Babinec, T., McCutcheon, M. W., Deotare, P. & Lončar, M. Fabrication and characterization of high-quality-factor silicon nitride nanobeam cavities. *Opt. Lett.* **36**, 421-423 (2011).

[214] Liu, J. *et al.* Single Self-Assembled $\mathrm{InAs}/\mathrm{GaAs}$ Quantum Dots in Photonic Nanostructures: The Role of Nanofabrication. *Physical Review Applied* **9**, 064019 (2018).

[215] Li, X. *et al.* Nonmagnetic Quantum Emitters in Boron Nitride with Ultranarrow and Sideband-Free Emission Spectra. *ACS Nano* **11**, 6652-6660 (2017).

[216] Duong, N. M. H. *et al.* Facile Production of Hexagonal Boron Nitride Nanoparticles by Cryogenic Exfoliation. *Nano Lett.* **19**, 5417-5422 (2019).

[217] Kovalenko, M. V. *et al.* Prospects of Nanoscience with Nanocrystals. *ACS Nano* **9**, 1012-1057 (2015).

[218] Wilhelm, S. Perspectives for Upconverting Nanoparticles. *ACS Nano* **11**, 10644-10653 (2017).

[219] Koenderink, A. F. Single-Photon Nanoantennas. *ACS Photonics* **4**, 710-722 (2017).

[220] Englund, D. *et al.* Deterministic coupling of a single nitrogen vacancy center to a photonic crystal cavity. *Nano Lett.* **10**, 3922-3926 (2010).

[221] Barth, M. *et al.* Nanoassembled Plasmonic-Photonic Hybrid Cavity for Tailored Light-Matter Coupling. *Nano Lett.* **10**, 891-895 (2010).

[222] Santhosh, K., Bitton, O., Chuntonov, L. & Haran, G. Vacuum Rabi splitting in a plasmonic cavity at the single quantum emitter limit. *Nat. Commun.* **7**, ncomms11823 (2016).

[223] Bogdanov, S. I. *et al.* Ultrabright Room-Temperature Sub-Nanosecond Emission from Single Nitrogen-Vacancy Centers Coupled to Nanopatch Antennas. *Nano Lett.* **18**, 4837-4844 (2018).

[224] Fehler, K. G., Ovvyan, A. P., Gruhler, N., Pernice, W. H. P. & Kubanek, A. Efficient Coupling of an Ensemble of Nitrogen Vacancy Center to the Mode of a High-Q, Si3N4 Photonic Crystal Cavity. *ACS Nano* **13**, 6891-6898 (2019).

[225] Pattantyus-Abraham, A. G. *et al.* Site-Selective Optical Coupling of PbSe Nanocrystals to Si-Based Photonic Crystal Microcavities. *Nano Lett.* **9**, 2849-2854 (2009).

[226] Gupta, S. & Waks, E. Spontaneous emission enhancement and saturable absorption of colloidal quantum dots coupled to photonic crystal cavity. *Opt. Express* **21**, 29612-29619 (2013).

[227] Fernandez-Bravo, A. *et al.* Ultralow-threshold, continuous-wave upconverting lasing from subwavelength plasmons. *Nature Materials* **18**, 1172-1176 (2019).

[228] Fernandez-Bravo, A. *et al.* Continuous-wave upconverting nanoparticle microlasers. *Nat. Nanotechnol.* **13**, 572-577 (2018).

[229] Chatzidrosos, G. *et al.* Miniature Cavity-Enhanced Diamond Magnetometer. *Physical Review Applied* **8**, 044019 (2017).

[230] Shalaginov, M. Y. *et al.* On-Chip Single-Layer Integration of Diamond Spins with Microwave and Plasmonic Channels. *ACS Photonics* **7**, 2018-2026 (2020).

[231] Tran, T. T. *et al.* Anti-Stokes excitation of solid-state quantum emitters for nanoscale thermometry. *science Advances* **5**, eaav9180 (2019).

[232] Li, K., Zhou, Y., Rasmita, A., Aharonovich, I. & Gao, W. B. Nonblinking Emitters with Nearly Lifetime-Limited Linewidths in CVD Nanodiamonds. *Physical Review Applied* **6**, 024010 (2016).

[233] Castelletto, S. *et al.* Room Temperature Quantum Emission from Cubic Silicon Carbide Nanoparticles. *ACS Nano* **8**, 7938-7947 (2014).

[234] Siampour, H. *et al.* On-chip excitation of single germanium vacancies in nanodiamonds embedded in plasmonic waveguides. *Light: Science & Applications* **7**, 61 (2018).

[235] Schell, A. W. *et al.* A scanning probe-based pick-and-place procedure for assembly of integrated quantum optical hybrid devices. *Review of Scientific Instruments* **82**, 073709 (2011).

[236] Alagappan, G., Krivitsky, L. A. & Png, C. E. Diamond in a Nanopocket: A New Route to a Strong Purcell Effect. *ACS Omega* **3**, 4733-4742 (2018).

[237] Robinson, J. T., Manolatou, C., Chen, L. & Lipson, M. Ultrasmall mode volumes in dielectric optical microcavities. *Phys. Rev. Lett.* **95**, 143901 (2005).

[238] Ryckman, J. D. & Weiss, S. M. Low mode volume slotted photonic crystal single nanobeam cavity. *Appl. Phys. Lett.* **101**, 071104 (2012).

[239] Hu, S. *et al.* Experimental realization of deep-subwavelength confinement in dielectric optical resonators. *Science Advances* **4**, eaat2355 (2018).

[240] Choi, H., Heuck, M. & Englund, D. Self-Similar Nanocavity Design with Ultrasmall Mode Volume for Single-Photon Nonlinearities. *Phys. Rev. Lett.* **118**, 223605 (2017).

[241] Schröder, S. *et al.* Modeling of light scattering in different regimes of surface roughness. *Opt. Express* **19**, 9820-9835 (2011).

[242] Hostein, R. *et al.* Room temperature spontaneous emission enhancement from quantum dots in photonic crystal slab cavities in the telecommunications C band. *Appl. Phys. Lett.* **94**, 123101 (2009).

[243] Hensen, B. *et al.* A silicon quantum-dot-coupled nuclear spin qubit. *Nat. Nanotechnol.* **15**, 13-17 (2020).

[244] van Donkelaar, J. *et al.* Single atom devices by ion implantation. *Journal of Physics: Condensed Matter* **27**, 154204 (2015).

[245] Tuček, J. *et al.* Emerging chemical strategies for imprinting magnetism in graphene and related 2D materials for spintronic and biomedical applications. *Chemical Society Reviews* **47**, 3899-3990 (2018).

[246] Lukin, D. M. *et al.* 4H-silicon-carbide-on-insulator for integrated quantum and nonlinear photonics. *Nat. Photonics* (2019).

[247] Johannes, G. *et al.* Spectroscopic Investigations of Negatively Charged Tin-Vacancy Centres in Diamond. *New Journal of Physics* (2019).

[248] Sohn, Y.-I. *et al.* Controlling the coherence of a diamond spin qubit through its strain environment. *Nat. Commun.* **9**, 2012 (2018).

[249] Scarabelli, D., Trusheim, M., Gaathon, O., Englund, D. & Wind, S. J. Nanoscale Engineering of Closely-Spaced Electronic Spins in Diamond. *Nano Lett.* **16**, 4982-4990 (2016).

[250] Schröder, T. *et al.* Scalable focused ion beam creation of nearly lifetime-limited single quantum emitters in diamond nanostructures. *Nat. Commun.* **8**, 15376 (2017).

[251] Zhou, Y. *et al.* Direct writing of single germanium vacancy center arrays in diamond. *New Journal of Physics* **20**, 125004 (2018).

[252] Lühmann, T., John, R., Wunderlich, R., Meijer, J. & Pezzagna, S. Coulomb-driven single defect engineering for scalable qubits and spin sensors in diamond. *Nat. Commun.* **10**, 4956 (2019).

[253] Haruyama, M. *et al.* Triple nitrogen-vacancy centre fabrication by C5N4Hn ion implantation. *Nat. Commun.* **10**, 2664 (2019).

[254] Wang, J. *et al.* Efficient Generation of an Array of Single Silicon-Vacancy Defects in Silicon Carbide. *Physical Review Applied* **7**, 064021 (2017).

[255] Siyushev, P. *et al.* Coherent properties of single rare-earth spin qubits. *Nat. Commun.* **5**, 3895 (2014).

[256] Bangert, U. *et al.* Ion Implantation of Graphene—Toward IC Compatible Technologies. *Nano Lett.* **13**, 4902-4907 (2013).

[257] Bischoff, L., Mazarov, P., Bruchhaus, L. & Gierak, J. Liquid metal alloy ion sources—An alternative for focussed ion beam technology. *Applied Physics Reviews* **3**, 021101 (2016).

[258] Nelson, R. S. The theory of recoil implantation. *Radiation Effects* **2**, 47-50 (1969).

[259] Paine, B. M. & Averback, R. S. Ion beam mixing: Basic experiments. *Nuclear Instruments and Methods in Physics Research Section B: Beam Interactions with Materials and Atoms* **7-8**, 666-675 (1985).

[260] Möller, W. & Eckstein, W. Ion mixing and recoil implantation simulations by means of tridyn. *Nuclear Instruments and Methods in Physics Research Section B: Beam Interactions with Materials and Atoms* **7-8**, 645-649 (1985).

[261] Sigmund, P. Recoil implantation and ion-beam-induced composition changes in alloys and compounds. *Journal of Applied Physics* **50**, 7261-7263 (1979).

[262] Bahm, A. Predictive modelling of gas assisted electron and ion beam induced etching and deposition. http://hdl.handle.net/10453/62155 (2016).

[263] Ziegler, J. F., Ziegler, M. D. & Biersack, J. P. SRIM – The stopping and range of ions in matter (2010). *Nuclear Instruments and Methods in Physics Research Section B: Beam Interactions with Materials and Atoms* **268**, 1818-1823 (2010).

[264] Sandstrom, R. *et al.* Optical properties of implanted Xe color centers in diamond. *Optics Communications* **411**, 182-186 (2018).

[265] Tamura, S. *et al.* Array of bright silicon-vacancy centers in diamond fabricated by low-energy focused ion beam implantation. *Applied Physics Express* **7**, 115201 (2014).

[266] Demtröder, W. *Laser spectroscopy: vol. 2: experimental techniques*. Vol. 2 (Springer Science & Business Media, 2008).

[267] Lindner, S. *et al.* Strongly inhomogeneous distribution of spectral properties of silicon-vacancy color centers in nanodiamonds. *New Journal of Physics* **20**, 115002 (2018).

[268] Ziegler, J. F., Ziegler, M. D. & Biersack, J. P. 8 - TRIM – SETUP AND INPUT http://www.srim.org/SRIM/SRIM%2008.pdf (2008).

[269] Burnett, T. L. *et al.* Large volume serial section tomography by Xe Plasma FIB dual beam microscopy. *Ultramicroscopy* **161**, 119-129 (2016).

[270] Bassim, N., Scott, K. & Giannuzzi, L. A. Recent advances in focused ion beam technology and applications. *MRS Bulletin* **39**, 317-325 (2014).

[271] Middleton, R. J. U. o. P., unpublished. A negative ion cookbook. (1989).

[272] Koch, M. *et al.* Spin read-out in atomic qubits in an all-epitaxial three-dimensional transistor. *Nat. Nanotechnol.* **14**, 137-140 (2019).

[273] Bali, R. *et al.* Printing Nearly-Discrete Magnetic Patterns Using Chemical Disorder Induced Ferromagnetism. *Nano Lett.* **14**, 435-441 (2014).

[274] Hughes, M. A. *et al.* n-type chalcogenides by ion implantation. *Nat. Commun.* **5**, 5346 (2014).

[275] Fei, Z. *et al.* Two-dimensional itinerant ferromagnetism in atomically thin Fe3GeTe2. *Nature Materials* **17**, 778-782 (2018).

[276] Mendelson, N. *et al.* Grain Dependent Growth of Bright Quantum Emitters in Hexagonal Boron Nitride. *arXiv e-prints*, arXiv:2005.10699 (2020).

[277] Butcher, A. *et al.* High-Q Nanophotonic Resonators on Diamond Membranes using Templated Atomic Layer Deposition of TiO2. *Nano Lett.* **20**, 4603-4609 (2020).